UNIVERSITY OF CALIFORNIA

Los Angeles

Rational Design of Nanomaterials for Next Generation Lithium-Sulfur Batteries

A dissertation submitted in partial satisfaction of the
requirements for the degree Doctor of Philosophy
in Chemical Engineering

by

Fang Liu

2018

© Copyright by

Fang Liu

2018

ABSTRACT OF THE DISSERTATION

Rational Design of Nanomaterials for Next Generation Lithium-Sulfur Batteries

by

Fang Liu
Doctor of Philosophy in Chemical Engineering
University of California, Los Angeles, 2018
Professor Yunfeng Lu, Chair

This dissertation focuses on the fundamental problems in the lithium-sulfur battery, which is one of the most promising candidates for next-generation electric energy storage. Despite years of research, the electrochemical process in lithium-sulfur batteries remains ambiguous. The first part of this dissertation discusses the geometric and electronic band structures of related sulfur species, and how these intrinsic properties determine their electrochemical behaviors. The second part introduces the concept of regenerative polysulfide-scavenging layers which mitigate the shuttling phenomenon of polysulfides. It also details the interactions between various metal oxides and lithium polysulfides in terms of physisorption and chemisorption. The third part illustrates the working mechanism of redox mediators for sulfur species and their expedited electrochemical behaviors. The last section presents the design of a hybrid silicate coating for lithium metal anode to suppress the formation of dendritic structures. These investigations unveil the fundamental limitations of lithium-sulfur batteries, and present practical strategies to achieve higher energy density, extended cycling life, and better safety.

The dissertation of Fang Liu is approved.

Bruce S. Dunn

Philippe Sautet

Yang Yang

Yunfeng Lu, Committee Chair

University of California, Los Angeles

2018

To my Parents, Xiaoye Liu and Guiwen Zhuang and
my Husband, Duo Xu

Table of Contents

List of Figures ………………………………………………………………………..…..… ix

List of Tables …………………………………………………………………………....xix

Acknowledgements……………………………………………………………………xx

Vita ……………………………………………………………………………………..xxii

Publications……………………………………………………………………………..xxii

Patents………………………………...……………………………………………..xxiii

Chapter 1 Introduction …………………………………………………………..…...1

Chapter 2 Electrochemical energy storage with battery systems ………………………....4

2.1 Fundamental of electrochemical energy storage systems ………………………….………4

2.1.1 Thermodynamics of cells ……………………………………...……..………6

2.1.2 Kinetics of electrode reactions ……………………………….……..………..6

2.2 Current state-of-the-art ..……………………………………...…………..………..8

2.2.1 Lithium-ion batteries with insertion chemistry ……………………………..…..……8

2.2.2 Post lithium-ion batteries with conversion chemistry ………………………..………9

2.3 Conclusion …………………………………………………………...……………10

Chapter 3 Lithium-sulfur battery ………………………………………………….….…11

3.1 Introduction ……………………………………………………………….…………11

3.2 Electrochemical reactions of lithium-sulfur battery ……………………………….……11

3.3 Fundamental problems ……………………………………………………………17

3.4 Current strategies ……………………………………………………………….……17

3.4.1 Carbon host materials ………………………………………………………..…17

3.4.2 Interfacial engineering …………………………………………………….….20

3.4.3 Functional interlayers ………………………………………………..………22

3.5 Conclusion ……………………………………………………………………..…………23

Chapter 4 Lithium metal battery …………………………………………………..…24

4.1 Introduction …………………………………………………………….……………24

4.2 Electrochemical reactions of lithium metal battery ………………………….……24

4.2.1 Electrochemical limitations …………………………………………….……24

4.2.2 Theoretical models …………………………………………………..………25

4.3 Current state-of-the-art ……………………………………………………………27

4.3.1 Electrolyte additives …………………………………………………………27

4.3.2 Coating layers ………………………………………………………..………28

4.4 Conclusion ……………………………………………………………………...…29

Chapter 5 Working mechanism and intrinsic properties of sulfur species …………………30

5.1 Introduction …………………………………………………………….…………30

5.2 Geometric structures of sulfur species ………………………………….………30

5.2.1 S_8 ……………………………………………………………………...30

5.2.2 Closed-shell lithium polysulfides ……………………………….………30

5.2.3 Sulfur radicals …………………………………………...………34

5.2.4 Li_2S_2 …………………………………………………………..……39

5.3 Electronic structures of sulfur species ……………………………………….…39

5.4 Conclusion ……………………………………………………………………...…41

Chapter 6 Regenerative Polysulfide-Scavenging Layers …………………….……42

6.1 Introduction ……………………………………………………………………….…42

6.2 Methods ……………………………………………………………………………...44

6.2.1 Synthesis of CNTs/oxides composites ……………………………….…44

6.2.2 Fabrication of RSL …………………………………………………………45

    6.2.3 Preparation of sulfur cathodes and Li_2S_6 solution ... 46
    6.2.4 Material characterization methods ... 46
    6.2.5 Electrochemical characterization methods ... 47
6.3 Material characterizations ... 47
6.4 Electrochemical behaviors ... 50
6.5 Characterizations of the scavenging and regeneration process ... 58
6.6 Working mechanisms of metal oxides ... 61
6.7 Chemisorption *vs.* physisorption ... 63
6.8 Conclusion ... 67
Chapter 7 Redox-mediators based on transitional metal oxides ... 68
7.1 Introduction ... 68
7.2 Geometric and electronic structures of redox mediators ... 69
7.3 Methods ... 72
    7.3.1 Synthesis of RGO and RGO-metal oxides composites ... 72
    7.3.2 Material characterizations ... 74
    7.3.3 Electrochemical characterizations ... 74
    7.3.4 DFT calculations ... 75
7.4 Electron transfers ... 76
7.5 Material characterizations ... 80
7.6 Electrochemical characterizations ... 83
7.7 Conclusion ... 87
Chapter 8 Hybrid Silicate Coatings for Lithium Metal Anodes ... 88
8.1 Introduction ... 88
8.2 Methods ... 90

    8.2.1 Fabrication of coated lithium metal anode ……………………………………………90

    8.2.2 Preparation of cathodes …………………………………………………………..……90

    8.2.3 Material characterization methods ……………………………………….…...…90

    8.2.4 Electrochemical characterization methods …………………………….…..…90

8.3 Material characterizations ……………………………………………………………………91

8.4 Electrochemical behaviors and morphological changes ……………………….………..…95

8.5 Side-reactions with electrolyte components ………………………………………...……103

8.6 Conclusion ………………………………………………………………………………..…104

References ……………………………………………………………………………...…106

List of Figures

Figure 1.1 Annual global market of electric vehicles. Reproduced from Bloomberg New Energy Finance ……………………………………………………………………………………1

Figure 1.2 Development of electric energy storage materials toward higher energy density, environmental benignity and better safety. Reproduced from Ref. 1 ……………………………..2

Figure 2.1 Representation of (**a**) reduction and (**b**) oxidation process of a species A/A$^+$. Reproduced from Ref. 2 ………………………………………..………………………..………5

Figure 2.2 Simplified Ragone plot of the energy storage domains of various energy storage and conversion systems. Reproduced from Wikipedia ……………………………..………………5

Figure 2.3 Typical discharge curve of a battery, showing three different kinds of polarization. Reproduced from Ref. 3……………………………………………………………………...7

Figure 2.4 Capacity and voltage ranges of anode and cathode materials for lithium-based batteries. Reproduced from Ref. 4 ..……………………………………………………………………9

Figure 3.1 Voltage profile of Li-S battery. Reproduced from Ref. 11 ………………………..…12

Figure 3.2 Relative quantity of sulfur species obtained from **a.** LC/MS and **b.** ^{1}H NMR result. Reproduced from Ref. 12 …………………………………………………………..………13

Figure 3.3 (**a-h**) The solvated structures of lithium polysulfides (Li_2S_n, $1 \leq n \leq 8$) in DOL solvent. Reproduced from Ref. 13 …………………..…………………………………………...…..14

Figure 3.4 ESR spectra of Li_2S_6 solution, showing the presence of S_3 free radical ions. (b) The ESR spectra of Li_2S_6 solution at 125 K showing the characteristic S = 1/2 EPR spectra. Reproduced from Ref. 14 ……………………………………………………………………………...15

Figure 3.5 a. First principle XANES spectra of LiS_3 radical in TEGDME solvent with five transition states. **b.** Structures and the calculated K-edge XANES spectra of LiS_5, LiS_4 and LiS_3 radicals, Li_2S_8 and Li_2S_6 molecules, and crystalline Li_2S. Reproduced from Ref. 17 ……………16

Figure 3.6 a. Discharge profile of lithium-sulfur battery. **b.** Comparison of the best fit spectra from theory and XAS measurement for the three voltages in **a.** Reproduced from Ref. 17 ………..…16

Figure 3.7 Illustration of **a.** Sulfur encapsulation in CMK-3 and **b.** Graphene wrapped sulfur microparticles. Reproduced from Ref. 18 and Ref. 19 ……………………………………..…18

Figure 3.8 First principle calculation of the interactions between undoped/nitrogen doped carbon atoms and sulfur species. Reproduced from Ref. 32...……..……………………………………..19

Figure 3.9 Synthesis process of nitrogen-doped mesoporous carbon sphere and CNT composites, as well as the electrochemical performances of lithium-sulfur batteries based on such composites. Reproduced from Ref. 28 ..……………………………………………………………………20

Figure 3.10 a. Schematic illustration of working mechanisms of non-polar conductors, polar insulator/semiconductors and polar conductors. **b.** Illustration of surface-mediated reduction of Li_2S from lithium polysulfides on metallic polar host Ti_4O_7. XANES results illustrate the distribution of sulfur species during discharge. The results of Ti_4O_7/S are shown in solid lines while that of VC-S are presented in dash lines. Reproduced from Ref. 33 and Ref. 34…………..21

Figure 3.11 a. Working mechanisms of SWCNT-modulated separator in lithium-sulfur battery. **b.** Illustration of ternary separator based on PP/GO/Nafion layers and their effective blocking effect toward lithium polysulfides. Reproduced from Ref. 35 and Ref. 36…………………………..22

Figure 4.1 Illustration of different working mechanisms of **a.** lithium-ion batteries and **b.** lithium metal batteries. **c.** The typical morphology of lithium dendrites and the associated problems. Reproduced from Ref. 39……………………………………………………………...……25

Figure 4.2 **a.** Displacement distribution at different polymer shear modulus (i) reference position, (ii) compressible polymer $v_s = 0$ and (iii) incompressible polymer $v_s = 0.5$. **b.** Contributions of compressive forces, deformation forces and surface forces as a function of polymer shear modulus, $v_s = 0.33$. Reproduced from Ref. 46…………………………………………………….………..26

Figure 4.3 Illustration of the working mechanisms of self-healing electrostatic shield. Reproduced from Ref. 53…………………………………………………………………………………...27

Figure 4.4 **a.** ALD protected lithium metal anode is resistant to air and lithium polysulfides, **b.** Working mechanism of carbon-sphere thin film in preventing the growth of lithium dendrites. Reproduced from Ref. 59 and 64……………………………………………………..……..…29

Figure 5.1 Geometric and electronic structures of sulfur species. The geometric structures of **a.** linear Li_2S_6-4DOL, **b.** cyclic Li_2S_6-2DME …………………………………………......….31

Figure 5.2 EPR spectrum of 20 mM Li_2S_6 solution at 5 K ……………………………………34

Figure 5.3 Geometric and electronic structures of Li_2S_2 …………………………………..……39

Figure 5.4 Electronic density of states (DOS) of **a.** S_8, **b.** LiS_4 radical, **c.** LiS_3 radical and **d.** Li_2S_2. Shadowed area represents filled valence band, while unfilled area indicates empty conduction band. The vertical dashed lines and solid lines show the positions of VBM and CBM, respectively...….40

Figure 5.5 Electronic band edges of sulfur species aligned with respect to vacuum energy. The sulfur species are (1) S_8, (2) Li_2S_7-DOL, (3) Li_2S_6-DOL, (4) Li_2S_5-DOL, (5) Li_2S_4-DOL, (6) LiS_5 radical, (7) LiS_4 radical, (8) LiS_3 radical, (9) LiS_5-DOL radical, (10) LiS_4-DOL radical, (11) LiS_3-DOL radical, (11) Li_2S_2 ……………………………………………………………………….41

Figure 6.1 Schematic presentation of a Li-S cell with a regenerative polysulfide-scavenging layers (RSL). The RSL is made from a CNTs membrane of which the center is embedded with interpenetrating nanowires or nanocrystals of metal oxides. (i) During discharge, as-generated polysulfides are adsorbed by or reacted with the RSL, immobilized onto the RSL denoted as [Polysulfides-RSL] complexes. (ii) Subsequent charge process strips away the immobilized species and regenerates the RSL, enabling dynamic blocking of the polysulfides ……………....43

Figure 6.2 a. SEM image of a CNTs/V_2O_5 composite with a fibrous structure made from interpenetrative V_2O_5 nanowires and CNTs. **b.** TEM images of the CNTs/V_2O_5 composites, showing a continuous and porous structure with average nanowire diameter of ~30 nm. **c.** High-resolution TEM image and its corresponding selected area FFT image (inset) of the CNTs/V_2O_5 composites. Scale bars are a. 500 nm; b. 50 nm, 10 nm (inset); **c.** 5 nm, 1 nm (inset) ………..…48

Figure 6.3 a. X-ray diffraction profile and **b.** TGA plot of the CNTs/V_2O_5 composites ……….48

Figure 6.4 Cross-section SEM image of a CNTs/V_2O_5 RSL made from two CNTs layers and a sandwiched CNTs/V_2O_5 layer. Scale bar is 5 µm ……………………………………..……49

Figure 6.5 Digital photographs of CNT/V_2O_5 RSL **a.** as prepared, **b.** folded and **c.** recovered state……………………………………………………………………………....49

Figure 6.6 a. Cyclic voltammetries obtained at a scanning rate of 0.2 mV s^{-1}. **b.** Nyquist plots showing a reduced charge-transfer resistance with the RSL..…………………………….……50

Figure. 6.7 Rate performance at 0.3 C, 0.5 C, 1 C, 2 C, 4 C and 0.3 C rate……..……………..…51

Figure 6.8 Galvanostatic cycling performance at 1 C rate. The empty bullets (○) represent the discharge capacity and circle bullets (•) represent the Coulombic efficiency.………..………52

Figure 6.9 Galvanostatic cycling performance of sulfur cathode with a mass loading of 6 mg cm^{-2} at **a.** 0.1 C rate and **b.** 0.2 C rate..………………………………………………….……53

Figure 6.10 Energy densities of Li-S cells with different sulfur loadings, ratios between electrolyte and sulfur (E/S) and specific capacities of active materials……………………………………55

Figure 6.11 a. Scavenging capacitance of the CNTs and CNTs/V_2O_5 RSL at different Li_2S_6 concentrations. Cyclic voltammetries of the equilibrated **b.** CNTs RSL and **c.** CNTs/V_2O_5 RSL cathodes at a scanning rate of 0.05 mV s^{-1}……..……………………………………………57

Figure 6.12 Self-discharge tests of sulfur cathodes with **a.** PP separator and **b.** CNTs/V_2O_5 RSL. The cells were cycled at 0.2 C for 9 cycles, stopped at 2.1 V during 10th discharge and rested for 3 days before the discharge process was resumed…………………………………………….....58

Figure 6.13 SEM image and element-mapping of CNTs/V_2O_5 RSL at discharged and charged stages. Li-S cells were cycled at 0.3 C between 1.7 to 2.8 V and a. interrupted at 2.05 V during the discharge or b. interrupted at 2.60 V during the charge. The blue arrows show the direction of the line scan, while the blue circles represent the starting and ending points. Purple line represents sulfur and orange line represents vanadium. Scale bars are a. 20 µm and b. 25 µm…..…………59

Figure 6.14 Cross-sectional SEM images and elemental mappings of lithium anodes after cycling with sulfur cathodes with and without the RSL. Li-S cells were assembled with **a-b.** CNTs RSL and **c-d.** CNTs/V_2O_5 RSL. Yellow color represents the distribution of sulfur species…………60

Figure 6.15 SEM images of lithium surface after cycling at 1 C for 50 cycles **a.** and **b.** Li-S cell with CNTs RSL, **c.** and **d.** Li-S cell with CNTs/V_2O_5 RSL…………..…………………………60

Figure 6.16 Reactions between V_2O_5 and polysulfides probed by XPS. **a.** Vanadium $2p_{3/2}$ spectra of V_2O_5 and **b.** V_2O_5/sulfide compound formed by reacting V_2O_5 with Li_2S_6, indicating the formation of V^{4+} in the presence of Li_2S_6. **c.** Sulfur 2p core spectra of Li_2S_6 showing the terminal (S_T^{-1}) and bridging (S_B^0) sulfur atoms with an expected ratio of 1:2. **d.** Sulfur 2p core spectra of the V_2O_5/sulfide compound. The formation of polythionate groups indicates redox reactions between Li_2S_6 and V_2O_5…………………………………..……………………………………62

Figure 6.17 Electron transfer directions regarding the relative positions of conduction bands and valence bands of the oxides and redox potential of the molecule.……………………………..…63

Figure 6.18 The interaction in physisorption and chemisorption. ……………………………64

Figure 6.19 Photographs of Li_2S_6 solutions mixed with metal oxides after centrifugation……..64

Figure 6.20 Absolute potentials of the conduction bands and valence bands of various metal oxides, as well as the oxidation potential of polysulfides (2.2 to 2.5 V *vs.* Li^+/Li, labeled in purple)….......65

Figure 6.21 Work functions of a series metal oxides. …………………………………………..65

Figure 6.22 A comparison of the bond energies between the metal oxides and polysulfides (Light green) with the specific capacity of the corresponding Li-S cells after 100 cycles at 1 C (Green)...66

Figure 6.23 Self-discharge rate of Li-S cells with different CNTs/oxide RSL …………………67

Figure 7.1 Illustration of electron transfer process in **a.** photosynthesis and **b.** dye sensitized solar cells. Reproduced from Wikipedia………………………………………………………....69

Figure 7.2 Geometric and electronic structures of redox mediators. The geometric structure of **a.** Nb_2O_5, **b.** $LiNb_2O_5$, **c.** MnO_2, and **d.** $Li_{0.5}MnO_2$. The corresponding electronic density of states of **e.** Nb_2O_5, **f.** $LiNb_2O_5$, **g.** MnO_2, and **h.** $Li_{0.5}MnO_2$. Lithium, niobium, manganese and oxygen atoms are shown in gray, green, blue, and red, respectively. Shadowed area represents filled valence band, while unfilled area indicates empty conduction band. The vertical dashed lines and solid lines show the positions of VBM and CBM, respectively …………………………………70

Figure 7.3 Electron paramagnetic resonance spectrum of **a.** Nb_2O_5 and **b.** $LiNb_2O_5$ at 5 K, illustrating the formation of EPR active species Nb^{4+}..……………………………………..72

Figure 7.4 Electron transfer pathways in the sulfur cathode with the presence of mediators. (1) S_8, (2) Li_2S_7-4DOL, (3) Li_2S_6-4DOL, (4) Li_2S_5-4DOL, (5) Li_2S_4-4DOL, (6) LiS_4-DOL, (7) LiS_3-DOL and (8) Li_2S_2…………………………………………………………………………...76

Figure 7.5 EPR spectrum of **b.** S-RGO electrode and **c.** S-Nb_2O_5 electrode at various potentials (*vs.* Li^+/Li). All the EPR spectra were recorded at 5 K. Scale bars are 1000 in **a.** and **b**………..77

Figure 7.6 Digital photograph of Li_2S_6 solution before and after mixing with RGO, $LiNb_2O_5$, and MnO_2 ……………………………………………………………………………………78

Figure 7.7 Niobium 3d spectrum of $LiNb_2O_5$ **d.** before and **e.** after mixing with Li_2S_6 solution. Sulfur 2p spectrum of **f.** Li_2S_6 and **g.** $LiNb_2O_5$-Li_2S_6 composites.………………………………79

Figure 7.8 Manganese 2p spectrum of MnO_2 **a.** before and **b.** after mixing with Li_2S_6 solution. **c.** Sulfur 2p spectrum of MnO_2-Li_2S_6 composites …………………………………………………79

Figure 7.9 TEM images of **a.** RGO, **b.** RGO-Nb_2O_5, **c.** RGO-MnO_2 composites and the corresponding high resolution TEM images of **d.** RGO, **e.** RGO-Nb_2O_5, **f.** RGO-MnO_2; Scale bars are 50 nm in TEM, and 5 nm in HRTEM ……………………………………………………...80

Figure 7.10 Thermogravimetric analysis of RGO-based composites ……………………………81

Figure 7.11 Tafel plot of RGO, Nb_2O_5, MnO_2 composites in 50 mM Li_2S_6 catholyte during **a.** cathodic scan and **b.** anodic scan ……………………………………………………………………81

Figure 7.12 SEM and EDS images of electrode based on S-Nb_2O_5 composites ……………..…82

Figure 7.13 **a.** Cyclic voltammetry of sulfur cathodes at a scanning rate of 0.3 mV s^{-1}, showing accelerated electrochemical kinetics of sulfur electrodes after incorporating oxides as redox mediators. **b.** Redox peak separations of sulfur cathodes with/without oxides at 0.3 mV s^{-1}..……83

Figure 7.14 Electrochemical performance of sulfur cathodes with/without redox mediators. **a.** Cyclic voltammetry of a S-Nb_2O_5 electrode under different sweep rates, ranging from 0.1 mV s^{-1} to 0.5 mV s^{-1}. **b-d.** Plots of cathodic and anodic peak currents *vs.* square root of sweep rates. **e.** Relative conversion rate of sulfur species during different electrochemical steps ……………….84

Figure 7.15 **a.** Comparison of the rate capability at various current densities. **b.** Representative voltage-capacity profiles of cells at high current densities (335 mA g^{-1}_{sulfur}, corresponding to 0.2 C rate)……………………………………………………………………………………...…86

Figure 7.16 Self-discharge capacity loss of sulfur cathodes with/without dual mediators ………86

Figure 7.17 Galvanostatic cycling performance at 0.1 C rate under different discharge conditions **d.** Self-discharge capacity loss of sulfur cathode with/without dual mediators. **e.** discharge to 1.7 V and **f.** discharge to 800 mAh g^{-1}_{sulfur} or 1.7 V………………………………………………..…87

Figure 8.1 Illustration of the formation of an organic-inorganic coating on LMA. **a.** Reactions of methoxysilane and ethoxysilane catalyzed by LiOH; **b.** Formation of an organic-inorganic coating layer on LMA ………………………………………………………………………………89

Figure 8.2 Characterizations of the inorganic-organic coatings. SEM images of a lithium foil **a.** before and **b.** after the vapor deposition. Elemental mapping of the coatings shows the uniform distribution of **c.** silicon and **d.** sulfur. Scale bars are 2 µm in a, b and 10 µm in c, d …………..91

Figure 8.3 Characterizations of the inorganic-organic coatings. **a.** FTIR spectra of the coatings, indicating the formation of Si-O-Si bonds. XPS analysis of a coating layer for **b.** silicon 2p and **c.** sulfur 2p and **d.** lithium 1s, respectively …………………………………………………………92

Figure 8.4 XPS depth profiling of coatings on LMA. Silicon 2p spectrum after etching for **a.** 0 s, **b.** 60 s, **c.** 180 s and **d.** 360 s, respectively …………………………………………………………93

Figure 8.5 Comparison of the current response of the coated and uncoated LMAs……………..94

Figure 8.6 Digital images of an uncoated and a coated lithium foil exposed to air at 25 ˚C and 50 % humidity ………………………………………………………………………………………94

Figure 8.7 Nyquist plots showing similar charge transfer resistance for symmetric cells of uncoated and coated LMAs ………………………………………………………………...95

Figure 8.8 Voltage profiles of symmetric lithium cells at 0.5 mA cm^{-2} in carbonate-based electrolyte ………………………………………………………………………………..96

Figure 8.9 SEM images of **a.** uncoated and **b.** coated LMAs after cycling for 100 h. Scale bars are 10 μm ………………………………………………………………………………96

Figure 8.10 SEM images of coated LMA with different volumetric ratio between MPS and TEOS a. 1:0, b. 2:1, c. 1:1, d. 0.5:1, e. 0:1. All the LMAs were cycled in symmetric cells for 100 h (50 cycles) under a current density of 0.5 mA cm^{-2} with an area capacity of 1 mAh cm^{-2}. Scale bars are 10 μm …………………………………………………………………………......97

Figure 8.11 Voltage profiles of symmetric lithium cells at 0.5 mA cm^{-2} in LiTFSI (1 M) in DOL/DME (*v*:*v* = 1:1)…………………………………………………………………..…..98

Figure 8.12 SEM images of **a.** uncoated and **b.** coated LMAs after cycling for 200 h. Scale bars are 10 μm in (**a**, **b**) and 1 μm in **c**..…………………………………………………..……99

Figure 8.13 SEM images of coated LMAs with a deposition time of 4 h under different magnifications. Scale bars are 10 μm in (A) and 2 μm in (B)..…………………………..……100

Figure 8.14 Voltage profiles of symmetric lithium cells at 2 mA cm^{-2} with an areal capacity of 2.0 mAh cm^{-2} in LiTFSI (1 M) in DOL/DME (*v*:*v* = 1:1)…….……………………………..……100

Figure 8.15 a. Voltage-capacity profile of Li-LiFePO$_4$ cells during the 3rd cycle at 0.5 C rate; **b.** Galvanostatic cycling performance of Li-LiFePO$_4$ cells at 0.5 C rate. **c.** Voltage-capacity profile of Li-S cells during the 3rd cycle at 0.3 C rate; **d.** Galvanostatic cycling performance of Li-S cells at 0.3 C rate……………...…………………………………………………………102

Figure 8.16 Comparison of (**A**) average cycling life and (**B**) degradation rate of capacity of Li-S batteries with uncoated and coated LMAs at 0.3 C rate ……………………………………..…..103

Figure 8.17 XPS analysis of LMAs after cycling regarding (**a**, **e**) carbon 1s, (**b**, **f**) fluorine 1s and (**c**, **g**) nitrogen 1s and (**d**, **h**) silicon 2p spectra of uncoated and coated LMAs, respectively. Both cells were cycled at 0.3 C rate for 150 cycles and interrupted at fully charged state (2.8 V *vs.* Li^+/Li)……………………………………………………………………………………104

List of Tables

Table 5.1 Electronic band structures of linear Li_2S_6 with different solvent models………….... 32

Table 5.2 Electronic band structures of cyclic Li_2S_6 with different solvent models…………….32

Table 5.3 Structures and electronic band edge positions of lithium polysulfide molecules…....33

Table 5.4 Structures and electronic band edge positions of LiS_5, LiS_4, LiS_3 radicals…………..36

Table 5.5 Comparison of g-factors obtained from DFT simulation and EPR measurement…....37

Table 5.6 Complexation free energy of solvated sulfur radicals……………………………..….38

Table 6.1 Comparison of sulfur contents and initial specific capacity of lithium-sulfur cells with different interlayers……………………………………….……………………...…54

Table 6.2 Table of capacity contributions from CNTs RSL and CNTs/V_2O_5 RSL in Li-S cells with various sulfur loadings at 1 C rate……………………………………………………..56

Table 7.1 Lattice parameters of T-Nb_2O_5 and $LiNb_2O_5$………………………………………70

Table 7.2 Lattice Parameters of MnO_2 and $Li_{0.5}MnO_2$………………………………………..71

Table 8.1 Comparison of the thickness of the coating layer, the resistance and the IR drop at a current density of 2 mA cm^{-2}. Assuming the diameter of the electrodes is 1.56 cm……..…….101

Acknowledgements

I would like to express my sincere gratitude to my Ph.D. advisor Prof. Yunfeng Lu for his guidance, encouragement, and continuous support throughout my Ph.D. study. I appreciate all his time, ideas, patience and research funding to make my Ph.D. career possible and fruitful. He is more than a research advisor, but also a life mentor. It is his determination, diligence, enthusiasm and optimism that supported us through the toughest days. It has been my honor to work in his group.

Through Prof. Lu, I have had the chance to collaborate with a number of faculty members at UCLA, including my committee: Prof. Bruce S. Dunn, Prof. Philippe Sautet and Prof. Yang Yang. I have learned so much through the collaborations, which is invaluable for my career. Thank you for serving as my committee and being so supportive over the years. Thank you for your time and assistance in my research work and evaluating this dissertation. I would also thank my formal committee members Prof. Jane P. Chang and Prof. Selim Senkan for all their time and help.

I would like to express my special thanks to our collaborator Dr. Mei Cai at General Motors company. She shows us a new perspective from the industrial view point that has guided our research design toward practical applications. I would also thank Dr. Qiangfeng Xiao at General Motors company for his generous help, support and guidance over the years. This dissertation won’t be possible without these wonderful collaborators.

I would like to thank Dr. Zheng Chen and Dr. Xiaolei Wang, who taught me the fundamental of electrochemistry and offered me great help over the years. I would also thank Dr. Hao Bin Wu, Dr. Huihui Zhou, Dr. Zaiyuan Le, Dr. Li Shen, Dr. Gurong Shen, Dr. Fei Sun, Dr. Xiaoyan Liu, Dr. Yufeng Jiang, Dr. Jianqiang Shen, Dr. Guoqiang Tan, Dr. Runwei Mo, Dr. Haiping Wu, Dr. Yang Liu, Dr. Di Wu, Xianyang Li, Fan Li, Shengxiang Ma, Ran Tao, Chen

Zhang, Wenyue Shi, and all other formal and current members in the group, who have made my life at UCLA enjoyable and memorable.

A special thanks to my parents and parents-in-law for their all-time support. Thank you for your faith in me at every stage of my life. Words cannot express how grateful I am. At last, I would like to thank my husband Duo Xu. Thank you for everything that you have done and thank you for being my soul mate. I believe the best is yet to come. Love you.

“Without commitment, you will never start. But more importantly, without consistency, you will never finish. --Denzel Washington”

Fang Liu
2018

Vita

2008-2012	B.E. in Department of Chemistry Jilin University Jilin, P. R. China
2012-2018	Graduate student researcher/Teaching assistant Department of Chemical and Biomolecular Engineering University of California, Los Angeles, USA

Publications

1. **F. Liu**, Q. Xiao, H. Wu, F. Sun, X. Liu, F. Li, Z. Le, L. Shen, G. Wang, M. Cai, Y. Lu. "Regenerative polysulfide–scavenging layers enabling lithium–sulfur batteries with high energy density and prolonged cycling life" *ACS Nano*, 11, 2697-2705 (2017).
2. **F. Liu**, Q. Xiao, H. Wu, L. Shen, D. Xu, M. Cai, and Y. Lu. "Fabrication of hybrid silicate coatings by a simple vapor deposition method for lithium metal anodes" *Adv. Energy Mater.* 1701744 (2017).
3. **F. Liu**, G. Sun, P. Oyala, S. Ma, G. Chen, X. Li, R. Tao, P. Sautet, B. Dunn, and Y. Lu. "First-principle-calculation guided design of sulfur cathodes with accelerated electrochemical reaction kinetics" (submitted).
4. **F. Liu**, J. Shen, S. Ma, L. Shen, and Y. Lu. "Ionic Liquid Tethered Metal Organic Framework for Lithium Metal Batteries" (*in preparation*).
5. **F. Liu**, G. Sun, B. Zohour, S. Senkan, P. Sautet, and Y. Lu. "Metal oxides bronze as heterogeneous catalysts for ammonia synthesis" (*in preparation*).
6. L. Shen, H. Wu, **F. Liu**, J. L. Brosmer, G. Shen, X. Wang, J. I. Zink, Q. Xiao, M. Cai, G. Wang, Y. Lu and B. Dunn. "Creating lithium-ion electrolyte with biomimetic ionic channels in metal organic framework" *Adv. Mater.*, 1707476, (2018).
7. D. Xu, H. Han, Y. He, H. Lee, D. Wu, **F. Liu**, X. Liu, Y. Liu, Y. Lu, C. Ji. "A hepatocyte-mimicking antidote for alcohol intoxication" *Adv. Mater.*, 1707443, (2018).
8. Y. Shi, H. Tang, S. Jiang, L. V. Kayser, M. Li, **F. Liu**, F. Ji, D. J. Lipomi, S. P. Ong and Z. Chen. "Understanding the electrochemical properties of naphthalene diimide: implication for stable and high-rate lithium-ion battery electrodes". *Chem. Mater.*, 30, 3508-3517 (2018).
9. F. Sun, Z. Qu, J. Gao, H. B. Wu, **F. Liu**, R. Han, L. Wang, T. Pei, G. Zhao and Y. Lu. "In situ doping boron atoms into porous carbon nanoparticles with increased oxygen graft enhances both affinity and durability toward electrolyte for greatly improved supercapacitive performance". *Adv. Funct. Mater.*, 1804190 (2018).
10. Z. Le, **F. Liu**, P. Nie, X. Li, X. Liu, Z. Bian, G. Chen, H. Wu, Y. Lu. "Pseudocapacitive sodium storage in mesoporous single–crystal–like TiO_2–graphene nanocomposite enables high–performance sodium–ion capacitors" *ACS Nano*, 11, 2952-2960 (2017).
11. F. Sun, H. Wu, X. Liu, **F. Liu**, H. Zhou, J. Gao, Y. Lu. "Nitrogen–rich carbon spheres made by a continuous spraying process for high-performance supercapacitors" *Nano Res,* 9, 3209-3221 (2016).

12. H. Zhou, Y. Peng, H. Wu, F. Sun, H. Yu, **F. Liu**, Q. Xu, Y. Lu. “Fluorine–rich nanoporous carbon with enhanced surface affinity in organic electrolyte for high-performance supercapacitors” *Nano Energy* 21, 80-89 (2016).
13. L. Shen, **F. Liu**, G. Chen, H. Zhou, Z. Le, H. Wu, G. Wang, Y. Lu. “Encapsulation of SnO_2 nanocrystals into hierarchically porous carbon by melt infiltration for high–performance lithium storage” *J. Mater. Chem. A*, *4*, 18706-18710 (2016).
14. Z. Chen, Y. Peng, **F. Liu**, Z. Le, J. Zhu, G. Shen, D. Zhang, M. Wen, S. Xiao, C. Liu, Y. Lu, H. Li. “Hierarchical nanostructured WO_3 with biomimetic proton channels and mixed ionic–electronic conductivity for electrochemical energy storage” *Nano Letter*, *15*, 6802-6808 (2015).
15. Q. Xiao, M. Gu, H. Yang, B. Li, C. Zhang, Y. Liu, **F. Liu**, F. Dai, L. Yang, Z. Liu, X. Xiao, G. Liu, P. Zhao, S. Zhang, C. Wang, Y. Lu, M. Cai. “Inward lithium–ion breathing of hierarchically porous silicon anodes” *Nature Comm.*, *6*, 8844 (2015).

Patents

1. **F. Liu**, Q. Xiao, Y. Lu, M. Cai, F. Dai, L. Yang. “Electrolyte and negative electrode structures”, U.S. Provisional Application No.: *62/090,181*.
2. **F. Liu**, D. Xu, Y. Lu, Q. Xiao, M. Cai. “Conformal coating of lithium anode via vapor deposition for rechargeable lithium ion battery”, U.S. Provisional Application No.: *15/666, 170*.
3. Y. Lu, G. Shen, J. Liu, **F. Liu**, H. Wu, J. Li. “Fuel cell with dynamic response capability based on energy storage electrodes”, U.S. Provisional Application No.: *62/413,851*.
4. Y. Lu, **F. Liu**, B. Zohour, S. Senkan. “Development of novel catalysts for ammonia synthesis”, UCLA Case No. *2017–399*.
5. Y. Lu, H. Wu, J. Liu, G. Shen, **F. Liu**. “Low–cost and effective electrocatalysts for oxygen reduction reaction”, UCLA Case No. *2017–398*.

Chapter 1 Introduction

Global climate change, which is mainly caused by carbon pollution, has already shown severe effects on the environment: rising sea levels and increased coastal flooding, more frequent wildfires and hurricanes, common infectious disease breakouts, *etc*. In the United States, transportation is the second largest source of carbon pollution. Every year, it generates around 1.7 billion tons of CO_2 emissions. Broad adaptation of electric vehicles could effectively curb the climate change by dramatically cutting emissions on a nationwide scale. Meanwhile, the global market of electric vehicles has been expanding rapidly, especially for the US and China (Figure 1.1).

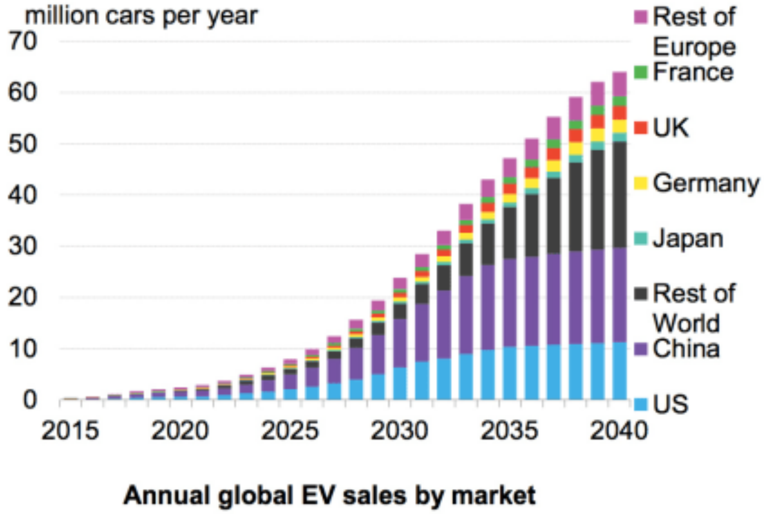

Figure 1.1 Annual global market for electric vehicles. Reproduced from Bloomberg New Energy Finance.

With the growing demand for electric vehicles and grid-scale energy storage, the development of electric energy storage materials has been driven toward higher energy density, environmental benignity and better safety (Figure 1.2)[1]. The focus of research has been moved from lithium ion batteries with liquid electrolyte toward lithium-sulfur/air batteries with solid electrolyte. Although these systems possess high theoretical energy density, they generally exhibit short cycling lifespan, as well as fast capacity degradation. The detailed problems of sulfur cathode and lithium metal anode will be introduced in Chapter 3 and Chapter 4, respectively.

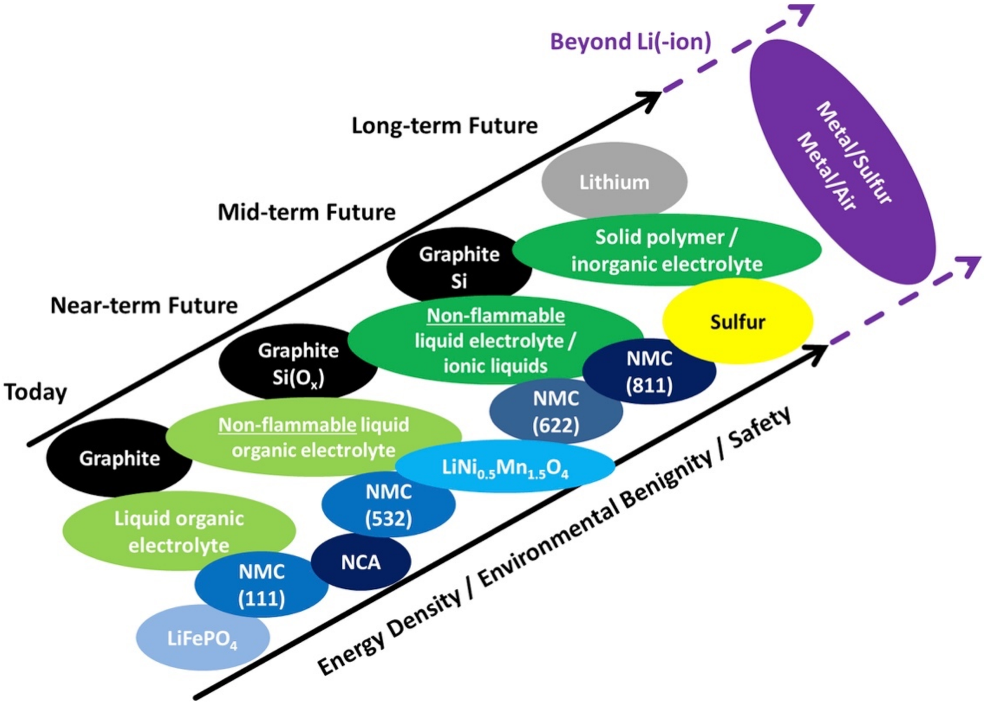
Beyond Li(-ion)
Metal/Sulfur
Metal/Air
Long-term Future
Mid-term Future
Near-term Future
Today
Lithium
Graphite
Si
Solid polymer / inorganic electrolyte
Sulfur
Non-flammable liquid electrolyte / ionic liquids
Graphite
Si(O$_x$)
NMC (811)
NMC (622)
Graphite
Non-flammable liquid organic electrolyte
LiNi$_{0.5}$Mn$_{1.5}$O$_4$
NMC (532)
Liquid organic electrolyte
NCA
NMC (111)
LiFePO$_4$
Energy Density / Environmental Benignity / Safety

Figure 1.2 Development of electric energy storage materials toward higher energy density, environmental benignity, and better safety. Reproduced from Ref. 1.

The broad adaptations of lithium-sulfur batteries have been limited by short cycling lifetime, fast capacity degradation, low sulfur utilization, and safety hazard. These issues are caused by (i) polysulfide shuttling phenomenon, (ii) slow redox kinetics of sulfur species and (iii) formation of lithium dendrites. Although researchers have demonstrated several methods to tackle these problems, the electrochemical processes in lithium-sulfur batteries remain ambiguous. The objective of this project is to unveil the fundamental limitations and challenges in lithium-sulfur batteries, and rationally design effective strategies to solve these problems. In chapter 5, we will discuss the geometric and electronic band structures of related sulfur species, as well as the correlation with their sluggish electrochemical responses. In chapter 6, we will introduce the designing concept of regenerative polysulfide-scavenging layers, which can effectively mitigate the shuttling phenomenon of polysulfides. The interactions between various metal oxides and lithium polysulfides are also detailed regarding physisorption and chemisorption. Chapter 7 presents the design of redox mediators to expedite the electrochemical behaviors of sulfur species and boost the energy density of lithium-sulfur batteries. At last, chapter 8 illustrates the fabrication of a hybrid silicate coating for lithium metal anode. Such hermetic hybrid coating combines the merit of organic and inorganic moieties and successfully suppresses the formation of dendritic structures. Together, this dissertation not only illustrates the fundamental limitation of lithium-sulfur batteries, and provides practical strategies in every aspect to solve these problems.

Chapter 2 Electrochemical energy storage with battery systems

2.1 Fundamental of electrochemical energy storage systems.

An electrochemical cell is mainly composed of two electronic conductors (electrodes), which are separated by an ionic conductor (electrolyte). Within electrodes, the charge is transported through the movement of electrons and electron holes; while within the electrolyte, the charge is carried by the movement of ions (such as H^+, Li^+ and ClO_4^-). The direction of charge movements can be manipulated by external circuits. By driving the electrodes to a more negative potential, the energy of electrons in the electrode is alleviated. When their energy is higher than the vacant electronic states of species in the electrolyte, electrons will flow from the electrode to the electrolyte (Fig. 2.1 a). Similarly, by applying a more positive potential, the energy of electrons can be lower than the occupied electronics states of species in the electrolyte, a flow of electrons from solution to the electrode will occur (Fig. 2.1 b)[2]. Given that such electron transfers cause chemical reactions that follow Faraday's law, they are often called faradaic processes. On the other hand, when electron transfers are thermal dynamically or kinetically unfavorable, adsorption or desorption can still take place over a range of potentials and such process is referred to as non-faradaic processes. Based on the different energy storage and conversion mechanisms, electrochemical cells can be categorized into electrochemical capacitors, pseudocapacitors, batteries and fuel cells.

As shown in Fig. 2.2, these devices offer a wide range of energy densities and power densities, which can meet the requirement of a wide range of applications. For instance, electrochemical capacitors can be charged in minutes or seconds, ensuring fast energy collection when connected with intermittent energy sources. On the contrary, batteries with high energy density are widely used in portable electronics, electric vehicles, grid-scale storage and so on.

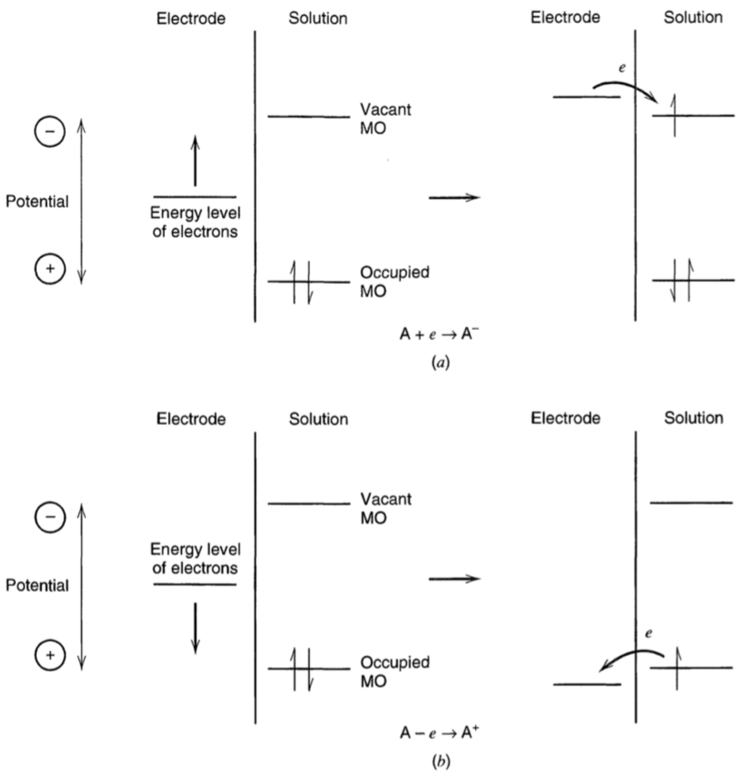
Electrode
Solution
Electrode
Solution
Potential
Energy level of electrons
Vacant MO
Occupied MO
e
$A + e \rightarrow A^-$
(a)
Electrode
Solution
Electrode
Solution
Potential
Energy level of electrons
Vacant MO
Occupied MO
e
$A - e \rightarrow A^+$
(b)

Figure 2.1 Representation of (a) reduction and (b) oxidation process of a species A/A^+. Reproduced from Ref. 2.

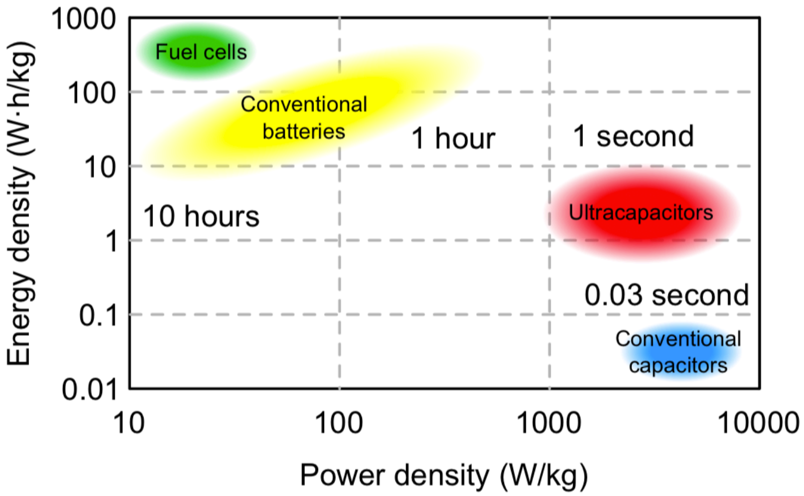

Figure 2.2 Simplified Ragone plot of the energy storage domains of various energy storage and conversion systems. Reproduced from Wikipedia.

2.1.1 Thermodynamics of cells

The energy storage and power characteristics of energy storage devices follow the same thermodynamic and kinetics theories for chemical reactions. In chemical reactions, Gibb's free energy is often used to predict the direction (or driving force) of a reversible chemical reaction under certain conditions. Similarly, in an electrochemical reaction, it is used to predict the standard electromotive force of an electrochemical process.

For a reversible electrochemical reaction, the fundamental thermodynamic equation is given by

$$\Delta G = \Delta H - T\Delta S,$$

where ΔG is the Gibb's free energy change, ΔH is enthalpy, ΔS is entropy, and T is temperature. ΔG, ΔH, and ΔS are state functions and only depend on the intrinsic properties of materials, as well as their initial and final states in the reactions. In electrochemical terms, this equation can also be written as

$$\Delta G = -nFE,$$

where n is the number of electrons transferred by per molar of reactant, F is the Faraday constant and E is the voltage of the cell. The equilibrium constant of the reaction (K) can be derived as

$$RT \ln K = -\Delta G = nFE.$$

2.1.3 Kinetics of electrode reactions

While thermodynamics describes the equilibrium state of the system, kinetics describes the rate of the charge transfer process. The kinetics of an electrochemical reaction can be expressed with Arrhenius equation

$$k = Ae^{-\frac{E_a}{RT}},$$

where E_a is the activation energy, A is a frequency factor, R is gas constant and T is temperature.

However, the electrode reactions in batteries are more complicated than chemical reactions. It is composed of several physical, chemical and electrochemical steps, such as charge transfer and charge transport reactions. The rate of these individual steps determines the overall kinetics of the electrode reactions. In general, there are three kinds of polarizations in cells: activation polarization, ohmic polarization, and concentration polarization. Activation polarization is correlated with the kinetics of charge-transfer process at the interphase between electrode and electrolyte; Ohmic polarization results from the contact resistant between cell components; Concentration polarization is determined by mass transport limitations at the end of the electrochemical process (Fig. 2.3)[3].

The rate (or current i) of a charge-transfer-controlled reaction can be given by Butler-Volmer equation as

$$i = i_o\left[e^{-\alpha f\eta} - e^{(1-\alpha)f\eta}\right],$$

where i_o is the exchange current of electrochemical reaction, α is transfer coefficient, f is the frequency of rotation and η is overpotential. Meanwhile, we can also use the Tafel plot (log i *vs.* η) to evaluate these kinetic parameters.

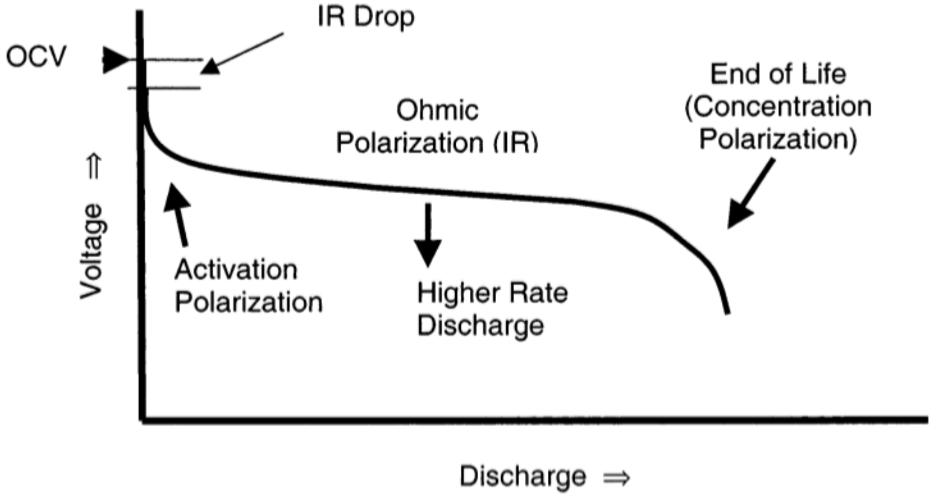

Figure 2.3 Typical discharge curve of a battery, showing three different kinds of polarization. Reproduced from Ref. 3.

2.2 Current state-of-the-art

2.2.1 Lithium-ion batteries with insertion chemistry

For the last decade, lithium-ion batteries have dominated the market of portable electronics, hybrid/electric vehicles, as well as grid-scale energy storage. Although the commercial lithium-ion technology has achieved a gravimetric energy density of 250 Wh kg^{-1} and a volumetric energy density of 650 Wh L^{-1}, their development has reached bottleneck due to their lithium insertion/desertion chemistry and the limited voltage window of organic liquid electrolytes.[4]

The most mature lithium-ion anode is based on graphite, which provides a theoretical capacity of 372 mAh g^{-1} and a low operating voltage of 0.1 V (*vs*. Li/Li^+). During lithiation, lithium ions occupy the interlayer space of graphite and induce ~ 13.2 % volumetric expansion[5]. Since the stable electrolyte window is above its working voltage, a chemically stable solid electrolyte interphase (SEI) layer is formed on its surface through the decomposition of liquid electrolyte components. However, such SEI offers insufficient Li^+ conductance and limits the rate performance of graphite anode. Moreover, the large overpotential during high-rate operation induces the local formation of lithium dendrites, which imposes the concerns of short-circuiting and cell explosion.

Commercial cathode materials are generally based on transition metal oxides, such as $LiCoO_2$, $LiMn_2O_4$, $LiFePO_4$. Their working voltage ranges from 3.4 V to 5 V and presents distinct electrochemical behaviors. Among these three, materials with layered structures exhibit the highest specific density (~180 mAh g^{-1}), but suffer from more rapid capacity degradation due to chemical/structure instability. On the contrary, $LiFePO_4$ presents good stability and safety, but a lower operating voltage of 3.4 V (*vs*. Li/Li^+) and limited practical capacity of 160 mAh g^{-1}.

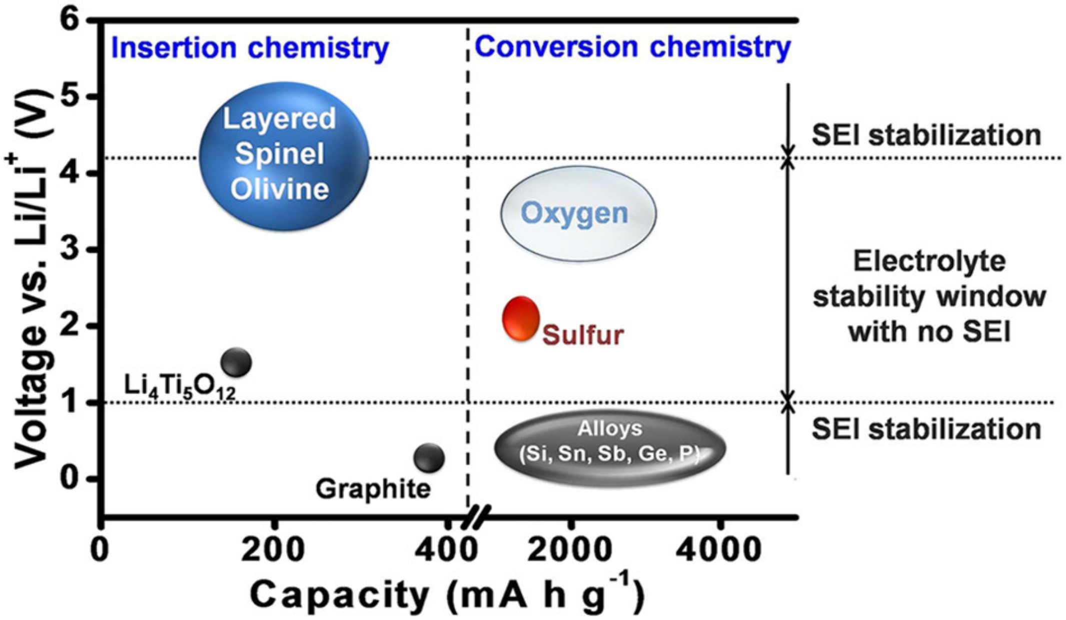

Figure 2.4. Capacity and voltage ranges of anode and cathode materials for lithium-based batteries. Reproduced from Ref. 4.

2.2.1 Post lithium-ion batteries with conversion chemistry

With the increasing demand for batteries with even higher energy density and power density, many materials with conversion chemistry have obtained tremendous attention during the last few years, such as metallic lithium, silicon, sulfur, oxygen and so on. In general, these materials can be converted into entirely new products during lithiation and offer a magnitude higher theoretical capacities comparing to conventional insertion-type materials. Moreover, they offer low prices without the use of precious metals, such as cobalt.

Unfortunately, the conversion reactions also dramatically change the electrode structure and some intrinsic properties of the active materials. For instance, silicon can form silicon-lithium alloys during lithiation and provide a high theoretical capacity of 3575 mAh g^{-1}. Meanwhile, such conversion is accompanied with a large volumetric expansion around 300%, which causes mechanical fractures, pulverization of electrodes, as well as repetitive side-reactions with liquid electrolyte. A number of strategies have been developed to address these issues, such as nanosized silicon[6], silicon-carbon composites[7], porous silicon particles[8], as well as conductive[9] and self-healing polymers[10] as binders. Although these methods mitigated the problems to some extent, some of them also lowered the overall energy density of cells, making them unfavorable for practical applications.

2.3 Conclusion

Lithium-ion batteries have been successfully transformed into the power sources for portable electronics and enabled the prototype hybrid/electronic vehicles, but they are unable to meet the market demands for even higher energy densities and power outputs. Meanwhile, post-lithium-ion batteries based on conversion reactions are promising next-generation electrical energy storage systems. Although they are still facing tremendous challenges at the current stage, their practical applications can be realized in the near future with the fundamental understanding of the battery operation processes.

Chapter 3 Sulfur cathode

3.1 Introduction

With the rapidly rising demands of batteries with high energy density and power density, lithium-sulfur batteries have attracted tremendous attention during last few years owing to its high theoretical energy density (2800 Wh L^{-1}, 2500 Wh kg^{-1}) and low cost. Despite the extensive research and development during the past decade, its application is still challenged by a number of practical problems, such as low sulfur utilization, polysulfide shuttling phenomenon, and short cycling life. Most of these problems are associated with the intrinsic property of sulfur species. In this chapter, we will discuss the electrochemical limitations of the sulfur cathode and some representative strategies.

3.2 Electrochemical reactions of lithium-sulfur battery

To date, S_8 and Li_2S have been widely used as the active materials in lithium-sulfur batteries. Both materials have advantages and disadvantages for practical application. S_8 is not sensitive to air and thus lowers the difficulty of electrode preparation. Meanwhile, it does not contain lithium and has to be paired with a lithium-containing anode, such as metallic lithium anode and pre-lithiated tin/silicon anode. Besides, it goes through large volumetric expansion (80%) during lithiation, leading to the pulverization of the electrode structures and low utilization of active species. On the contrary, Li_2S is air-sensitive and thus electrodes have to been prepared and dried in an argon-filled glove box. Given that sulfur element is fully lithiated, the option of anode materials is not limited to metallic lithium. Silicon or tin-based compounds can also be employed as the counter electrode with much-improved safety. The volumetric expansion of active materials is also eliminated and the stability of the electrode structure can be potentially improved.

Despite the differences in cell configurations and starting materials, the electrochemical process in cathode remains the same. The overall electrochemical reaction is

$$S_8 + 16\ \mathrm{Li} \leftrightarrow 8\ \mathrm{Li_2S},\ E^0 = 2.15\ \mathrm{V}\ (vs.\ \mathrm{Li/Li^+})$$

This conversion reactions of sulfur species are far more complicated than the insertion chemistry in conventional lithium-ion batteries. It is composed of several electrochemical steps that involve several sulfur intermediates, including elemental sulfur (solid), lithium polysulfide in solution (Li_2S_n, $4 \leq n \leq 8$), lithium persulfide (Li_2S_2, solid), lithium sulfide (Li_2S, solid) and so on.

The representative voltage profile of lithium-sulfur battery is shown in Figure 3.1. During the discharge process, S_8 is consequentially reduced to higher-order lithium polysulfides (Li_2S_n, $6 < n \leq 8$) and lower-order lithium polysulfides (Li_2S_n, $2 < n < 6$). There are two voltage plateaus at 2.3 V and 2.1 V with ether-based electrolyte, corresponding to the reduction from S_8 to Li_2S_4 and reduction from Li_2S_4 to Li_2S, respectively. At the end of the discharge process, Li_2S is formed as the final discharge product. Similarly, during the reversed charge process, Li_2S is concerted back to S_8 through the generation of lithium polysulfides.

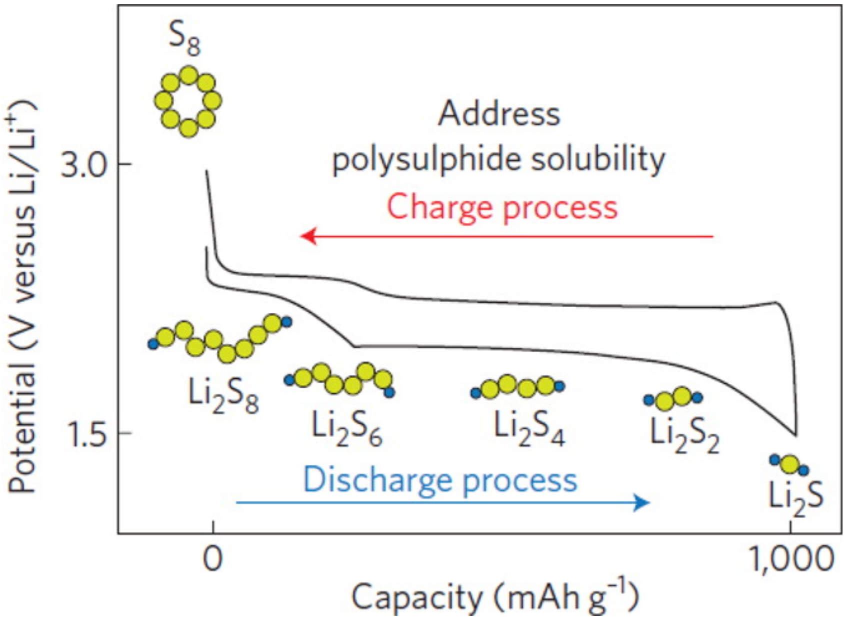

Figure 3.1 Voltage profile of Li-S battery. Reproduced Ref. 11.

With the development of modern technologies and computational method, the understanding of this electrochemical process becomes more comprehensive. IR and Raman spectroscopic studies have been widely used to probe the transformation of different sulfur species. However, given that the complete pure intermediate phase is difficult to obtain (if not impossible), the peaks in UV-Vis, IR and Raman spectroscopies are not readily assigned. To distinguish different sulfur species, Kawase and his colleagues converted Li_2S_n species to benzylized polysulfide (Bz_2S_x) molecules without changing the number of sulfur atoms, and further analyzed them using liquid chromatography-mass spectrometry (LC/MS) and magnetic resonance spectrometry (^{1}H NMR) (Figure 3.2). With the assistance of this organic conversion technique, they suggested that the first voltage plateau at 2.3 V and the subsequent transition stage are associated with multiple reactions that involve S_8, Li_2S_6, Li_2S_5, Li_2S_4, Li_2S_3, Li_2S_2, and Li_2S, while the reduction/oxidation of Li_2S_3 dominates the discharge voltage plateau at 2.1 V. The authors also claimed that higher-order lithium polysulfides are responsible for the redox shuttling phenomenon, which causes capacity degradation.

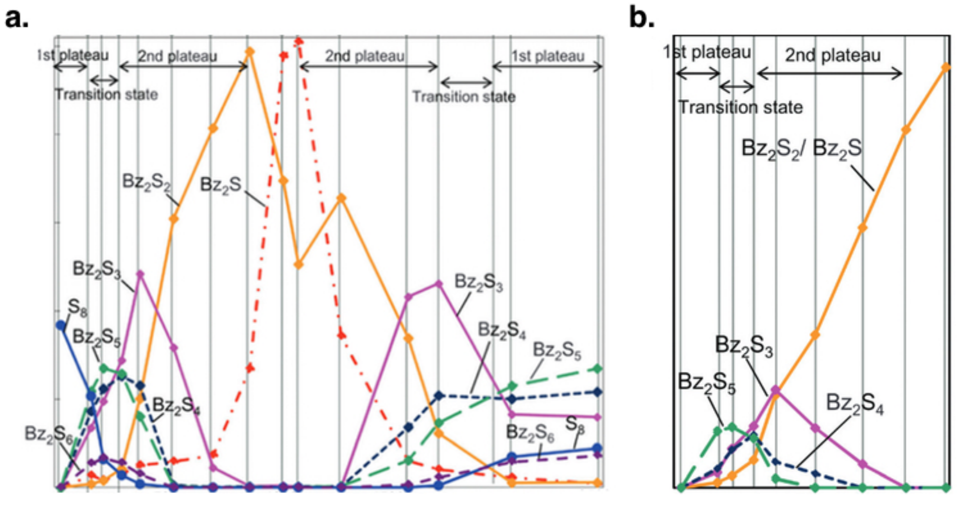

Figure 3.2 Relative quantity of sulfur species obtained from **a.** LC/MS and **b.** ^{1}H NMR result. Reproduced from Ref. 12.

The molecular structures of sulfur intermediates have also been systematically investigated using density functional theory (DFT)[11]. As shown in Figure 3.3, short-chain lithium polysulfides (Li_2S_n, $1 \leq n \leq 3$) present a linear structure, while long-chain lithium polysulfides (Li_2S_n, $4 \leq n \leq 8$) exhibit a ring structure. Liu *et al.* also pointed out that the linear structure will transform into a cyclic structure during structural optimization, providing essential insights for cathode structure design.

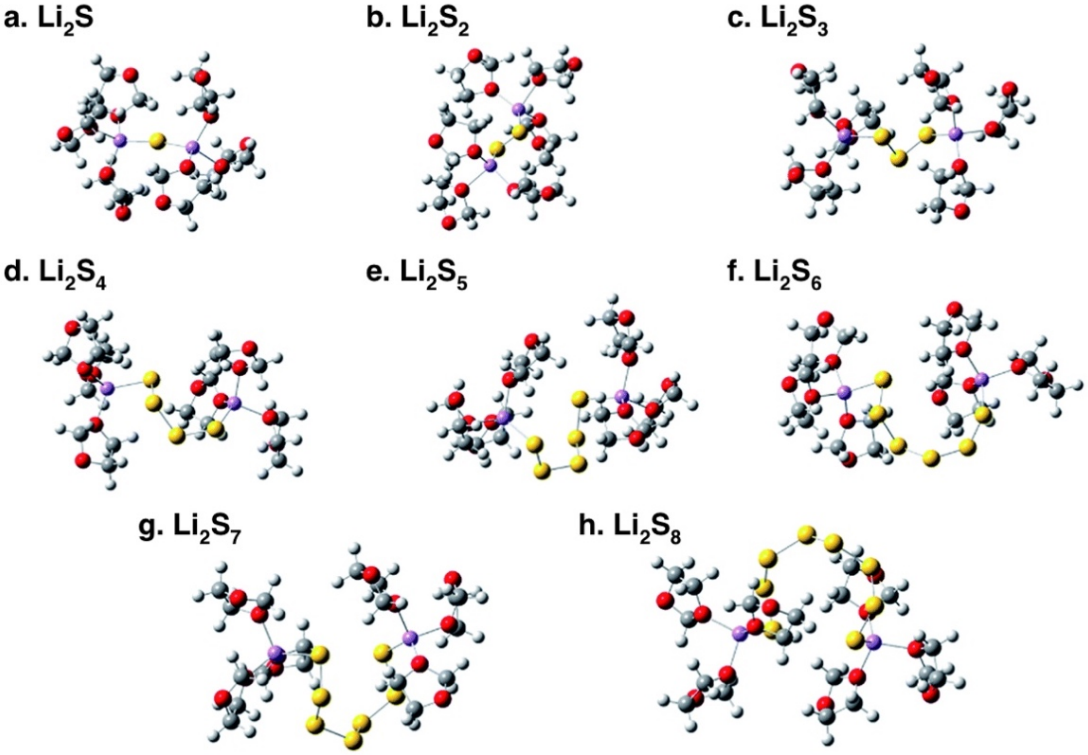

Figure 3.3 (**a-h**) The solvated structures of lithium polysulfides (Li_2S_n, $1 \leq n \leq 8$) in DOL solvent. Reproduced from Ref. 13.

Besides closed-shell lithium polysulfides, sulfur radicals have also been predicted by first principle calculations[12] and detected with the assistance of ^{7}Li NMR spectroscopy[13], electron magnetic resonance spectroscopy (EPR)[12,14], X-ray absorption near-edge structure spectroscopy (XANES)[15] and so on. As shown in Figure 3.4, the EPR spectra of both Li_2S_4 and Li_2S_6 solutions illustrate a typical rhombic S = 1/2 EPR signal at low temperatures ($g_x = 2.0028$, $g_y = 2.0333$, $g_z = 2.0535$ and $g = 2.0282$), and Vijayakumar *et al.* indicated that their result is consistent with that of S_3 free radicals in literature. The authors also proposed that lithium polysulfides can undergo dissociation reactions to produce S_3 radicals, which can also participate in the shuttling phenomena along with its parent S_6^{2-} molecules.

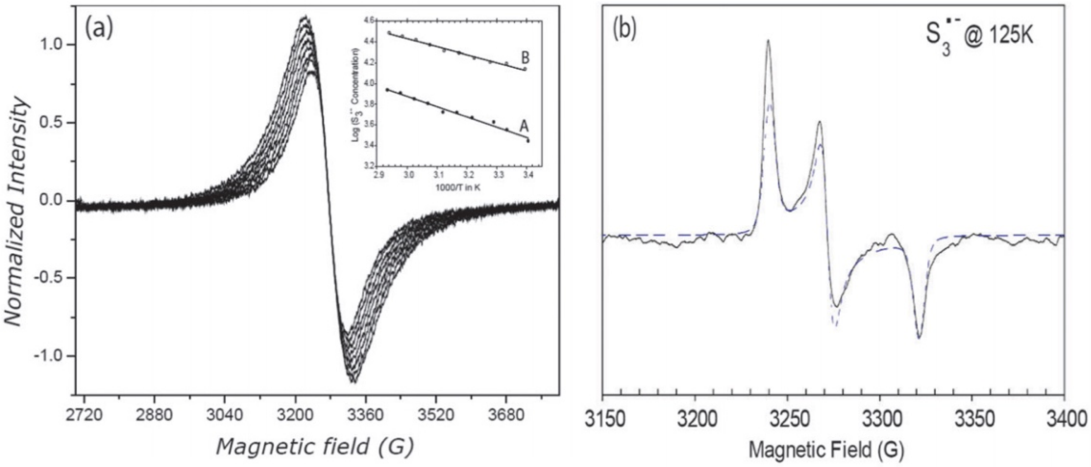

Figure 3.4 ESR spectra of Li_2S_6 solution, showing the presence of S_3 free radical ions. (b) The ESR spectra of Li_2S_6 solution at 125 K showing the characteristic S = 1/2 EPR spectra. Reproduced from Ref. 14.

Wujcuk *et al.* conducted first principle calculations regarding the structures of various sulfur species and their corresponding XANES spectra, including lithium polysulfides, sulfur radicals, and crystalline lithium sulfide. As shown in Figure 3.5, lithium atoms are located at the center of the sulfur chains, forming stable radical structures. The authors also assigned the characteristic peaks to different transition modes. Furthermore, they found that sulfide radicals and high order polysulfide dianions dominate the electrolyte composition after the early stage of discharge. As discharge proceeds, sulfur radicals are consumed before polysulfide dianions. At the end of the discharge process, sulfur species are all converted to low-order lithium polysulfides and Li_2S.

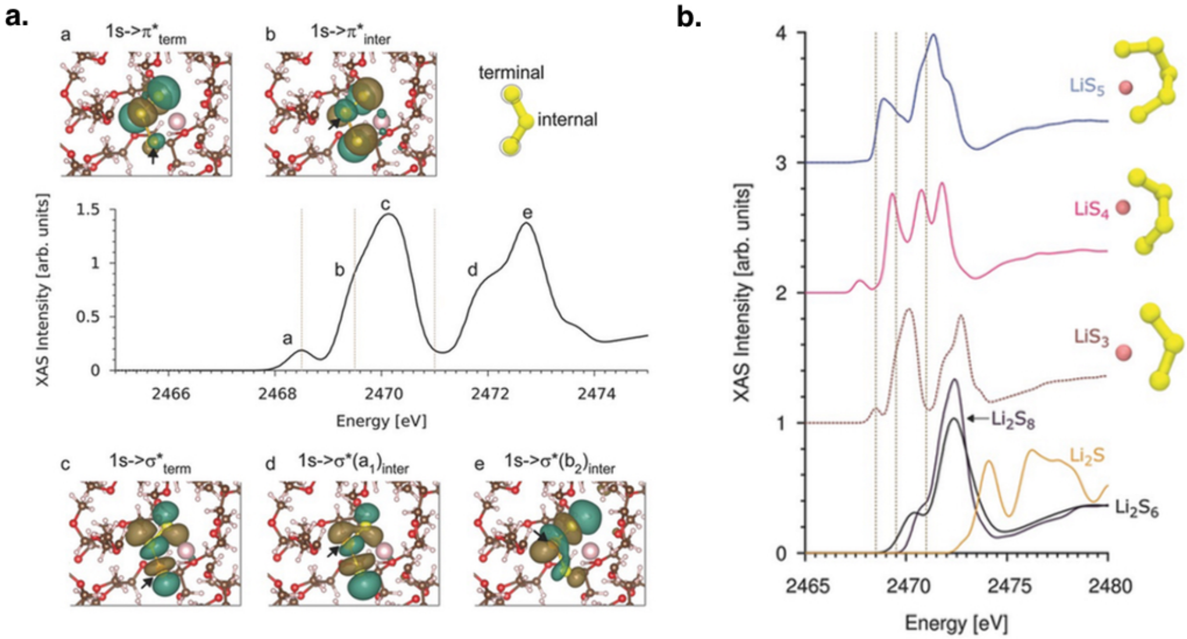

Figure 3.5 a. First principle XANES spectra of LiS_3 radical in TEGDME solvent with five transition states. The carbon (grey), oxygen (red), and hydrogen (silver) in TEGDME molecules are near LiS_3 radicals are shown here. Lithium ions are shown as pink spheres. **b.** Structures and the calculated K-edge XANES spectra of LiS_5, LiS_4 and LiS_3 radicals, Li_2S_8 and Li_2S_6 molecules, and crystalline Li_2S. Reproduced from Ref. 17.

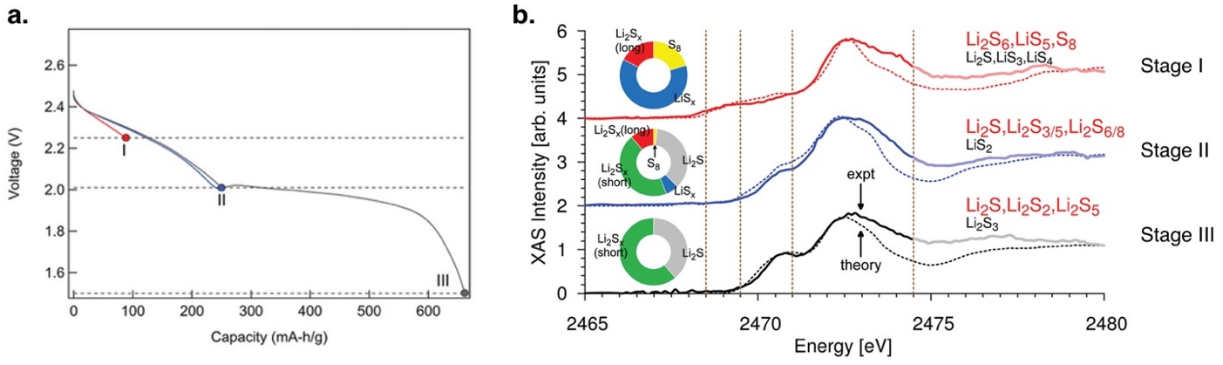

Figure 3.6 a. Discharge profile of lithium-sulfur battery. **b.** Comparison of the best-fit spectra from theory and XAS measurement for the three voltages in **a**. Reproduced from Ref. 17.

3.3 Fundamental problems

Currently, the problems that are impeding the commercialization of lithium-sulfur batteries have resulted from the intrinsic properties of sulfur species. The electronic conductivities of sulfur species are extremely low, especially the solid products S_8 (1×10^{-15} S/m) and Li_2S (1×10^{-16} S/m). Such low electronic conductivity requires high activation energies and large overpotentials to drive the electrochemical reactions and limits their power output. Meanwhile, the conversion reactions of sulfur, which endow them with high theoretical capacities, lead to large volumetric expansions and the pulverization of sulfur electrodes. The loose contact between electrode components results in the low utilization of sulfur species and the corresponding fast capacity degradation. Furthermore, polysulfide shuttling is originated from the high solubility of lithium polysulfides in the electrolyte and their reactivity with metallic lithium. Tuning the intrinsic properties of sulfur through introducing catalytic agents or conducting agents into sulfur electrodes can potentially improve their redox kinetics. Moreover, by introducing blocking layers between two electrodes or on the surface of two electrodes can mitigate the outward diffusion of sulfur intermediates and thus enhance the capacity retention rate.

3.4 Current strategies

3.4.1 Carbon host materials

During the early stage of development, porous carbon scaffolds have been widely used as the major hosting materials for sulfur species to improve their electronic conductivity and enable the operation of lithium-sulfur batteries. One of the examples is the encapsulation of elemental sulfur in the PEG-modified CMK-3 (Figure 3.7a).[16] Nazar *et al.* demonstrated efficient utilization of sulfur species and reached 80% of their theoretical capacity. The authors also proposed that the carbon framework not only acts as an electronic conduit to the encapsulated sulfur species but serves as a reaction chamber that retards the outward diffusion of lithium polysulfides. Later on, various conductive porous scaffolds have been employed as host materials for sulfur-based cathodes, including carbon nanotubes[17], carbon nanofibers[18], graphene (Figure 3.7 b)[19,20], porous carbon[21,22] and their hybrids[23-25]. Although improved electrochemical performances have been achieved, the areal mass loading of sulfur is generally limited to 2 mg cm^{-2}. The energy density of such Li-S cells is far below that of the commercialized 18650 lithium-ion battery[26].

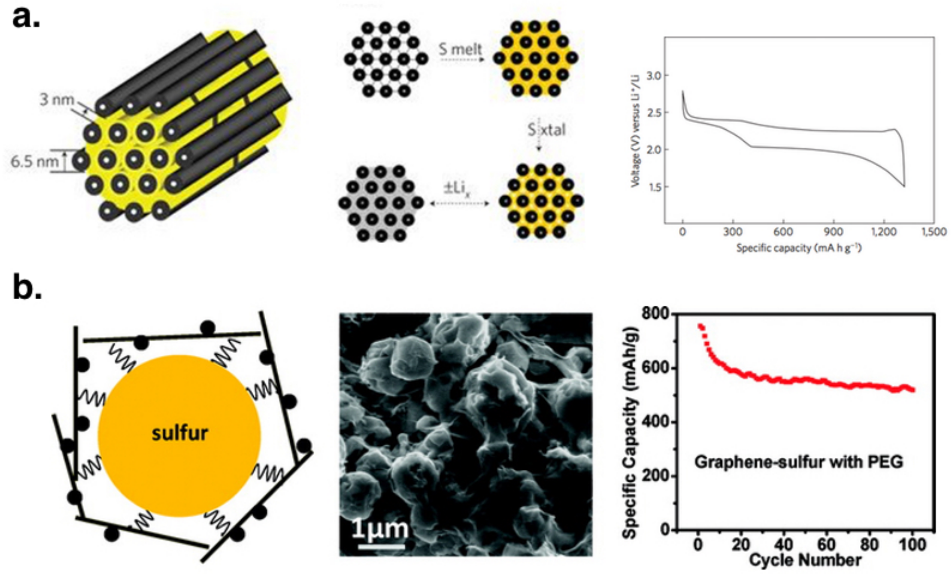

Figure 3.7 Illustration of **a.** Sulfur encapsulation in CMK-3 and **b.** Graphene wrapped sulfur microparticles. Reproduced from Ref. 18 and Ref. 19.

To improve the interactions between the conducting network and sulfur species, multiple heteroatoms have also been also doped into carbon structures during their fabrication process, including nitrogen[27-29], phosphate[30], sulfur[31], and so on. Peng *et al.* performed first principle calculations based on density functional theory, investigating the interactions between undoped/nitrogen-doped carbon atoms and sulfur species (Figure 3.8)[32]. Their results reveal the strong interactions between pyridinic/quaternary N regions and polar Li_2S/polysulfide species. As shown in Figure 3.8 h, the positively charged lithium atoms can directly bind to the electron-rich pyridinic N sites, suggesting a strong interaction derived from electron donating and accepting.

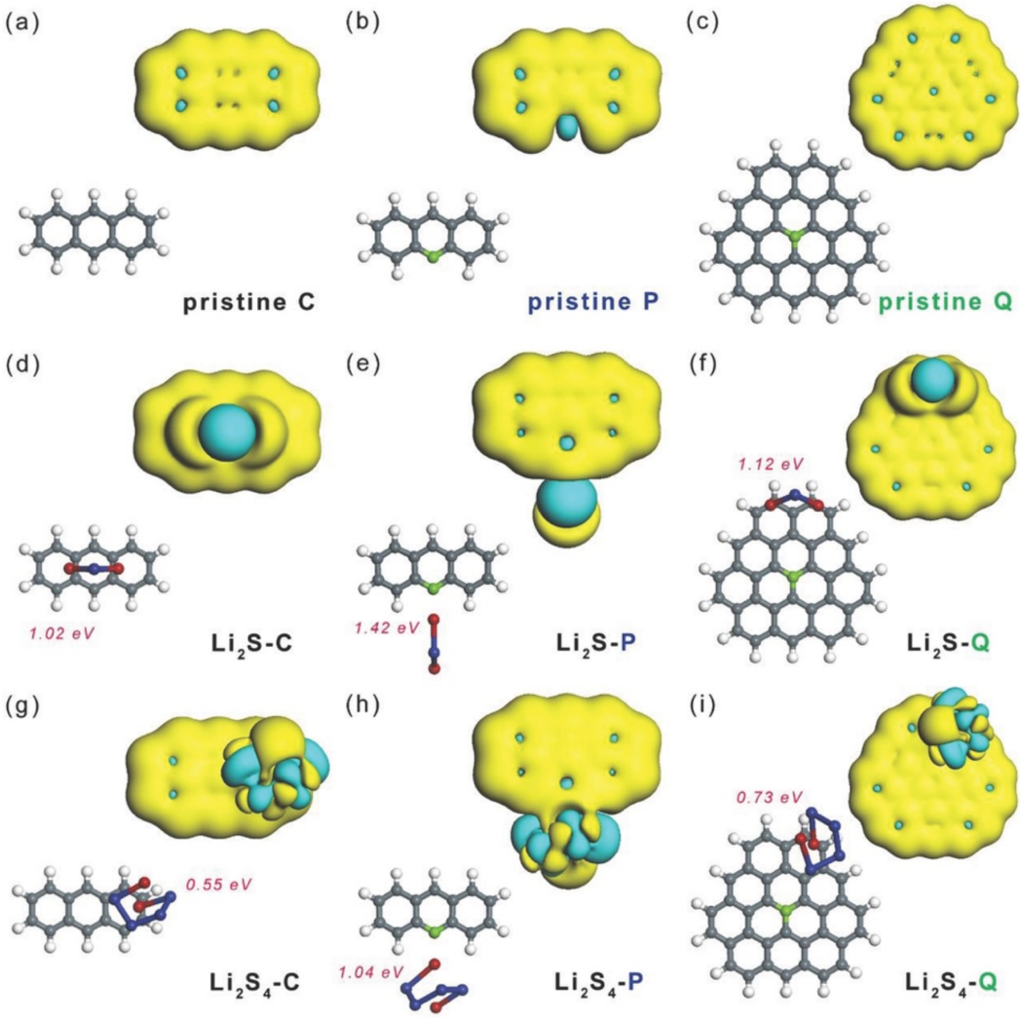
(a)
pristine C
(b)
pristine P
(c)
pristine Q
(d)
1.02 eV
Li$_2$S-C
(e)
1.42 eV
Li$_2$S-P
(f)
1.12 eV
Li$_2$S-Q
(g)
0.55 eV
Li$_2$S$_4$-C
(h)
1.04 eV
Li$_2$S$_4$-P
(i)
0.73 eV
Li$_2$S$_4$-Q

Figure 3.8 First principle calculation of the interactions between undoped/nitrogen doped carbon atoms and sulfur species. Reproduced from Ref. 32.

Figure 3.9 presents one of the examples of nitrogen-doped porous carbon scaffold developed by Song *et al*.[28] The author successfully demonstrated an areal capacity of 6 mAh cm^{-2} with a mass loading (sulfur) of 5 mg cm^{-2} over 200 cycles. They attributed such exceptional electrochemical performance to the nitrogen functional groups that enable the effective trapping of lithium polysulfides to the electroactive sites, which is consistent with the simulation results above.

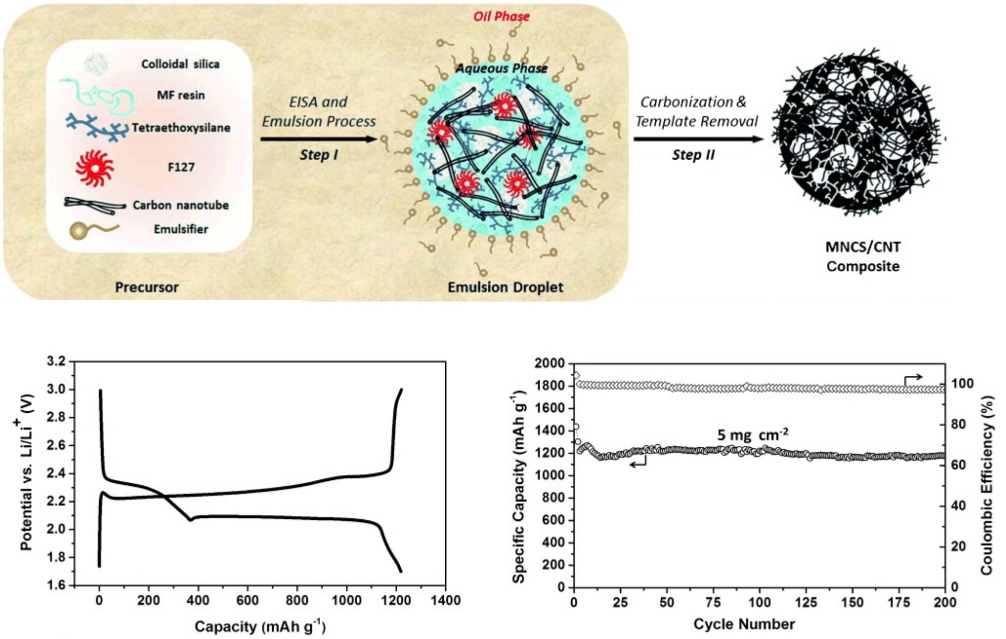

Figure 3.9 Synthesis process of nitrogen-doped mesoporous carbon sphere and CNT composites, as well as the electrochemical performances of lithium-sulfur batteries based on such composites. Reproduced from Ref. 28.

3.4.2 Interfacial engineering

Lithium-sulfur batteries that based on carbonaceous hosts generally exhibit sluggish redox kinetics, especially for electrodes with high sulfur loadings. This is caused by the weak interactions between non-polar carbon materials and polar lithium polysulfides. Besides heterogenous atom doping, researchers also developed other polar materials, such as metal oxides/sulfides/nitrides/carbides, and investigated their influences on the electrochemical process. Peng *et al.* pointed out the importance of polar and conductive in promoting the conversion of lithium polysulfides and the precipitation of lithium sulfides (Figure 3.10 a)[33]. The author explained that the electrochemical kinetics is determined by the efficient adsorption of active species to the surface, as well as fast electron transport of electrons to the reactive intermediates. First principle calculations also showed increased binding energies between TiC and sulfur species.

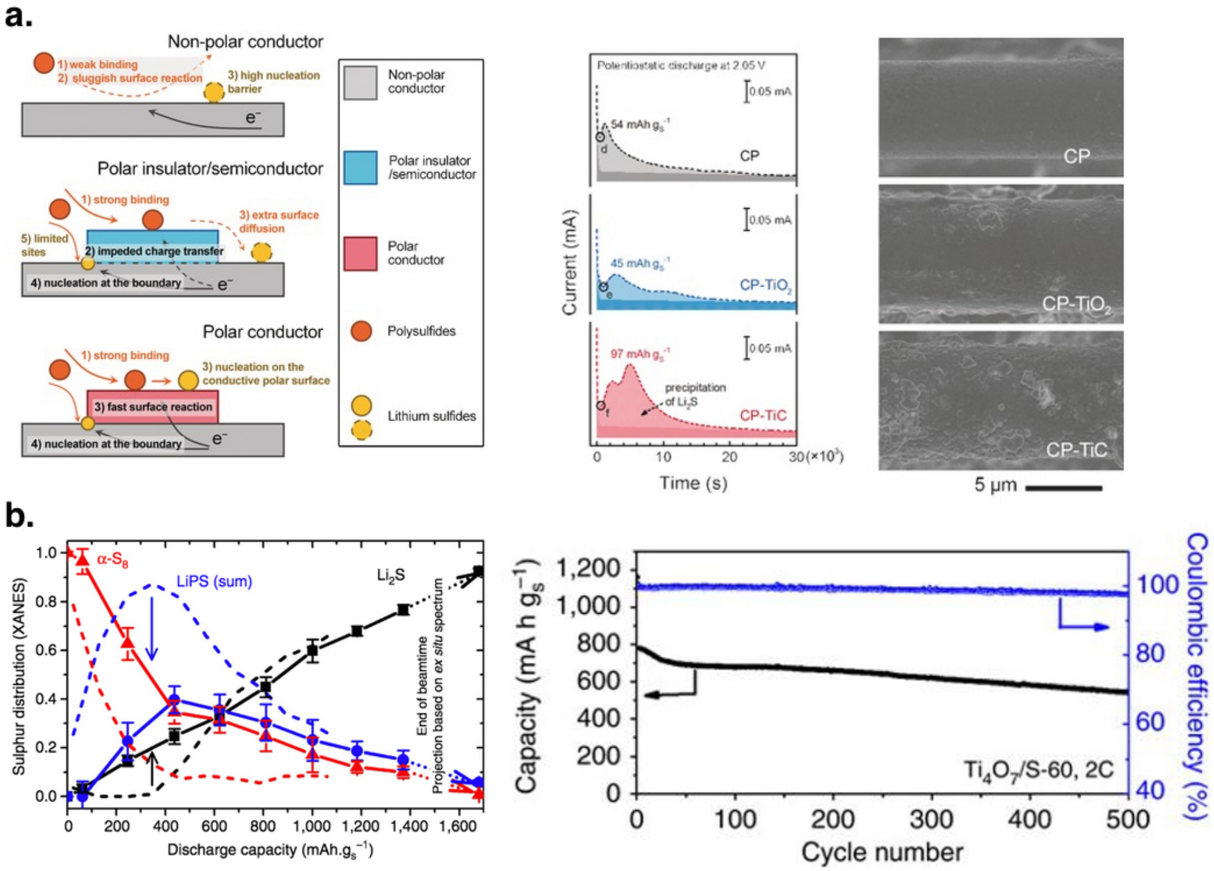

Figure 3.10 a. Schematic illustration of working mechanisms of non-polar conductors, polar insulator/semiconductors, and polar conductors. **b.** Illustration of surface-mediated reduction of Li_2S from lithium polysulfides on metallic polar host Ti_4O_7. XANES results illustrate the distribution of sulfur species during discharge. The results of Ti_4O_7/S are shown in solid lines while that of VC-S are presented in dash lines. Reproduced from Ref. 33 and Ref. 34.

The strong affinity between lithium polysulfides and host materials has also been observed in metallic oxide Ti_4O_7. The distribution of sulfur species was determined by XANES (Figure 3. 10 b). The author observed sudden precipitation of Li_2S on the surface of carbon and a gradual deposition on the surface of Ti_4O_7. Such different electrode structure evolution can lead to distinct electrochemical performances. Stable cycling performance has been demonstrated with more than 500 cycles under 2 C rate.[34]

3.4.3 Functional interlayers

Since 2012, polysulfide-reactivation layer has been intensively developed to block the diffusion of lithium polysulfides and reactive the trapped active species. The first demonstration is the SWCNT-modulated separator designed by Manthiram's group (Figure 3.11 a)[35]. By placing such functional interlayer between two electrodes, not only is the electrochemical stability of sulfur cathode significantly improved, but the corrosion of lithium metal anode is also alleviated. Later on, polymeric materials are further incorporated into the interlayer to decrease porosity and slow down the migrations of lithium polysulfides (Figure 3.11 b). For instance, Nafion, which possess negatively charged functional group -SO_3^-, allows the effective transportation of positively charged lithium cations while rejecting the negatively charged S_n^{2-}, resulting in improved electrochemical stability.[36]

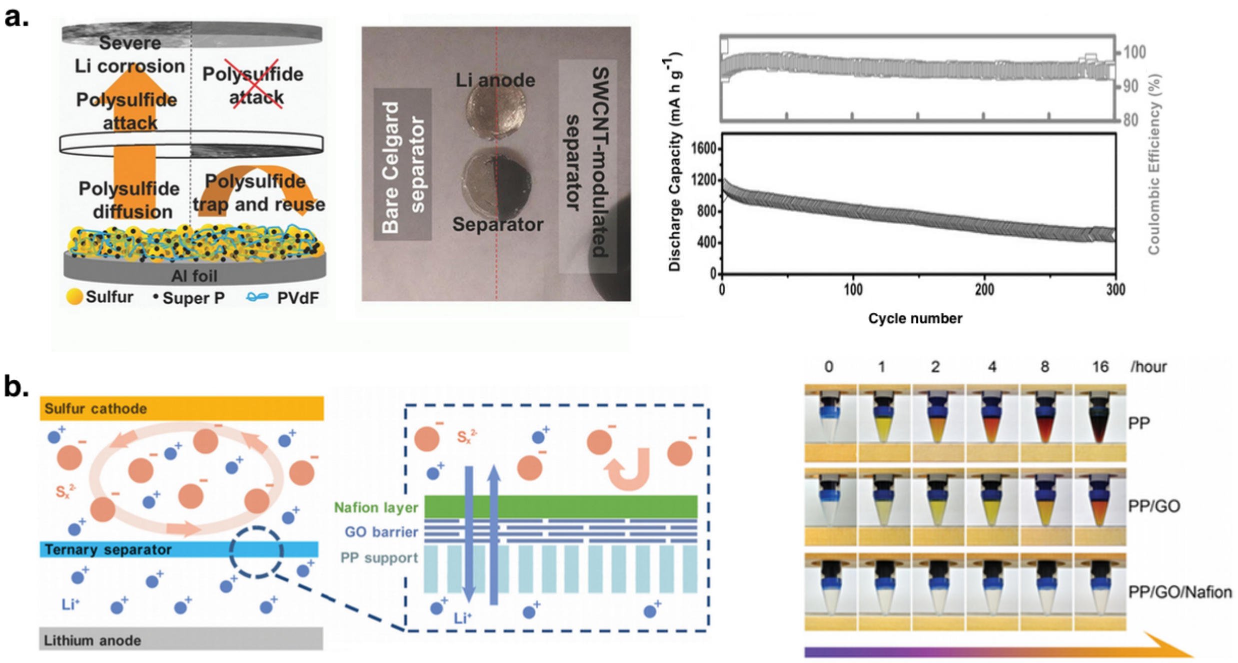
a.
Severe
Li corrosion
Polysulfide
attack
Polysulfide
attack
Polysulfide
diffusion
Polysulfide
trap and reuse
Al foil
Sulfur
Super P
PVdF
Bare Celgard separator
Li anode
Separator
SWCNT-modulated separator
Discharge Capacity (mA h g-1)
Coulombic Efficiency (%)
Cycle number
0
100
200
300
400
800
1200
1600
80
90
100
b.
Sulfur cathode
Sx2-
Ternary separator
Li+
Lithium anode
Nafion layer
GO barrier
PP support
0
1
2
4
8
16
/hour
PP
PP/GO
PP/GO/Nafion

Figure 3.11 a. Working mechanisms of the SWCNT-modulated separator in the lithium-sulfur battery. **b.** Illustration of ternary separator based on PP/GO/Nafion layers and their effective blocking effect toward lithium polysulfides. Reproduced from Ref. 35 and Ref. 36.

3.5 Conclusion

Lithium-sulfur battery has been regarded as one of the most promising electric energy storage systems for next-generation. After years' of research and development, the electrochemical performances of lithium-sulfur batteries have been dramatically improved from every aspect. Although the energy density of current lithium-sulfur batteries is comparable to the benchmark lithium-ion batteries, the cycling life is much shorter. Moreover, the utilization of highly reactive metallic lithium is also raising tremendous safety concerns. Future investigation should combine fundamental study, theoretical calculations with experimental data to guide and expedite the development of mature lithium-sulfur technologies.

Chapter 4 Lithium metal anode

4.1 Introduction

Lithium metal battery is one of the most promising candidates for next-generation electric energy storage systems, especially for applications in transportation and grid-scale energy storage. Lithium metal anode presents a high theoretical capacity of 3860 mAh g^{-1}, as well as a lowest electrochemical potential (-3.04 V *vs.* SHE). Replacing current graphite anode in lithium-ion batteries (250 Wh kg^{-1}) with LMA can significantly increase the cell's specific energy by 35% and energy density by 50%.[37] More importantly, Li-S batteries and Li-air batteries can further boost the energy density to 650 Wh kg^{-1} and 950 Wh kg^{-1}, respectively.[38] Nowadays, two challenges are the safe operation of lithium metal battery, and their short cycling life. In this chapter, we will discuss the models of lithium dendrite growth and some strategies to stabilize their electrochemical performances.

4.2 Electrochemical reactions of lithium metal anode

4.2.1 Electrochemical limitations

With the emergence of lithium-ion batteries, lithium metal batteries were abandoned by industry in early 1990, mainly because of its safety hazards. As shown in Figure 4.1 a-b, the insertion chemistry of graphite prevents the formation of lithium dendrites, while such a phenomenon is widely observed in lithium anode.[39,40] Such dendritic structure can penetrate through the separator and result in the internal short circuit, which is the primary cause of thermal runaway and even explosion. The repetitive formation of lithium dendrites can lead to the continuous consumption of electrolyte components and the growth of solid electrolyte interphase (SEI), while the dissolution of lithium dendrites sometimes results in the generation of "dead" lithium, which loses contact with the current collectors and becomes electrochemically inactive.

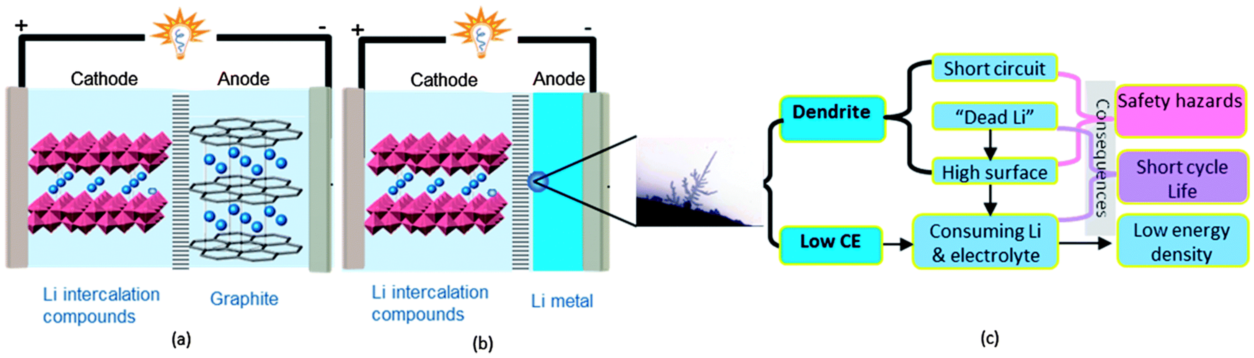
+
-
Cathode
Anode
Li intercalation compounds
Graphite
(a)
+
-
Cathode
Anode
Li intercalation compounds
Li metal
(b)
Dendrite
Low CE
Short circuit
"Dead Li"
High surface
Consuming Li & electrolyte
Consequences
Safety hazards
Short cycle Life
Low energy density
(c)

Figure 4.1 Illustration of different working mechanisms of **a.** lithium-ion batteries and **b.** lithium metal batteries. **c.** The typical morphology of lithium dendrites and the associated problems. Reproduced from Ref. 39.

4.2.2 Theoretical models

One of the models is developed by Rosso *et al.*,[41-44] and they started with the concentration gradient of lithium cations near the interface and derived the following equation

$$\frac{\partial C}{\partial x}(x) = \frac{J\mu_a}{De\,(\mu_a + \mu_{Li^+})}$$

where J is the electrode current density, D is the diffusion coefficient, e is the electronic charge, μ_a and μ_{Li^+} are the anionic and cationic mobility, respectively. When the concentration of lithium cations is approaching to zero at the interface

$$i.e., (dC/dx) > 2C_0/L$$

the Sand's time can be expressed as $\tau = \pi D\left(\frac{eC_0}{2Jt_a}\right)^2$

$$t_a \approx 1 - t_{Li^+} = \frac{\mu_a}{\mu_a + \mu_{Li^+}}$$

where t_a and t_{Li^+} are the anionic and cationic transference number, respectively. When the transference number of lithium cations approaches to unity, the Sand's time reaches infinity, in other words, the dendritic structure will not be formed on the surface. They also observed that under high-current density regions, dendrites first appear as predicted by the Sand's time, and earlier and earlier during subsequent cycles. Under low-current-density region, the onset of dendrite formation can't be explained with Sand's time, but their growth velocity still follows Chazalviel's model[45].

Another model is developed by Newman *et al.* regarding the influence of mechanical strength on the stability of lithium/polymer interface and their special deformation profiles.[46] For a compressible polymer, the gridlines at the interface are allowed to change when lithium deforms; while for an incompressible polymer, the area between gridlines in the deformed state remains identical to that of undeformed state. Although the mechanical strength of polymers has small differences in the displacement distribution on the surface, it significantly influences the forces that placed on the interface. Here the authors defined a deformation parameter (∇μ) to describe the thermodynamic properties of the interface. As shown in Figure 4.2 b, the total of the forces equals zero when the shear modulus is twice that of lithium.

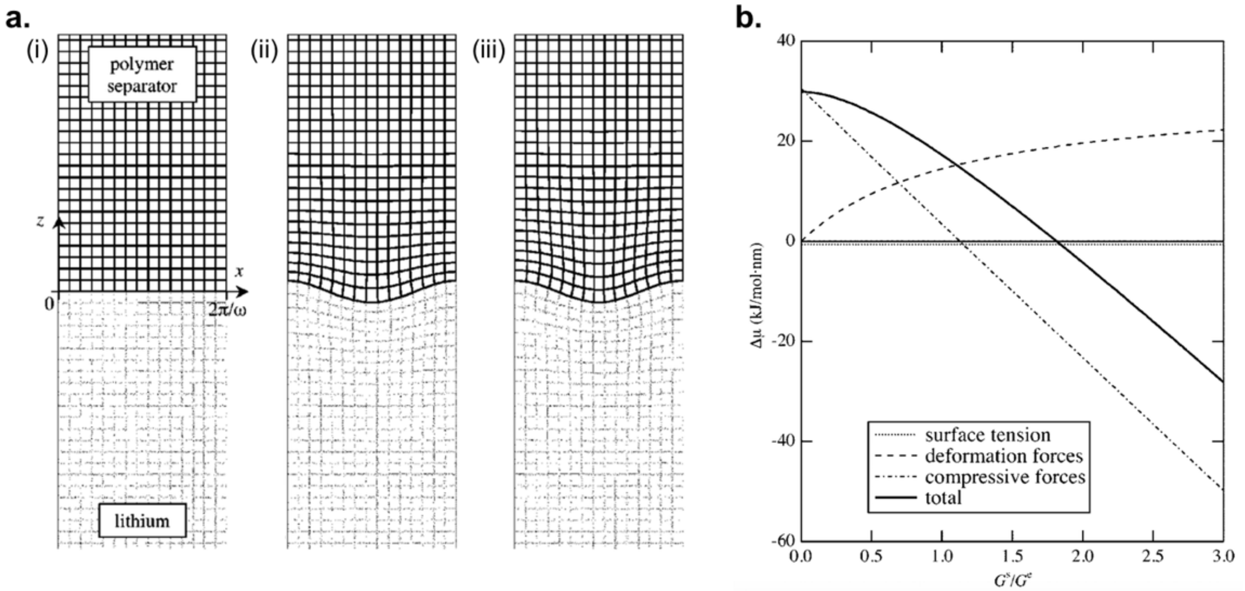

Figure 4.2 a. Displacement distribution at different polymer shear modulus (i) reference position, (ii) compressible polymer $v_s = 0$ and (iii) incompressible polymer $v_s = 0.5$. **b.** Contributions of compressive forces, deformation forces and surface forces as a function of polymer shear modulus,

v_s = 0.33. Reproduced from Ref. 46.

4.3 Current state-of-the-art

4.3.1 Electrolyte additives

Various strategies have been explored to stabilize lithium metal anodes. One strategy is to employ functional additives, such as lithium nitrate[47], lithium polysulfide,[48] and fluoroethylene carbonate.[49,50] Given that these additives exhibit higher reduction potentials than those of electrolytes, lithium preferentially reacts with these additives to form solid electrolyte interphase (SEI). Unfortunately, the resulting SEI is still brittle and can hardly accommodate the volumetric change of lithium during cycling.[51,52] As a result, the additives are continuously consumed during repetitive formation of SEI, resulting in gradually deteriorated electrochemical performance.

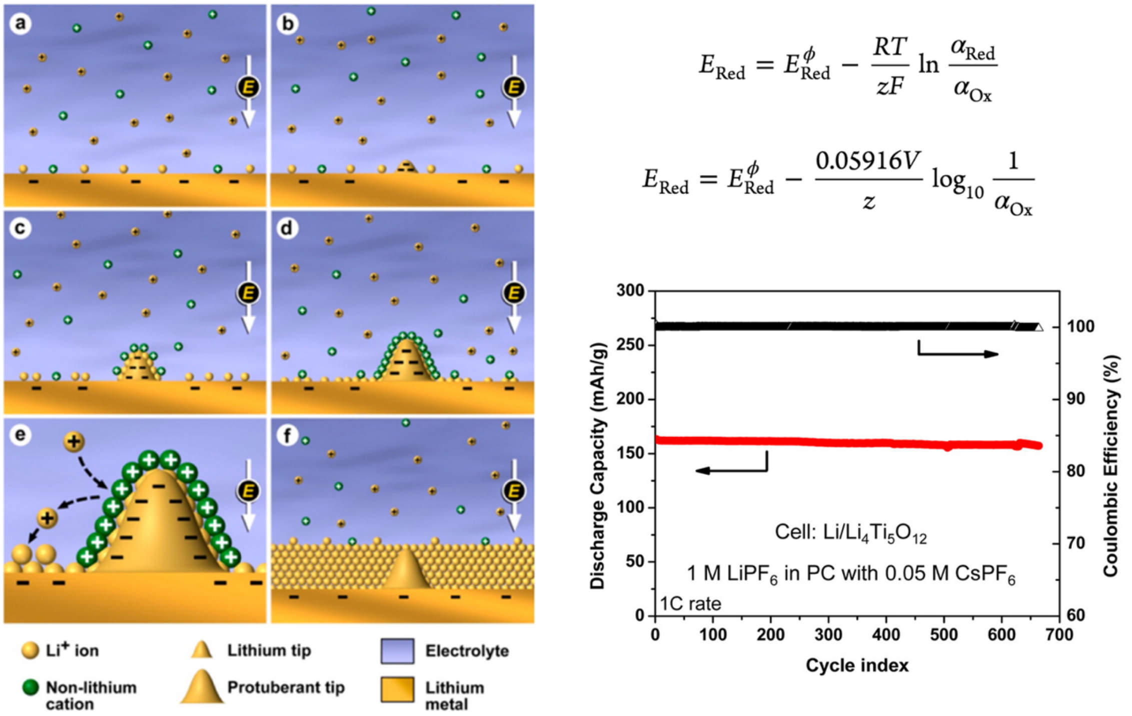
a
b
c
d
e
f
E
Li⁺ ion
Non-lithium cation
Lithium tip
Protuberant tip
Electrolyte
Lithium metal
Discharge Capacity (mAh/g)
Coulombic Efficiency (%)
Cycle index
0
100
200
300
400
500
600
700
50
150
250
60
70
80
90
Cell: Li/Li$_4$Ti$_5$O$_{12}$
1 M LiPF$_6$ in PC with 0.05 M CsPF$_6$
1C rate

$$E_{\mathrm{Red}} = E^{\phi}_{\mathrm{Red}} - \frac{RT}{zF}\ln\frac{\alpha_{\mathrm{Red}}}{\alpha_{\mathrm{Ox}}}$$

$$E_{\mathrm{Red}} = E^{\phi}_{\mathrm{Red}} - \frac{0.05916V}{z}\log_{10}\frac{1}{\alpha_{\mathrm{Ox}}}$$

Figure 4.3 Illustration of the working mechanisms of the self-healing electrostatic shield. Reproduced from Ref. 53.

Ding *et al*. designed an alternative strategy to form a positively charged electrostatic shield around the lithium dendrites without the reduction or deposition of the additives (Figure 4.3)[53]. By manipulating the relative concentration and chemical reactivity of different cations, the reduction potential of Cs^+ can be lower than that of Li^+. When the dendrite tip initiates, Cs^+ can form an electrostatic shield around it, which can repel the coming Li^+ and slow down the growth of lithium dendrites. With such additive, the formation of lithium dendrites is effectively inhibited, but the Coulombic efficiency is still unsatisfactory.

4.3.2 Coating layers

To circumvent the parasitic reactions between lithium and liquid electrolyte components, researchers have exploited various solid materials as electrolytes or coatings for lithium anode. These materials can be categorized into four groups: inorganic, polymeric, hybrid organic/inorganic and carbonaceous materials. Inorganic Li^+ conductors, represented by lithium superionic conductor (LISICON), tend to form point contacts with lithium foil due to their rigidity, resulting in large interfacial resistance.[39,54,55] Although ceramic materials with Li^+ conductivity exceeding 1×10^{-3} S cm^{-1} have been developed, such materials (*e.g.* $Li_{10}GeP_2S_{12}$ and $Li_{1.3}Al_{0.3}Ti_{1.7}(PO_4)_3$) are unstable in the presence of metallic lithium[56,57]. Electrochemically inert lithium phosphorous oxynitride (LiPON)[58] and Al_2O_3[59] (Figure 4.4 a) have been deposited on lithium foil using a sputtering and an atomic layer deposition technique, respectively; however, the area of the coatings is limited (*e.g.*, < 5 cm^2). Polymeric materials, which offer the ease of processing, present insufficient modulus to inhibit dendritic formation.[60-62] Hybrid organic/inorganic layers, which combines the merits of organic and inorganic materials, have been subsequently deposited onto lithium foil and demonstrated successful suppression of dendrite formation at a high current density (*e.g.* 2 mA cm^{-2}).[63] Coatings of carbon nanospheres[64] (Figure

4.4 b) and carbon film[65] have also been transferred onto lithium to facilitate the formation of stable SEI, whereas it is still difficult to implement such coatings during battery fabrication. To date, it is still challenging to stabilize the interface between metallic lithium and liquid electrolyte.

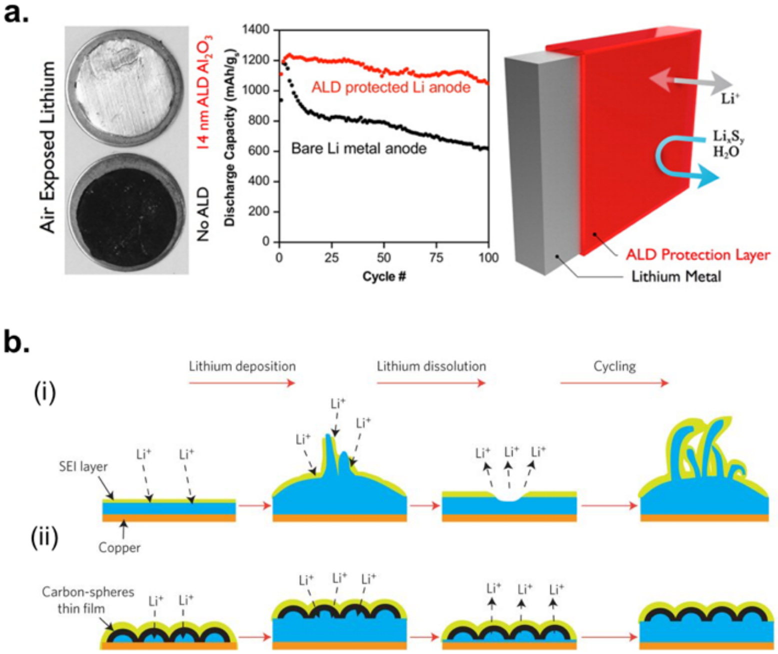
a.
Air Exposed Lithium
14 nm ALD Al2O3
No ALD
Discharge Capacity (mAh/gs)
1400
1200
1000
800
600
400
200
0
ALD protected Li anode
Bare Li metal anode
0
25
50
75
100
Cycle #
Li+
LixSy
H2O
ALD Protection Layer
Lithium Metal
b.
(i)
Lithium deposition
Lithium dissolution
Cycling
Li+
SEI layer
Copper
(ii)
Carbon-spheres thin film

Figure 4.4 a. ALD protected lithium metal anode is resistant to air and lithium polysulfides. **b.** The working mechanism of the carbon-sphere thin film in preventing the growth of lithium dendrites. Reproduced from Ref. 59 and 64.

4.4 Conclusion

The major challenges of lithium metal batteries are the high reactivity of metallic lithium and the formation of lithium dendrites. Although tremendous improvements have been achieved in this field over the last decade, fundamental understandings of the electrochemical process (such as the desolvation process of Li^+ at the interface), the formation of solid electrolyte interphase and the distributions of cation/anion near the electrode surface remain unsolved. The practical application of rechargeable lithium metal battery still needs effort and time for research and developments.

Chapter 5 Working mechanism and intrinsic properties of sulfur species

5.1 Introduction

The electrochemical reduction of sulfur is a multistep process that associated with several phase transitions between solid and solution phases. Understanding the molecular identity and intrinsic properties of the relevant intermediates along the reduction process is essential for the design of high-performance lithium-sulfur batteries. Although researchers have identified several sulfur species using different technologies, their structures and electronic structures are still missing. Here, we systematically investigated the electronic structures of possible sulfur species using density functional theory (DFT) simulations. A wide range of close shell Li_2S_n ($4 \le n \le 8$) molecules with explicit solvent DOL or DME, crown shape *cyclo*-octa sulfur molecules, as well as stable radicals LiS_x are studied in the level of B3LYP functional.

5.2 Geometric structures of sulfur species

5.2.1 S_8

Given that crystalline α-sulfur is only weakly bonded by van der Waals interaction which only imposes minor influence on the band structure of elemental sulfur, isolated crown-S_8 molecule with a symmetry of D_{4h} is used as the model to evaluate the redox property of S^0 species. The calculated band gap (energy difference between HOMO and LUMO) is 3.18 eV, which is close to the experimental value of 2.79 eV[66].

5.2.2 Closed-shell lithium polysulfides

Due to disproportionation reactions of sulfur species, a number of lithium polysulfide intermediates have been found in the electrolyte and researchers have proposed different models regarding their structures. Here, we chose Li_2S_6 as a presentative intermediate molecule and investigated both linear and cyclic structures. Structure optimizations are conducted by Gaussian

09 packages in the level of 6-311g++(d,p) basis sets and B3LYP functional. For both models, except for these explicit solvent molecules, other solvent molecules in the system are considered as implicit with a dielectric constant of 7.34.

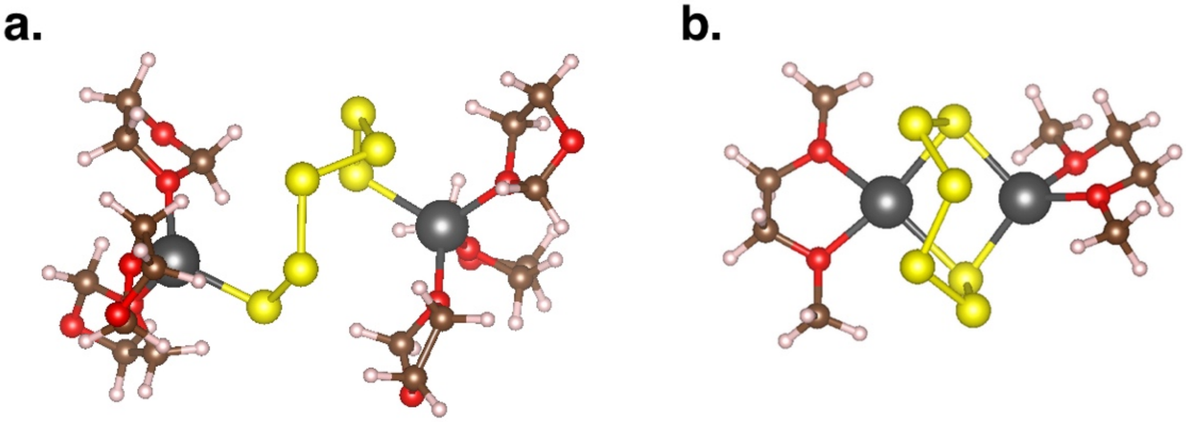

Figure 5.1 Geometric and electronic structures of sulfur species. The geometric structures of **a.** linear Li_2S_6-4DOL, **b.** cyclic Li_2S_6-2DME.

As a solvated molecule, Li_2S_6 may exist in a linear configuration with both lithium cations bonded to the terminal sulfur anions (Figure 5.1 a). Four or six dioxolane (denoted as DOL) molecules are used as explicit solvent molecules to mimic the solvation environment of the lithium cations. This is a very simplified solvation model for Li_2S_6 and DOL/DME molecules. In reality, the solvation shell of Li cations may exchange with environments dynamically. While previous results show that Li cations are 3-4 coordinated in average.[11] Therefore, the numbers shown in Table 5.1 should give a qualitatively correct picture of the redox potential of dissolved Li_2S_6 molecules. It shows that more explicit solvation molecules can elevate both HOMO and LUMO positions, while the addition of implicit solvent expands its band gap from 2.64 eV to 3.17 eV.

The model of cyclic Li_2S_6 is adopted from Fan et al.[67] In this model, lithium cations can also serve as a 4-coordination center with two sulfur atoms and two oxygen atoms from dimethoxymethane (denoted as DME), forming a cyclic Li_2S_6 molecule (Figure 5.1 b). The addition of implicit solvent molecules to this model imposes limited influence on the band structures (Table 5.2). The calculated band gaps of Li_2S_6 based on linear and cyclic structures are 3.17 eV and 3.64 eV, respectively.

Table 5.1 Electronic band structures of linear Li_2S_6 with different solvent models.

	Li_2S_6-4 DOL		Li_2S_6-6 DOL	
	HOMO	LUMO	HOMO	LUMO
With implicit solvent DOL $\epsilon = 7.34$	-4.975 eV	-1.806 eV	-4.522 eV	-1.36 eV
No implicit solvents	-4.800 eV	-2.159 eV		

Table 5.2 Electronic band structures of cyclic Li_2S_6 with different solvent models.

	Li_2S_6-2 DME	
	HOMO	LUMO
With implicit solvent DME $\epsilon = 7.34$	-5.39 eV	-1.75 eV
No implicit solvents	-5.41 eV	-1.86 eV

Similarly, we investigated the geometric structures and electronic band structures of lithium polysulfide molecules with different number of sulfur atoms using the same simulation method. As shown in Table 5.3, they all exhibit linear/ring structures, as well as wide bandgaps. Given that the position of their LUMO is generally above -2 eV, the electro-activation of these sulfur species requires high energy to promote their redox reactions, which is consistent with their sluggish electrochemical behaviors.

Table 5.3 Structures and electronic band edge positions of lithium polysulfide molecules.

Molecule	HOMO/eV	LUMO/eV	Bandgap/eV	structure
Li_2S_4-4 DOL (2)	-4.721	-0.999	3.722	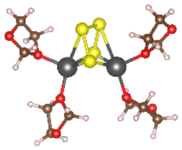
Li_2S_4-6 DOL	-4.325	-0.730	3.595	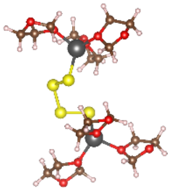
Li_2S_5-4 DOL	-4.797	-1.587	3.21	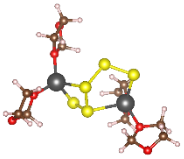
Li_2S_5-6 DOL	-4.540	-1.174	3.366	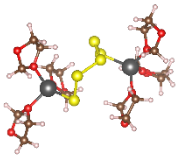
Li_2S_6-4 DOL (2)	-4.951	-2.255	2.696	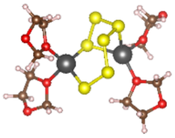
Li_2S_6-2 DME	-5.034	-1.373	3.661	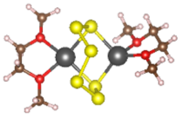
Li_2S_6-6 DOL	-4.597	-1.384	3.213	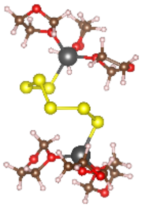
Li_2S_7-4 DOL	-5.077	-2.148	2.929	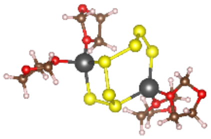

5.2.3 Sulfur radicals

Although the structures of lithium polysulfides are still under debate, the existence of sulfur radicals has been demonstrated with electron paramagnetic resonance (EPR) spectroscopy[12,14] (Figure 5.2). It has also been proposed that these sulfur radicals are the reactive intermediates in sulfur cathodes and there is an equilibrium between Li_2S_n and sulfur radicals (REF). Therefore, we studied three different structures of sulfur radicals (*i.e.*, LiS_3, LiS_4, and LiS_5) using both micro-salvations and density functional theory (DFT) methods. The bare radicals can represent the limit of weak solvation in a nonpolar solvent, while the radicals with explicit DME or DOL can mimic the limit of strong solvation.

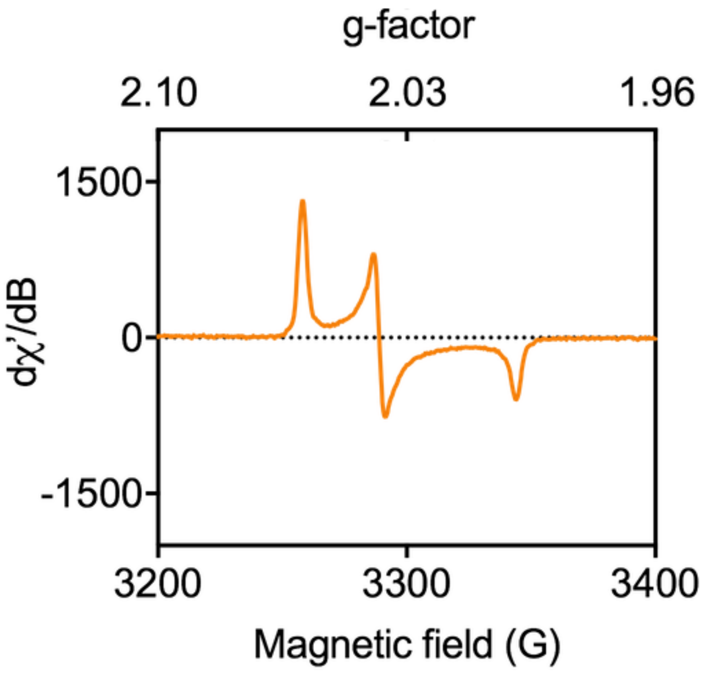

Figure 5.2 EPR spectrum of 20 mM Li_2S_6 solution at 5 K.

Optimized LiS_3 and LiS_4 radicals present cyclic structures (Table 5.4), which are similar with previously proposed radical structures.[15] Such ring structures are maintained even when the Li cations are coordinated with DOL molecules. LiS_5 radicals show slightly different geometries, where lithium cation forms bonds with four S atoms of the sulfur chain. Meanwhile, LiS_5 can present a similar ring structure when it is explicitly solvated by 2 DOL molecules. The band gaps of these radicals much smaller compared to that of molecular lithium polysulfides, indicating that sulfur radicals are the more reactive intermediate species in the system.

Table 5.5 compares the g-factors obtained from calculations and EPR experiments, indicating that both LiS_4 and LiS_3 radicals may exist in the solution. We further optimized the structure of sulfur radicals and calculated their electronic band structures. Vibration analysis is carried out by G09 package to calculate the thermal corrections and zero-point energy (ZPE). In order to avoid the effect of BSSE on the calculation of complexation energy between LiS_n radicals and DOL solvents, additional calculations with VASP, which exploits plane waves as basis sets are conducted (the cutoff for plane waves are 600 eV). The free energy is calculated by summation of electronic energies from VASP and thermal corrections from G09 package.

Table 5.4 Structures and electronic band edge positions of LiS_5, LiS_4, LiS_3 radicals.

Formula	HOMO/eV	LUMO/eV	Bandgap/eV	Structure
LiS_3	-5.954	-3.872	2.082	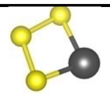
LiS_3 (aug-cc-pvqz)	-5.885	-3.741	2.144	Same as above
LiS_3-1DOL	-5.465	-3.392	2.073	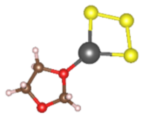
LiS_3-1DOL(aug-cc-pvqz)	-5.408	-3.273	2.135	Same as above
LiS_3-2DOL	-5.234	-3.163	2.071	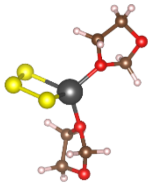
LiS_4	-5.785	-3.975	1.81	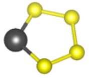
LiS_4 (aug-cc-pvqz)	-5.693	-3.835	1.858	Same as above
LiS_4-1DOL	-5.316	-3.515	1.801	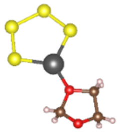
LiS_4-1DOL(aug-cc-pvqz)	-5.237	-3.388	1.849	Same as above
LiS_4-2DOL	-5.173	-3.388	1.785	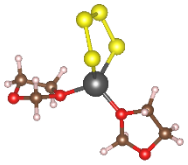
LiS_5	-6.356	-4.518	1.838	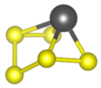
LiS_4 (aug-cc-pvqz)	-6.240	-4.384	1.856	Same as above
LiS_5-1DOL	-5.903	-4.061	1.842	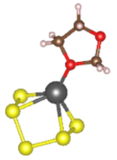
LiS_5-2DOL	-5.522	-4.025	1.497	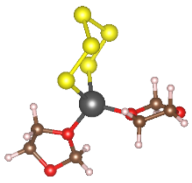

Table 5.5 Comparison of g-factors obtained from DFT simulation and EPR measurement.

	g factor			Error		
	g_x	g_y	g_z	g_{xx}	g_{yy}	g_{zz}
Experimental result	2.00421	2.03770	2.05694	-	-	-
LiS$_3$	2.00165	2.04085	2.05560	-0.00256	0.00315	-0.00134
LiS$_4$	2.00144	2.03626	2.06156	-0.00277	-0.00144	0.00462
LiS$_5$	2.00866	2.02166	2.06792	0.00445	-0.01604	0.01098
LiS$_3$[1]	2.00163	2.04170	2.05977	-0.00258	0.00400	0.00283
LiS$_4$[1]	2.00142	2.03723	2.06341	-0.00279	-0.00047	0.00647
LiS$_5$[1]	2.00962	2.01664	2.06094	0.00541	-0.02106	0.00400
LiS$_3$[2]	2.00166	2.03683	2.05035	-0.00255	-0.00087	-0.00659
LiS$_4$[2]	2.00143	2.03354	2.05552	-0.00278	-0.00416	-0.00142
LiS$_5$[2]	2.00901	2.01588	2.05235	0.00480	-0.02182	-0.00459
LiS$_3$-DOL[3]	2.00164	2.04233	2.05726	-0.00257	0.00463	0.00032
LiS$_4$-DOL[3]	2.00137	2.03575	2.06389	-0.00284	-0.00195	0.00695
LiS$_5$-DOL[3]	2.00994	2.02038	2.07627	0.00573	-0.01732	0.01933
LiS$_3$-DME[4]	2.00161	2.04278	2.05808	-0.00260	0.00508	0.00114
LiS$_4$-DME[4]	1.99953	2.03394	2.09265	-0.00468	-0.00376	0.03571
LiS$_5$-DME[4]	2.01052	2.01347	2.05846	0.00631	-0.02423	0.00152

[1] diethyl ether is used as the implicit solvent.

[2] Aug-CC-pVQZ(5D,7F) is used as basis sets rather than 6-311++(d,p).

[3] One DOL molecule is used as explicit a solvation molecule.

[4] One DME molecule is used as explicit a solvation molecule.

To study the stable solvation structure for sulfur radicals, we studied the complexation energy LiS_x-nDOL. The complexation free energy is defined by:

$$G(\text{complexation}) = G(\text{LiS}_\text{x}\text{-nDOL}) - G(\text{LiS}_\text{x}\text{-(n-1)DOL}) - G(\text{DOL})$$

The negative complexation free energy means the complex is more stable. Furthermore, vibration analysis is performed with G09 package to get the free energy of molecules and calculate the thermal corrections and zero-point energy (ZPE). Meanwhile, the electronic energies are calculated by additional calculations with VASP package, where plane waves are with fixed cutoff energy (ENCUT=600 eV) are used. This method can avoid the effect of BSSE (Basis Set Superposition Error) on the calculated free energy. In the end, the free energy is calculated by summation of electronic energies from VASP and thermal corrections from G09.

The results listed in Table 5.6 show that radicals prefer to form solvated structures with only one DOL molecule, regardless of the chain length of sulfur. It should be noted that we did not consider the effect of entropies of the solution. Nevertheless, we can anticipate that LiS_x-2DOL is less favorable even the entropy is taken into account.

Table 5.6 Complexation free energy of solvated sulfur radicals.

Radicals	First DOL (kJ/mol)	Second DOL (kJ/mol)
LiS_3	-27.3	4.95
LIS_4	-28.7	17.8
LiS_5	-24.9	7.34

5.2.4 Li_2S_2

Li_2S_2 is widely accepted as a transient crystalline product at the end of the charge process or at the beginning of the discharge process.[68] In this work, we adopted the structure determined by global optimization method.[69] As shown in Figure 5.3, the unit cell of Li_2S_2 is composed of a tetragonal cell with a symmetry of $P4_2/mnm$. This structure is formed by LiS_4 tetrahedrons sharing edges and vertexes, in which sulfur atoms form 4 S-Li ionic bonds and one S-S bond (2.117 Å) with neighboring LiS_4 tetrahedrons. The calculated band gap is 2.29 eV, which is slightly larger than previous DFT predicted value of 1.8 eV[69].

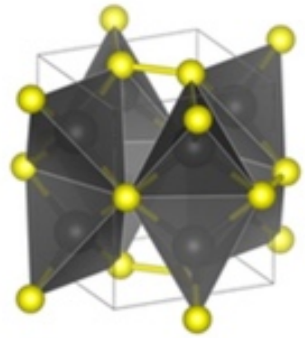

Figure 5.3 Geometric and electronic structures of Li_2S_2.

5.3 Electronic structures of sulfur species

To get a better understanding of the electronic structures of related sulfur species, we further calculated their electronic density of states (DOS) using DFT in the level of meta-GGA (SCAN)[70]. DOS is an electron density distribution that describes the number of electron states at each energy level. As shown in Figure 5.4, molecular species (*i.e.*, S_8 and Li_2S_2) exhibit symmetrical DOS, while radicals (*i.e.*, LiS_4 and LiS_3) present unsymmetrical DOS with unpaired electrons, which is consistent with the results of EPR spectroscopy.

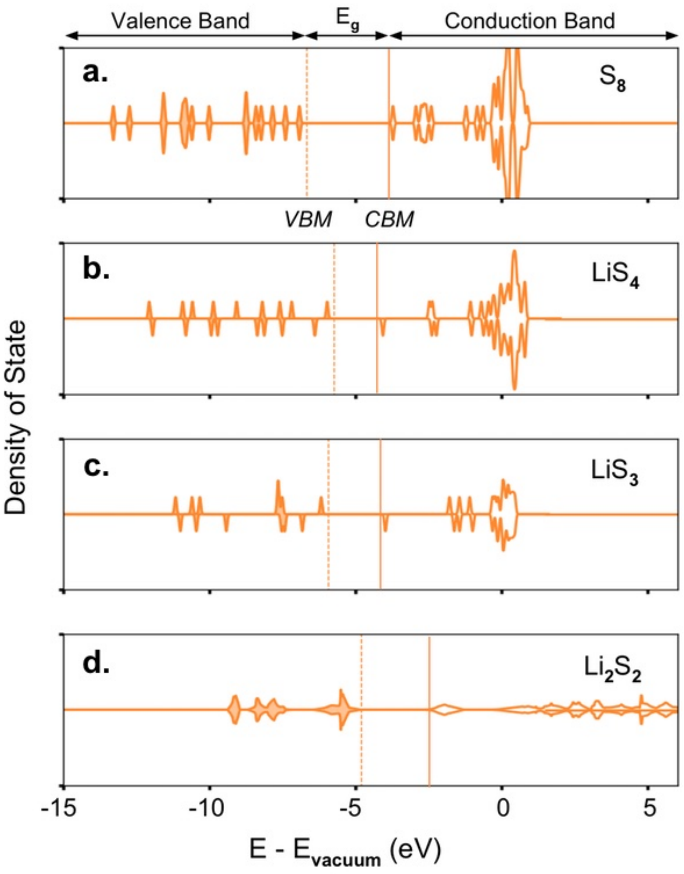

Figure 5.4 Electronic density of states (DOS) of **a.** S_8, **b.** LiS_4 radical, **c.** LiS_3 radical and **d.** Li_2S_2. Shadowed area represents filled valence band, while unfilled area indicates empty conduction band. The vertical dashed lines and solid lines show the positions of VBM and CBM, respectively.

Additionally, the band edges (HOMO and LUMO) of all sulfur species are aligned with respect to vacuum energy to illustrate the electron transfer process during cycling (Figure 5.5). During discharge, electrons from the external circuit are inserted into the conduction band of S_8, generating lithium polysulfides Li_2S_n. These molecules can be spontaneously converted into sulfur radicals, which are electrochemically more reactive. During continuous discharge, electrons will be transferred to the conduction bands of these radicals and drive the equilibrium between Li_2S_n and LiS_n radicals to the radical side. At the end of discharge, all the sulfur species will be converted Li_2S_2/Li_2S. During the reversed charge process, the electrons are extracted from the valence band of sulfur species and transported to the external circuit. At the end of charge process, all the sulfur species are converted back to S_8.

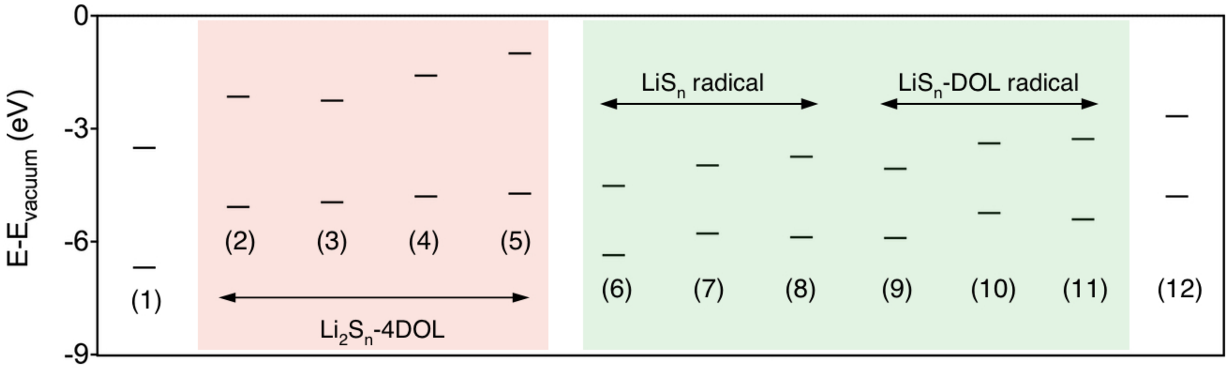

Figure 5.5 Electronic band edges of sulfur species aligned with respect to vacuum energy. The sulfur species are (1) S_8, (2) Li_2S_7-DOL, (3) Li_2S_6-DOL, (4) Li_2S_5-DOL, (5) Li_2S_4-DOL, (6) LiS_5 radical, (7) LiS_4 radical, (8) LiS_3 radical, (9) LiS_5-DOL radical, (10) LiS_4-DOL radical, (11) LiS_3-DOL radical, (11) Li_2S_2.

5.4 Conclusion

The sluggish electrochemical response of sulfur species is rooted from their wide electronic band structures, which require high activation energy to promote their electrochemical conversions. Such intrinsic limitations can't be circumvented unless their reaction pathways are altered. In chapter 8, we will introduce the concept of redox mediator, which can effectively enable the fast electron transfer to sulfur species.

Chapter 6 Regenerative Polysulfide-Scavenging Layers

6.1 Introduction

Extensive efforts have been made to address polysulfide shuttling, which causes the capacity decay and short cycling lifetime of lithium-sulfur batteries. One focus is to infiltrate sulfur into conductive scaffolds.[16,71-75] Polysulfides, which are generated continuously during the discharge process, may still diffuse throughout the cells. To restrain the outward diffusion of lithium polysulfides, various materials have been coated onto the separators. For example, polymer layers,[76-78] represented by Nafion with sulfonated moieties ($-SO_3^-$), may block the diffusion of polysulfides anions through electrostatic repulsion. High loading of high-cost Nafion, however, is required to achieve sufficient blocking effect (*e.g.*, 0.7 mg cm^{-2} loading of Nafion for cathodes with 0.53 mg cm^{-2} loading of sulfur).[77] Metal-oxide layers, represented by V_2O_5 layers, allow effective transport of Li^+ ions while blocking the diffusion of polysulfides.[79] Such inorganic coatings are generally achieved by the sol-gel process, and are often brittle and defective. In addition, extensive research on carbon-coated separators has been conducted, utilizing CNTs,[35,80-83] graphene,[84,85] carbon black,[86-88] carbon fibers,[89] porous carbons,[90-93] as well as composites of carbons and non-reactive inorganic moieties (*e.g.*, Al_2O_3[94], TiO_2[95] and SiO_2[96]) as adsorbents. Through physisorption of polysulfides, such carbon-coated separators help mitigate the shuttling effect; however, the effectiveness and enhancement is mostly limited to cathodes with low sulfur loadings (< 2 mg cm^{-2}). Therefore, it remains challenging to develop effective polysulfide-blocking layers for high loading cathodes (>6 mg cm^{-2}) to achieve high specific energy (> 350 Wh kg^{-1}) and prolonged cycling life (>100 cycles).[26]

In this chapter, we designed an effective polysulfide-blocking strategy based on regenerative polysulfide-scavenging layers (RSL), which can dynamically block the diffusion of polysulfides and regenerate themselves during cycling. As illustrated in Figure 1, the RSL are made from flexible and conductive membranes of carbon nanotubes (CNTs), in which the center layers are embedded with nanowires or nanocrystals of metal oxides. The outward diffused polysulfides are adsorbed by or reacted with the RSL, forming [Polysulfides-RSL] complexes and being immobilized within the RSL. Subsequent charge process stripes away these polysulfides and regenerates the RSL. This combination of a large amount of polysulfides scavenged and the regenerative capability affords highly effective and dynamic scavenging of polysulfides, leading to dramatically reduced lithium corrosion and prolonged cycling life, especially for electrodes with high sulfur loadings. Furthermore, the RSL are electronically conductive and mechanically robust, thus further enhance the performance of the cells. The scavenging effects, which are originated from the physisorption and chemical reaction with polysulfides, have been thoroughly investigated and correlated with the electrochemical performance of the cells.

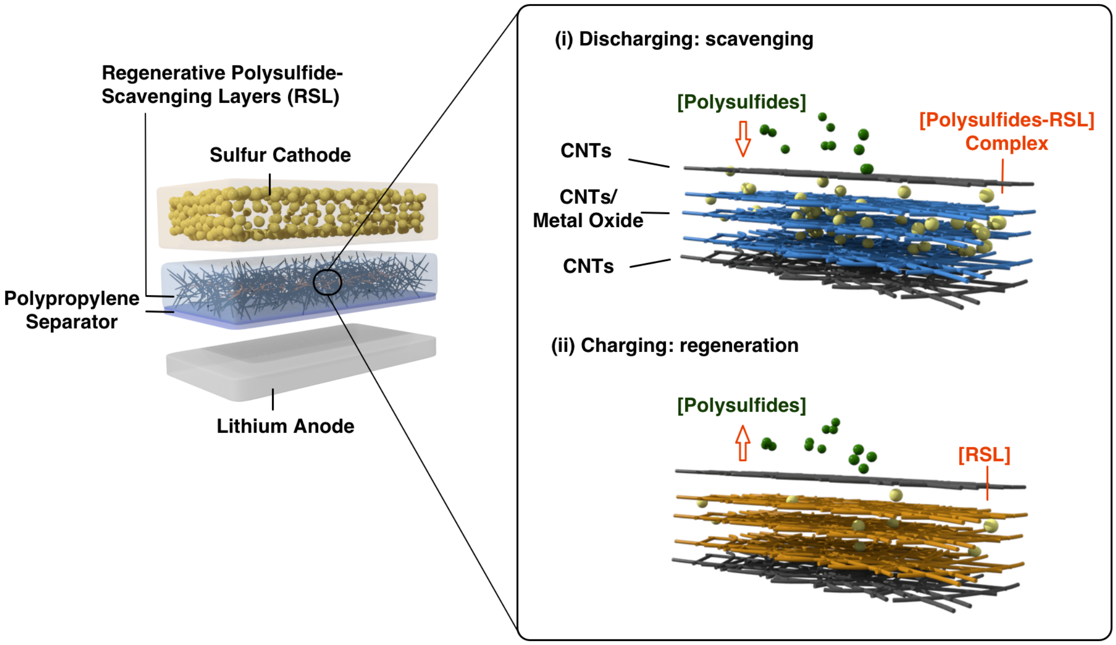
Regenerative Polysulfide-Scavenging Layers (RSL)
Sulfur Cathode
Polypropylene Separator
Lithium Anode
(i) Discharging: scavenging
[Polysulfides]
[Polysulfides-RSL] Complex
CNTs
CNTs/ Metal Oxide
CNTs
(ii) Charging: regeneration
[Polysulfides]
[RSL]

Figure 6.1 Schematic presentation of a Li-S cell with a regenerative polysulfide-scavenging layers (RSL). The RSL is made from a CNTs membrane of which the center is embedded with

interpenetrating nanowires or nanocrystals of metal oxides. (i) During discharge, as-generated polysulfides are adsorbed by or reacted with the RSL, immobilized onto the RSL denoted as [Polysulfides-RSL] complexes. (ii) Subsequent charge process strips away the immobilized species and regenerates the RSL, enabling dynamic blocking of the polysulfides.

6.2 Methods

6.2.1 Synthesis of CNTs/oxides composites.

CNTs/V_2O_5 composite. CNTs/V_2O_5 composites were synthesized with activated CNTs according to the previously reported procedure.[97] Briefly, 0.6 g of ammonium metavanadate (Sigma-Aldrich) and 1 g of P123 ($EO_{20}PO_{70}EO_{20}$) (Sigma-Aldrich) were dispersed in 60 mL deionized water with 3 mL 2 M HCl. 20 mg activated CNTs was added to the mixture and sonicated for 30 min. The mixture was stirred at room temperature for 12 h and then transferred to an autoclave and heated at 120 ˚C for 24 h. The resulted composites were rinsed with DI water and ethanol for 3 times and dried at 80 ˚C overnight in vacuum. Other CNTs composites containing different metal oxides were synthesized using similar hydrothermal methods (see Supplementary Information for details).

CNTs/Fe_2O_3 composite. 1.25 g $FeSO_4 \cdot 7H_2O$, 5 mL of polyethylene glycol 20,000 solution (50 g L^{-1}) and 20 mg activated CNTs were dispersed in 42.5 mL DI water by sonication. 5 mL of diluted ammonia (2.5 wt%) and 0.135 mL H_2O_2 (28-30 wt%) were added into the above mixture under stirring. The mixture was then stirred for 1h at room temperature and underwent hydrothermal reaction at 160 ˚C for 8 h. After cooling to room temperature, as-formed composites were filtered, washed with distilled water, and dried at 60 ˚C overnight in vacuum.

CNTs/CuO composite. 0.94 g copper nitrate (Sigma-Aldrich), 1 g of P123 and 20 mg active CNTs were dispersed in 40 mL DI water by sonication. Then, 10 mL of ammonium hydroxide solution (27-30 wt%) was added. The mixture was then stirred for 1h at room temperature, and then underwent hydrothermal reaction at 110 ˚C for 4 h. The as-formed product was rinsed with deionized water and ethanol for 3 times and dried at 80 ˚C overnight in vacuum. The product was further calcinated in nitrogen at 300 ˚C for 2 h.

CNTs/MnO_2 composite. 0.72 g $KMnO_4$ and 20 mg active CNTs were dispersed in 60 mL of deionized water by sonication. The mixture underwent hydrothermal reaction at 100 ˚C for 24 h. The products were rinsed with deionized water for 3 times and then dried at 80 ˚C overnight in vacuum.

CNTs/MoO_3 composite. 1 g ammonium heptamolybdate tetrahydrate, 1g of P123 and 40 mg active CNTs were dispersed in 33 mL of deionized water by sonication. Then, 6 mL HNO_3 was added and allowed to react at 180 ˚C for 24 h. The products were rinsed with deionized water for 3 times and then dried at 80 ˚C overnight in vacuum.

CNTs/WO_3 composite. 0.5 g of sodium tungstate, 0.25 g of ammonium sulfate (Sigma-Aldrich) and 20 mg activated CNTs were dispersed in 10 mL of deionized water by sonication. The pH of the solution was then adjusted to 1 by adding 3 M H_2SO_4 aqueous solution. The mixture underwent hydrothermal reaction at 100 ˚C for 12 h. The products were rinsed with deionized water for 3 times and then dried at 80 ˚C overnight in vacuum.

6.2.2 Fabrication of RSL. The RSL were prepared using a vacuum-filtration method. CNTs and CNTs/metal oxides composites were dispersed in ethanol by sonication and formed 0.1 mg mL^{-1} and 1 mg mL^{-1} suspensions, separately. Subsequently, 20 mL CNT suspension, 6 mL suspension of CNTs/metal oxides composites and 20 mL CNT suspension were vacuum filtered through a polypropylene membrane (Celgard 2500, diameter: 47 mm) and form a flexible triple-layer membrane. The membranes were dried at 70 ˚C overnight and then punched into a round shape with a diameter of 18 mm. The weight of the RSL on each separator is around 0.4-0.6 mg cm^{-2}

(Supplementary Table 1). For CNTs RSL, 100 mL CNT suspension was filtrated.

6.2.3 Preparation of sulfur cathodes and Li_2S_6 solution. Sulfur cathodes were prepared using a slurry casting method. For electrodes with low sulfur loading (1~2 mg cm^{-2}), sulfur, carbon black and polyvinylidene fluoride (PVDF) were mixed with weight ratio of 5:4:1 to form a homogenous slurry with N-methyl-2-pyrrolidone, then casted onto carbon-coated aluminum foil with a doctor blade. For electrodes with higher sulfur loading (up to 6 mg cm^{-2}), carbon/sulfur composites, carbon nanofiber, carbon black and PVDF were mixed with weight ratio of 88:4:1:7 to form a slurry. Porous carbon particles were fabricated using Kejent black[98] and the carbon/sulfur composites were prepared using liquid infiltration method at 159 ˚C with a weight ratio of 1:4. The electrodes were dried at 70 ˚C in vacuum for 4 h and then cut into pieces with a diameter of 16 mm. 0.5 M Li_2S_6 solution was prepared by mixing stoichiometric amounts of elemental sulfur (Sigma Aldrich) and Li_2S (Alfa Aesar) in DOL:DME (volume ratio 1:1). A homogenous dark-red solution of Li_2S_6 was obtained after stirring for 24 h at 130 ˚C.

6.2.4 Material characterization methods. XRD measurements were performed on Rigaku MiniFlex instrument using the copper Kα radiation (λ = 1.54 Å). TGA was performed on a TA Instrument SDT Q600 employing a heating rate of 5 ˚C min^{-1} from 40 ˚C to 600 ˚C under airflow. SEM studies were conducted on a JEOL JSM-6700 FE-SEM and TEM studies were carried out on a FEI T12 operating at 120 kV. For XPS studies, the samples were sealed in a transporter in the glove box before being quickly transferred to the high-vacuum chamber of XPS (AXIS Ultra DLD) for analysis. All the spectra were fitted to Gaussian-Lorentzian functions and a Shirley-type background using CasaXPS software. The binding energy values were all calibrated using C 1s peak at 286.0 eV.

6.2.5 Electrochemical characterization methods. To evaluate the electrochemical performance, 2032-type coin cells (MTI Corporation) were assembled using lithium metal as the anodes. RSL were placed between the polypropylene separator and sulfur cathode. 0.5 M LiTFSI and 2 wt-% $LiNO_3$ in DOL/DME was used as the electrolyte. CV measurements were performed on a Bio-Logic VMP3 electrochemical workstation. Galvanostatic charge-discharge measurements were carried out using Land CT2000 battery tester in a voltage range of 1.7-2.8 V for all rates. Specific capacities were calculated with respect to the mass of sulfur. EIS tests were carried out on a Solartron 1860/1287 Electrochemical Interface.

6.3 Material characterizations.

Here, V_2O_5 nanowires were selected as a model oxide, which has been extensively explored for electrochemical energy storage with high capacity (294 mAh g^{-1} with 2 Li^+ insertion/extraction per unit), fast Li^+ intercalation kinetics, and long cycling life (> 500 cycles).[99] Besides, it exhibits a redox window from 1.8 to 4.0 V (*vs.* Li^+/Li), matching well with the redox window of sulfur (1.7 to 2.8 V *vs.* Li^+/Li). We have recently synthesized the composites of V_2O_5 nanowires intertwined with CNTs using hydrothermal reaction.[97,100] Based on such composites, CNTs/V_2O_5 RSL were fabricated by sequentially depositing thin layers of CNTs, CNTs/V_2O_5 composites, and CNTs onto commercial polypropylene separators.

Figure 6.2 a-b present the scanning electron microscopy (SEM) and transmission electron microscopy (TEM) images of the CNTs/V_2O_5 composites, respectively, demonstrating a continuous fibrous structure made from interpenetrative V_2O_5 nanowires and CNTs. The nanowires are porous (see inset) with diameters of ~30 nm. The high-resolution TEM (HRTEM) image and selected area Fast Fourier Transformation (FFT) of the V_2O_5 nanowires shows a layered crystalline structure (Figure 6.2 c). The HRTEM image displays a *d*-spacing of 0.211 nm, which is consistent with the (020) lattice plane of V_2O_5.

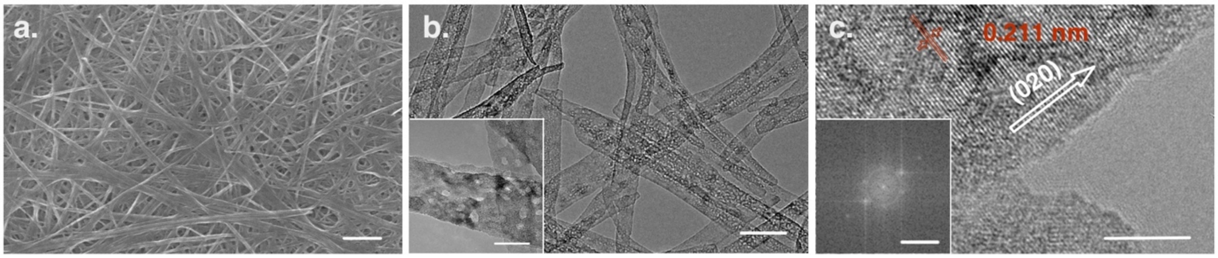

Figure 6.2 a. SEM image of a CNTs/V_2O_5 composite with a fibrous structure made from interpenetrative V_2O_5 nanowires and CNTs. **b.** TEM images of the CNTs/V_2O_5 composites, showing a continuous and porous structure with an average nanowire diameter of ~30 nm. **c.** High-resolution TEM image and its corresponding selected area FFT image (inset) of the CNTs/V_2O_5 composites. Scale bars are a. 500 nm; b. 50 nm, 10 nm (inset); **c.** 5 nm, 1 nm (inset).

X-ray diffraction (XRD) analysis (Figure 6.3 a) reveals the characteristic peaks at 9.2, 13.2, 26.4, 29.1 and 41.8°, corresponding to the (001), (002), (111), (200) and (020) planes of V_2O_5 with a layered structure, respectively.[101,102] According to the result of thermogravimetric analysis (TGA), the weight percent of CNTs in the composites is 9.8 % (Figure 6.3 b).

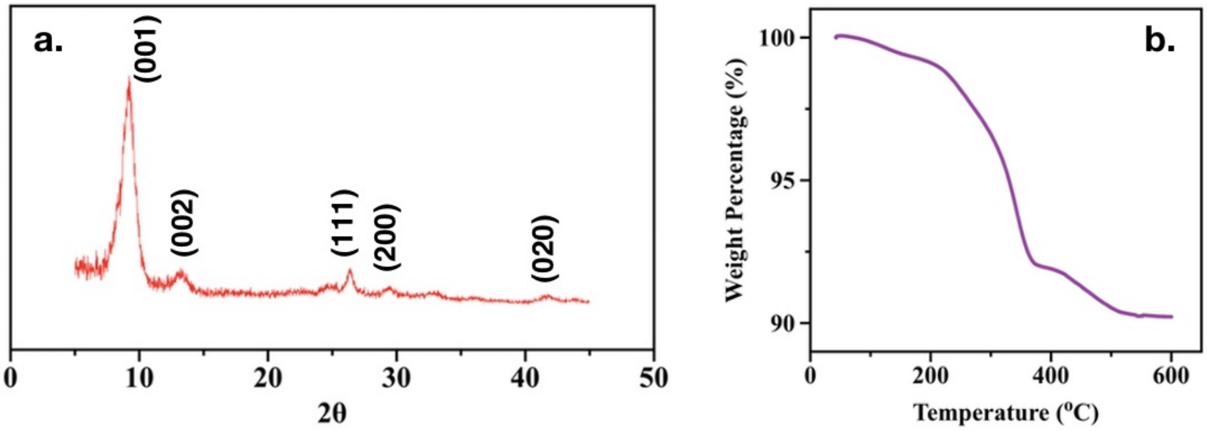

Figure 6.3 a. X-ray diffraction profile and **b.** TGA plot of the CNTs/V_2O_5 composites.

The triple layer structure can be formed through vacuum filtration. Figure 6.4 shows a cross-sectional image of RSL with ~15 μm in thickness, which contains porous CNTs layers sandwiched with a V_2O_5-rich layer in the center. Such RSL are also flexible with good mechanical strength (Figure 6.5).

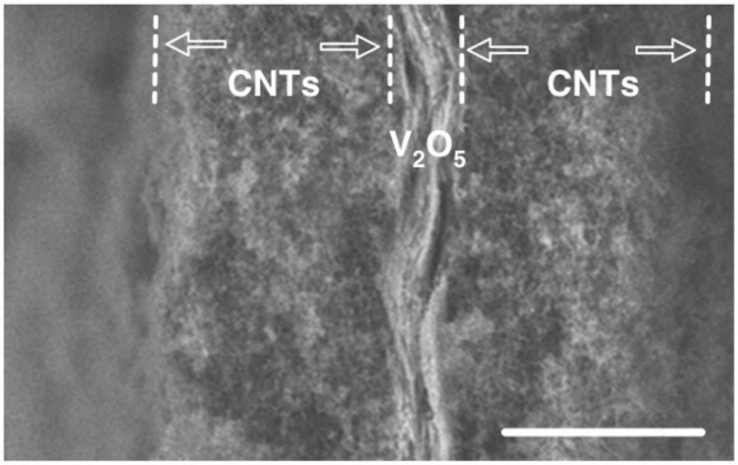

Figure 6.4 Cross-section SEM image of a CNTs/V_2O_5 RSL made from two CNTs layers and a sandwiched CNTs/V_2O_5 layer. Scale bar is 5 μm.

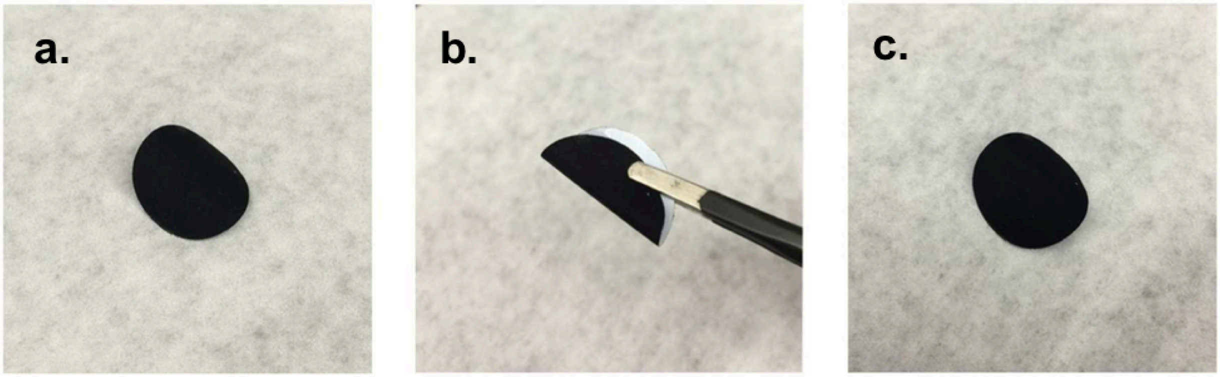

Figure 6.5 Digital photographs of CNT/V_2O_5 RSL **a.** as prepared, **b.** folded and **c.** recovered state.

6.4 Electrochemical behaviors

The redox behavior of the sulfur cathodes with Celgard polypropylene (PP) separator or the CNTs/V_2O_5 RSL was first examined with cyclic voltammetry (CV) at a scanning rate of 0.2 mV s^{-1} (Figure 6.6 a). To deconvolute the attribution of the CNTs and the V_2O_5 moieties, CNTs RSL were fabricated with CNTs *via* a similar method and integrated with the sulfur cathode. All three cathodes present two cathodic peaks corresponding to the reduction of elemental sulfur and high-order lithium polysulfides, and an anodic peak corresponding to the oxidation of sulfur species.[95] The electrode without RSL shows sluggish electrochemical kinetic, which is resulted from the low electronic and ionic conductivity of the sulfur species.[16,80,103] By incorporating the CNTs/V_2O_5 RSL or the CNTs RSL, the cathode exhibits well-defined redox peaks with less polarization. Figure 6.6 b presents the electrochemical impedance spectroscopy (EIS) of the electrodes, showing a charge transfer resistance of 160, 70 or 55 ohms with Celgard PP separator, CNTs/V_2O_5 RSL or CNTs RSL, respectively. The improved conductivity will enhance the rate performance and capacity of sulfur.

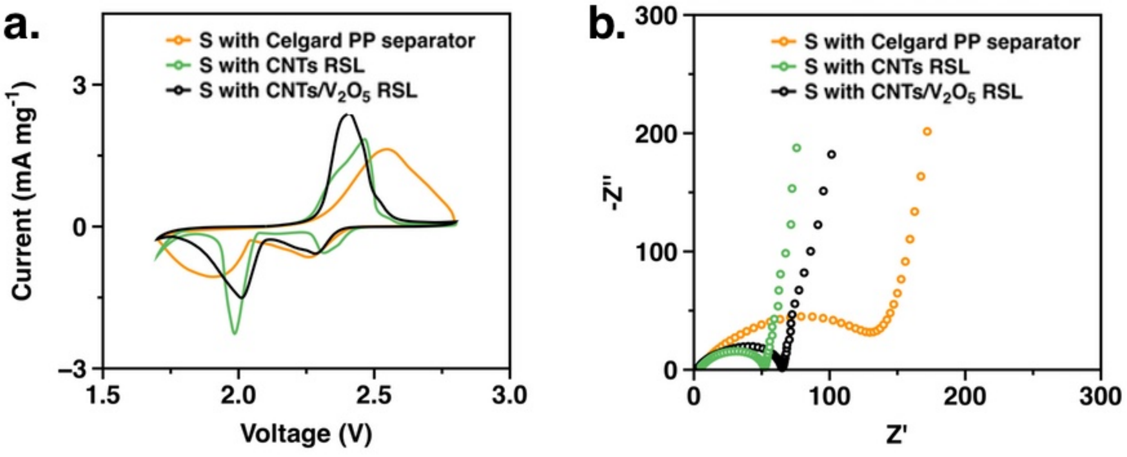

Figure 6.6 a. Cyclic voltammetry obtained at a scanning rate of 0.2 mV s^{-1}. **b.** Nyquist plots showing a reduced charge-transfer resistance with the RSL.

As shown in Figure 6.7, the sulfur electrode with Celgard PP separator exhibits an initial capacity of 663 mAh g^{-1} at 0.3 C rate (1 C = 1675 mA g^{-1}) and reversible capacities of 521, 396, 352, and 272 mAh g^{-1} at 0.5, 1, 2 and 4 C rates, respectively. In addition, the sulfur electrode with CNTs RSL presents an initial capacity of 1396 mAh g^{-1} at 0.3 C rate and reversible capacities of 901, 768, 694 and 614 mAh g^{-1} at 0.5, 1, 2 and 4 C rates, respectively. In contrast, the sulfur electrode with the CNTs/V_2O_5 RSL delivers a much higher initial capacity of 1513 mAh g^{-1} at 0.3 C rate and reversible capacities of 1170, 1063, 954 and 858 mAh g^{-1} at 0.5, 1, 2 and 4 C rates, respectively. As-presented electrochemical performance clearly suggests that the incorporation of CNTs/V_2O_5 RSL leads to significantly improved rate performance and the utilization of sulfur.

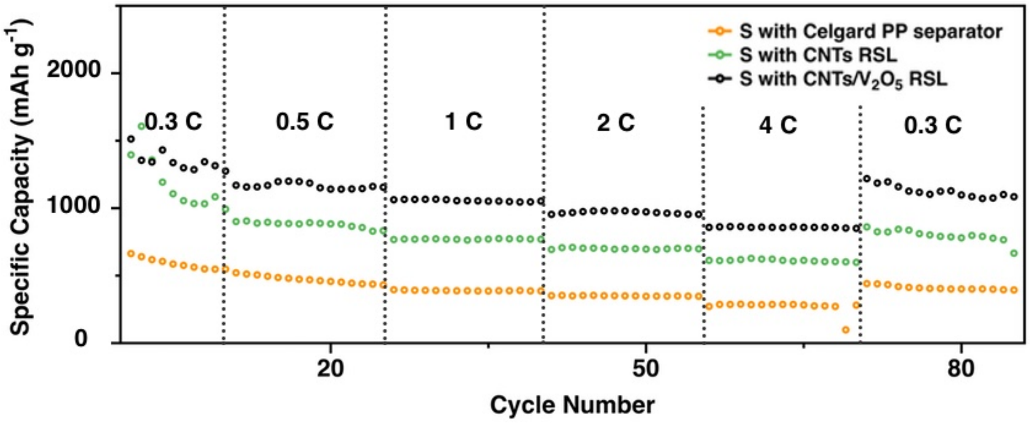

Figure 6.7 Rate performance at 0.3 C, 0.5 C, 1 C, 2 C, 4 C and 0.3 C rate.

Figure 6.8 illustrates the cycling stability of sulfur electrodes with moderate sulfur loading at 1 C rate. With the conventional separator, a low initial capacity of 315 mAh g^{-1} is observed, which decreases to 124 mAh g^{-1} after 250 cycles, while the cell with the CNTs/V_2O_5 RSL delivers a much higher initial capacity of 1068 mAh g^{-1} and a reversible capacity of 939 mAh g^{-1} after 250 cycles. As shown in Figure 6.8, the cell with the CNTs RSL exhibits a reversible capacity of 498 mAh g^{-1} after 250 cycles, which is significantly lower than that with the CNTs/V_2O_5 RSL. Furthermore, the one with the CNTs/V_2O_5 RSL retains near 100% efficiency after 200 cycles, while the one with the CNTs RSL suffers from severe shuttling effect with dramatically reduced Coulombic efficiency. This comparison indicates that the enhancement in cycling stability is mainly contributed by the V_2O_5 moieties.

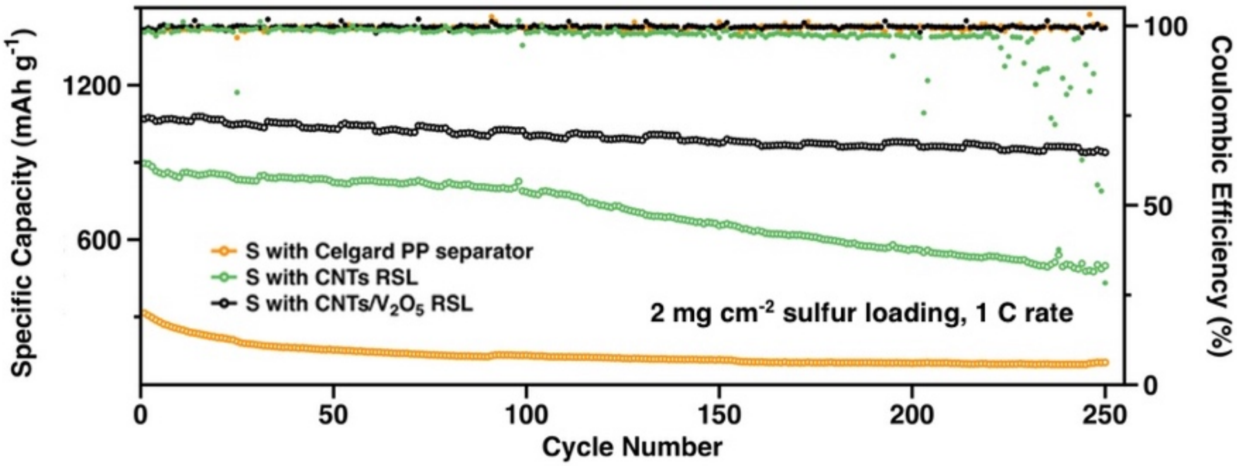

Figure 6.8 Galvanostatic cycling performance at 1 C rate. The empty bullets (○) represent the discharge capacity and circle bullets (•) represent the Coulombic efficiency.

In addition, Figures 6.9 a-b compare the electrochemical performance of the Li-S cells with a sulfur loading of 6 mg cm^{-2} at 0.1 C rate and 0.2 C rate, respectively. At 0.1 C rate, the cells with CNTs RSL and Celgard PP separator deliver similar capacity and cycling stability, while the cell with the CNTs/V_2O_5 RSL exhibits significantly higher initial capacity at 0.05 C rate (1309 mAh g^{-1} *vs.* ~1105 mAh g^{-1}) and capacity retention after 50 cycles at 0.1 C rate (1037 mAh g^{-1} *vs.* ~613 mAh g^{-1}). The enhancement in electrochemical performance becomes more pronounced at 0.2 C rate. The cell with the CNTs/V_2O_5 RSL delivers a capacity of 1323 mAh g^{-1} and an area capacity of 7.94 mAh cm^{-2} after the 1st activation cycle and maintains ~100% Coulombic efficiency for 100 cycles. On the contrary, the cell with the CNTs RSL exhibits a lower capacity of 890 mAh g^{-1} during the 2nd cycle and failed after 12 cycles due to shuttling effect. Owing to the high interfacial resistance, the cell with Celgard PP separator lost most of its capacity after 6 cycles.

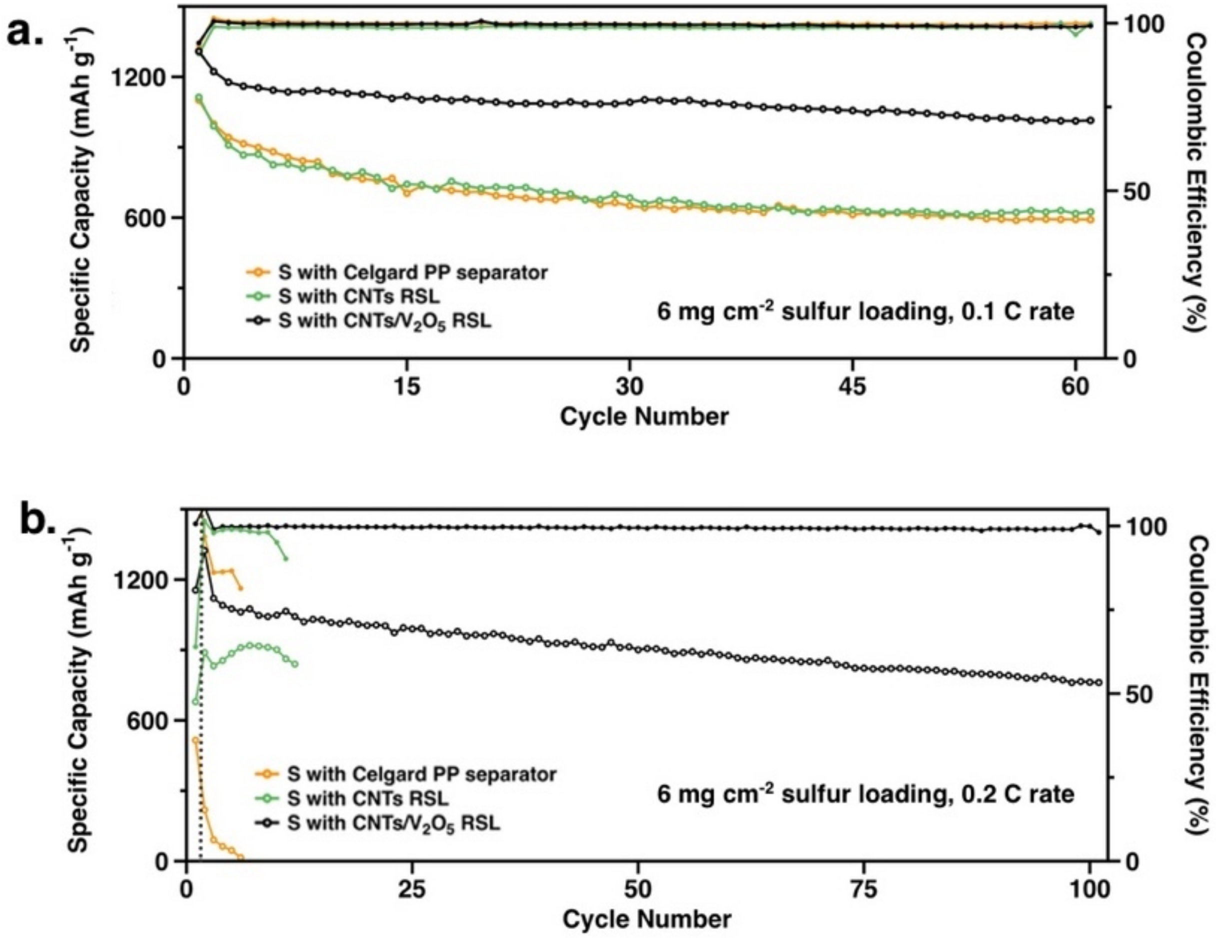

Figure 6.9 Galvanostatic cycling performance of sulfur cathode with a mass loading of 6 mg cm^{-2} at **a.** 0.1 C rate and **b.** 0.2 C rate.

The initial specific capacities and sulfur contents of the lithium-sulfur cells are further calculated based on the total weight of the cathodes, which includes the weights of the carbon/sulfur composite, conductive agent, binder and RSL. As shown in Table 6.1, the weight contribution of CNTs/V_2O_5 RSL only slightly reduces the overall sulfur content from 70.4% to 66.6%. Given that the incorporation of CNTs/V_2O_5 RSL significantly enhances the utilization of sulfur, the specific capacity of the cathode with CNTs/V_2O_5 RSL is still much higher than those with CNTs RSL or Celgard PP separator (814 mAh g^{-1} *vs.* ~700 mAh g^{-1}).

Table 6.1 Comparison of sulfur contents and initial specific capacity of lithium-sulfur cells with different interlayers.

Interlayer material	Loading of sulfur (mg/cm^2)	Loading of interlayer (mg/cm^2)	Sulfur content (%)		Initial specific capacity at 0.1 C rate (mAh/g)		
			Based on cathode	Based on cathode and interlayer	Based on sulfur	Based on cathode	Based on cathode and interlayer
CNTs/V_2O_5	6	0.49	70.4	66.6	1223	861	814
CNTs	6	0.13	70.4	69.3	991	698	694
Celgard PP	6	0	70.4	70.4	999	703	703

With 100 wt-% lithium excess and E/S ratio of 5, the cell with CNTs/V_2O_5 RSL delivers a much higher initial energy density of 365 Wh kg^{-1} with a lower capacity fading rate of 0.303% per cycle, while the ones with CNTs RSL exhibits an energy density of 311 Wh kg^{-1} with a capacity fading rate of 0.77% per cycle. The specific capacity and average working potential of Li-S cells are based on the electrochemical performance of coin cells, while the mass is based on the whole cell, which includes the weights of separator, RSL, sulfur cathode, lithium anode and liquid electrolytes. The comparison clearly distinguishes our work from current state of the art. As shown in Figure 6.10, the energy density of Li-S cells increases with higher sulfur loadings, lower ratio between the volume of electrolyte and the mass loading of sulfur (E/S, µL/mg), as well as higher specific capacities of active materials. With further optimization of the ratio of E/S (*e.g.,* E/S=3) and addition of electroactive solvent into the electrolyte, the specific capacity of sulfur may achieve 1500 mAh g^{-1} and the energy density of the cell can possibly reach up to 560 Wh kg^{-1}, which could bring Li-S batteries to practical applications.

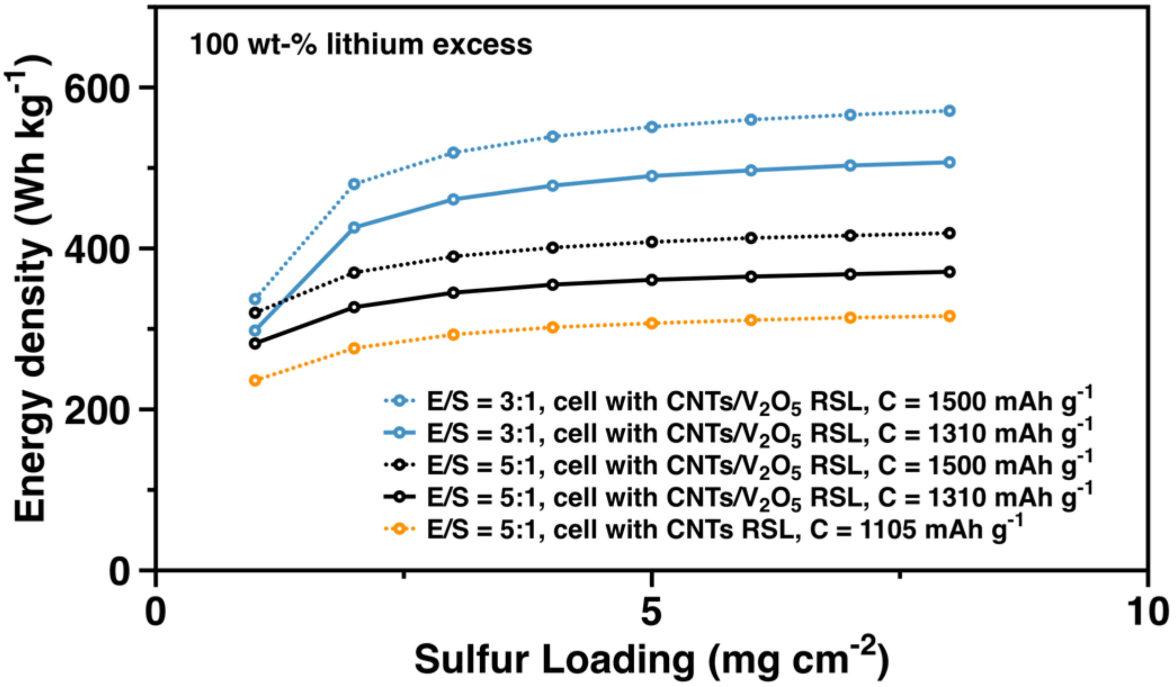

Figure 6.10 Energy densities of Li-S cells with different sulfur loadings, ratios between electrolyte and sulfur (E/S) and specific capacities of active materials.

To quantify the capacity contribution from V_2O_5 moieties, cells with lithium as the anode and CNTs/V_2O_5 RSL as the cathodes were assembled and tested under similar condition. It was found that the capacity contribution from the CNTs/V_2O_5 RSL is less than 1% of the overall capacity of the Li-S cells (Table 6.2). It is reasonable to conclude that the enhanced performance for the cells with CNTs/V_2O_5 RSL is mainly attributed to the polysulfide-scavenging effect and the enhanced conductivity.

Table 6.2 Table of capacity contributions from CNTs RSL and CNTs/V_2O_5 RSL in Li-S cells with various sulfur loadings at 1 C rate.

	Sulfur loading	
	1 mg cm^{-2}	2 mg cm^{-2}
Capacity of sulfur cathode with CNTs RSL (mAh)	1.4	1.5
Capacity of sulfur cathode with CNTs/V_2O_5 RSL (mAh)	1.6	2.3
Capacity of the CNTs RSL (mAh)	0.011	0.01
Capacity of the CNTs/V_2O_5 RSL (mAh)	0.013	0.01
Capacity contribution from the CNTs RSL (%)	0.78%	0.67%
Capacity contribution from the CNTs/V_2O_5 RSL (%)	0.81%	0.43%

To further examine the scavenging effect, we equilibrated RSL in Li_2S_6 solutions with various concentrations and used them as the cathodes. The amount of polysulfides scavenged was determined *via* an electrochemical method. It was found that the maximum amount of Li_2S_6 scavenged by the CNTs RSL and CNTs/V_2O_5 RSL is 0.110 mg and 0.486 mg, respectively (Figure 6.11 a). After wiping off the residual solution on the surface, cells were assembled using the equilibrated RSL as the cathode and lithium metal as the anode. Both cells exhibit an open circuit voltage (OCV) of ~2.36 V, which is the same as the redox potential of the polysulfides. The cells were then held at 2.8 V till the current reached 1 μA, during which the Li^+ from the adsorbed polysulfides was stripped off from the RSL. The total charges were measured and converted to the amount of Li_2S_6 adsorbed on the RSL. Furthermore, the polysulfides scavenged by the RSL could be released and recaptured reversibly upon cycling between 2.8 V to 1.7 V (Figure 6.11 b and c). Upon cycling for ten cycles, the CNTs RSL exhibited significantly capacity decay whereas the

CNTs/V_2O_5 RSL retains the initial capacity (the amount of polysulfide scavenged), clearly indicating the outstanding scavenging and regenerative capability of the CNTs/V_2O_5 RSL.

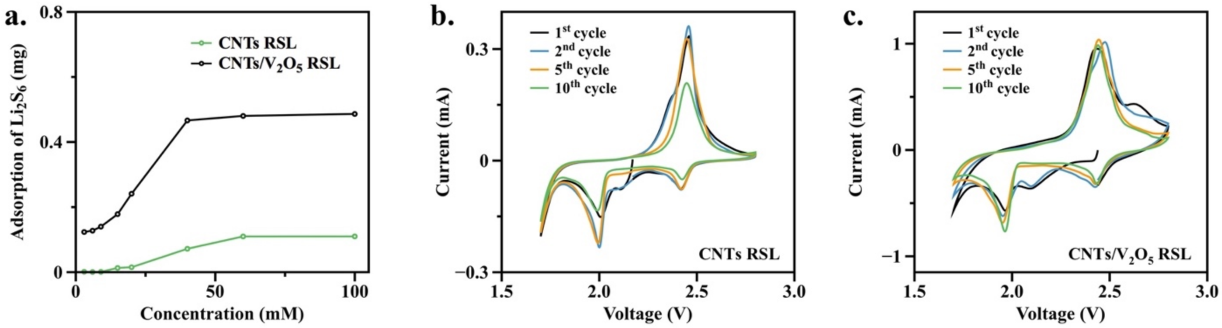

Figure 6.11 a. Scavenging capacitance of the CNTs and CNTs/V_2O_5 RSL at different Li_2S_6 concentrations. Cyclic voltammetry of the equilibrated **b.** CNTs RSL and **c.** CNTs/V_2O_5 RSL cathodes at a scanning rate of 0.05 mV s^{-1}.

Besides the improved capacity, cycling stability and rate performance, the use of CNTs/V_2O_5 RSL also dramatically reduced the self-discharge rate of Li-S cells. After cycling at 0.2 C rate for 9 cycles, the 10^{th} discharge was stopped at 2.1 V, a voltage corresponding to the maximized concentration of polysulfides in the cells.[103,104] Then the discharge process was resumed after 3 days, during which the diffusion of polysulfides could cause self-discharge of the cells. Figures 6.12 display the charge-discharge voltage *vs.* capacity for cells without and with the CNTs/V_2O_5 RSL before and after the resting. As can be seen here, the cell without the RSL exhibits a discharge capacity of 674 mAh g^{-1} in the 9^{th} cycle (denoted as C_{9th}), which decreases to 539 mAh g^{-1} after the resting (denoted as C_{10th}). On the contrary, the cell with the RSL delivers a much higher capacity of 1174 mAh g^{-1} in the 9^{th} cycle (C_{9th}), and still maintains the high capacity after the resting (1145 mAh g^{-1}, C_{10th}). For quantitative analysis, the self-discharge rate of the cells can be estimated by $(C_{9th}-C_{10th})/C_{9th} \cdot 100\%$. Upon incorporating the RSL, the self-discharge rate of the cell was decreased from 26.7% to 2.5%, suggesting the significant role of the CNTs/V_2O_5 RSL in blocking diffusion of polysulfides and minimizing the self-discharge rate, which is essential for practical utilization of lithium-sulfur batteries.

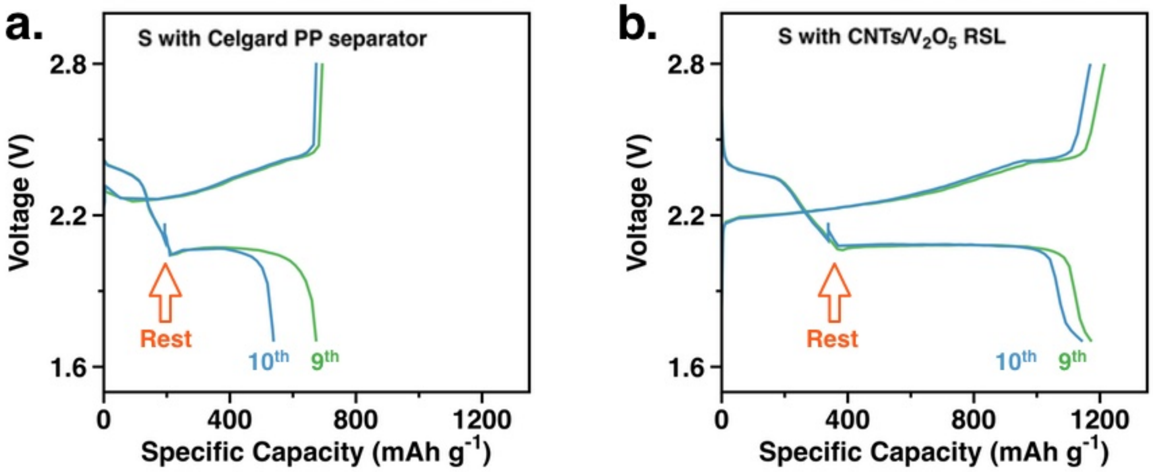

Figure 6.12 Self-discharge tests of sulfur cathodes with **a.** PP separator and **b.** CNTs/V_2O_5 RSL. The cells were cycled at 0.2 C for 9 cycles, stopped at 2.1 V during 10th discharge and rested for 3 days before the discharge process was resumed.

6.5 Characterizations of the scavenging and regeneration process.

To further understand the scavenging and regenerating process, we studied the distribution of sulfur moieties within the CNTs/V_2O_5 RSL at different electrochemical stages with SEM and energy dispersive x-ray (EDX) spectroscopy. Li-S cells with CNTs/V_2O_5 RSL were cycled at 0.3 C and interrupted at 2.05 V during discharge or 2.60 V during charge, respectively. The CNTs/V_2O_5 RSL were then disassembled from the cells and dried in an argon-filled glove box for SEM and EDX studies. Figure 6.13 a displays a cross-section SEM image and the corresponding EDX analysis of the RSL interrupted at 2.05 V. At this electrochemical stage, sulfur is mainly converted to polysulfides located within the electrode and in the electrolyte. EDX analysis shows two peaks associated with sulfur and vanadium co-localized in the center, indicating that the sulfur moieties are distributed dominantly within the V_2O_5 layer (less amount of sulfur in the CNTs region). This observation is consistent with the critical role of V_2O_5 in scavenging the polysulfides. Figure 6.13 b presents a cross-section SEM image and the corresponding EDX analysis of the RSL interrupted at 2.60 V. At this electrochemical stage, the scavenged polysulfides are partially stripped away while the RSL is being regenerated. Consistently, EDX analysis also shows two co-localized peaks for sulfur and vanadium but with significantly less amount of sulfur species.

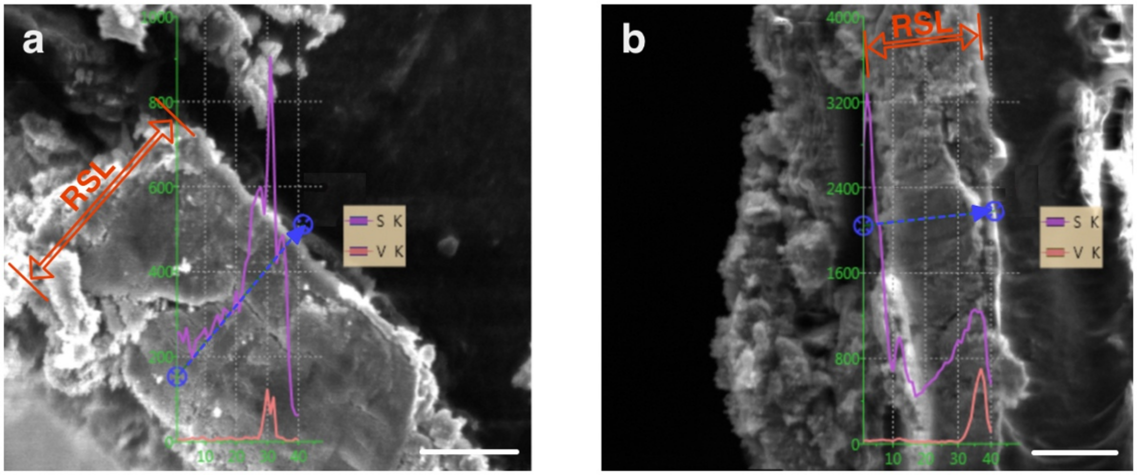

Figure 6.13 SEM image and element-mapping of CNTs/V_2O_5 RSL at discharged and charged stages. Li-S cells were cycled at 0.3 C between 1.7 to 2.8 V and **a.** interrupted at 2.05 V during the discharge or **b.** interrupted at 2.60 V during the charge. The blue arrows show the direction of the line scan, while the blue circles represent the starting and ending points. Purple line represents sulfur and orange line represents vanadium. Scale bars are a. 20 µm and b. 25 µm.

The scavenging ability of CNTs/V_2O_5 RSL also alleviate the corrosion of lithium anodes during cycling. As shown in Figure 6.14 and Figure 6.15, the lithium anode from the cell with CNTs RSL exhibits a rough surface with a thick sulfur-containing passivation film (~300 µm). In comparison, the lithium anode from the cell with CNTs/V_2O_5 RSL maintains a smooth surface with a significantly thinner penetration of polysulfides (~80 µm depth), indicating 73.3% less lithium corrosion.

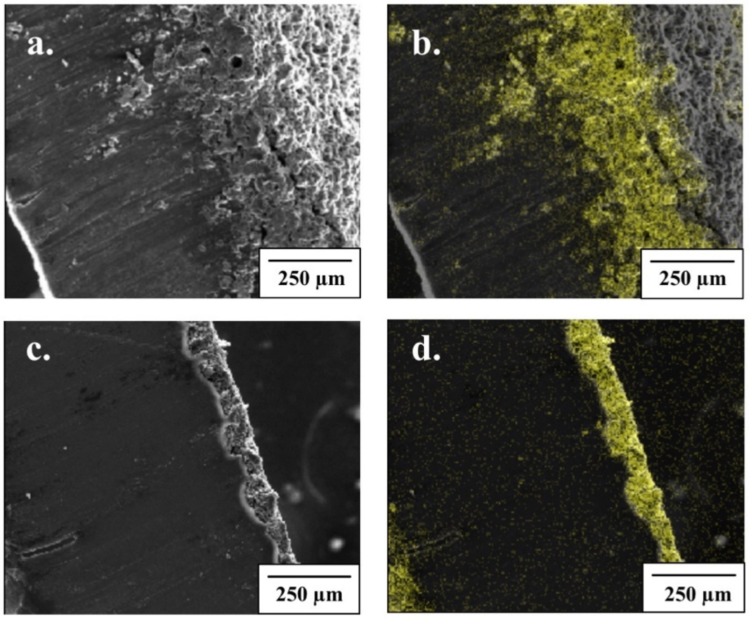
a.
b.
c.
d.
250 µm
250 µm
250 µm
250 µm

Figure 6.14 Cross-sectional SEM images and elemental mappings of lithium anodes after cycling with sulfur cathodes with and without the RSL. Li-S cells were assembled with **a-b**. CNTs RSL and **c-d**. CNTs/V_2O_5 RSL. Yellow color represents the distribution of sulfur species.

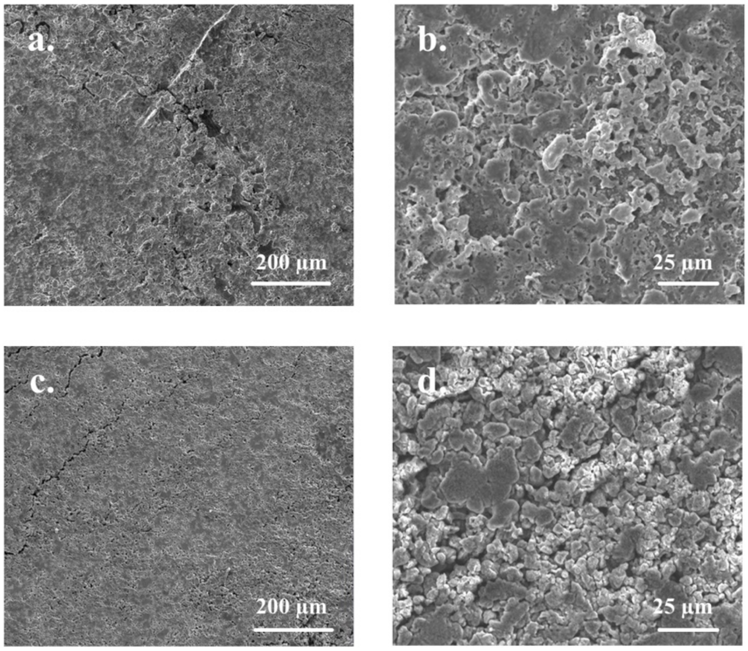
a.
b.
c.
d.
200 µm
25 µm
200 µm
25 µm

Figure 6.15 SEM images of lithium surface after cycling at 1 C for 50 cycles **a.** and **b.** Li-S cell with CNTs RSL, **c.** and **d.** Li-S cell with CNTs/V_2O_5 RSL.

6.6 Working mechanisms of metal oxides.

The scavenging effect is supposed to originate from the chemical-physical adsorption and/or reactions between polysulfides and the CNTs/V_2O_5 RSL. To explore the mechanism, we used Li_2S_6 as a representative polysulfide species, which was mixed with V_2O_5 nanowires. The resulted oxide/sulfide solid was isolated and investigated using x-ray photoelectron spectroscopy (XPS) analysis.

XPS spectra of V_2O_5 before and after mixing with Li_2S_6 are presented in Figures 6.16 a-b. V_2O_5 displays a typical $2p_{3/2}$ spectrum for the V^{5+} state at 517.5 eV. After the mixing, the $2p_{3/2}$ peak splits into two peaks centered at 517.5 eV and 516.0 eV, which are originated from the V^{5+} and V^{4+} states, respectively.[105] Figures 6.16 c-d further compare the sulfur 2p core spectra of Li_2S_6 and oxide/sulfur solid. Li_2S_6 exhibits two sulfur states at 163.0 eV and 161.7 eV, which can be assigned to bridging (S_B^0) and terminal (S_T^{-1}) sulfur atoms in polysulfide anions, respectively.[72,106,107] The ratio between S_B^0 and S_T^{-1} is around 2:1, which is in accordance with the composition of Li_2S_6. In contrast, the S 2p spectrum of the oxide/sulfide solid illustrates two sulfur states, which can be attributed to S_B^0 at 163.2 eV and polythionate complex at 167.9 eV, respectively.[106] The formation of V^{4+} and the polythionate complex suggests the occurrence of redox reactions between Li_2S_6 and V_2O_5, forming Li-V-O-S complexes. Meanwhile, the terminal sulfur atoms (S_T^{-1}) were not detected in the oxide/sulfide solid, suggesting that the Li^+ ions, which were paired with the polysulfides, are intercalated or inserted into V_2O_6.

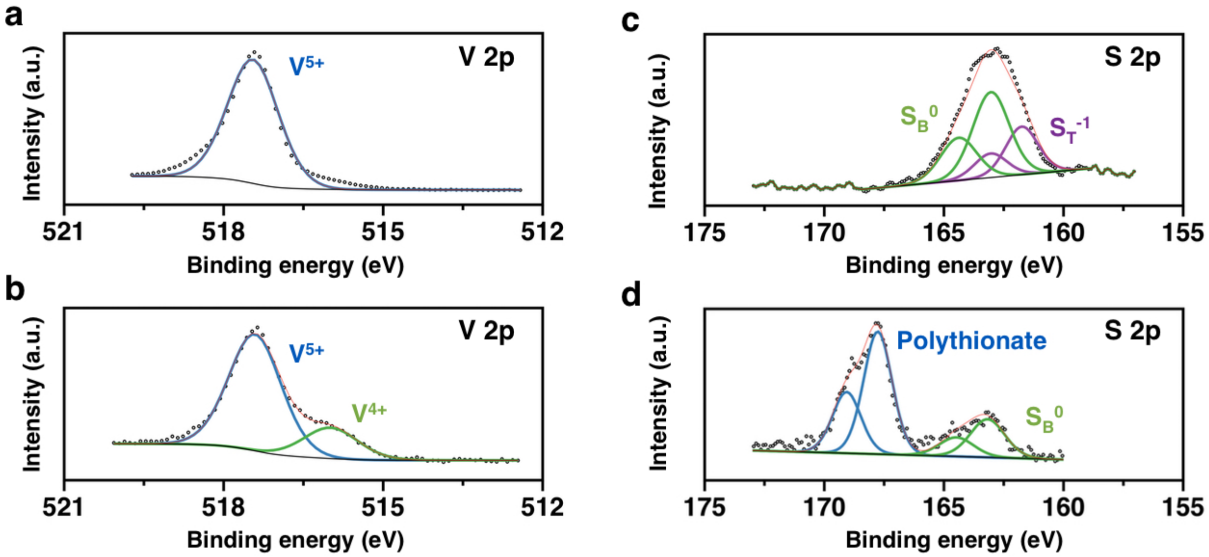

Figure 6.16 Reactions between V_2O_5 and polysulfides probed by XPS. **a.** Vanadium $2p_{3/2}$ spectra of V_2O_5 and **b.** V_2O_5/sulfide compound formed by reacting V_2O_5 with Li_2S_6, indicating the formation of V^{4+} in the presence of Li_2S_6. **c.** Sulfur 2p core spectra of Li_2S_6 showing the terminal (S_T^{-1}) and bridging (S_B^0) sulfur atoms with an expected ratio of 1:2. **d.** Sulfur 2p core spectra of the V_2O_5/sulfide compound. The formation of polythionate groups indicates redox reactions between Li_2S_6 and V_2O_6.

Based on the studies presented above, a possible mechanism can be constructed: During discharge, soluble polysulfides are continuously generated in the cathode and tend to diffuse toward the anode. With the incorporation of CNTs/V_2O_5 RSL, polysulfides are adsorbed and oxidized by the embedded oxide, forming solid-state [Polysulfides-RSL] complex and being immobilized. In the subsequent charge/delithiation process, lithium ions and polysulfides are stripped away from the RSL and re-deposited onto the electrodes, respectively. Through such a dynamic and regenerative process, the shuttling effect of polysulfides can be effectively mitigated, leading to Li-S batteries with significantly improved electrochemical performance.

6.7 Chemisorption *vs.* physisorption

Thermodynamically, adsorption occurs spontaneously between solid-gas and solid-liquid interfaces to balance the chemical potentials between the interfaces. When the redox potential of the polysulfides is above the conduction bands of the oxide, electrons from the polysulfides can be transferred to the oxides, resulting in chemisorption with new chemical-bond formations (Figure 6.17).

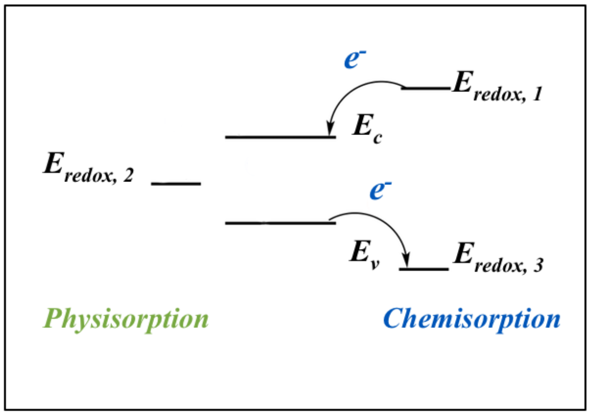

Figure 6.17 Electron transfer directions regarding the relative positions of conduction bands and valence bands of the oxides and redox potential of the molecule.

The binding energies in physisorption and chemisorption are completely different. For physisorption, the adsorption is mainly governed by work function (or surface energy, which is proportional to surface potential) of the oxides. An oxide with a higher surface potential may build up a stronger electric field within its Debye length, resulting in a stronger adsorption of the adsorbates (Figure 6.18 a).[108] In the other hand, in chemisorption, the bond energy between adsorbents and adsorbates is related to their dissociation energy,[109] electronegativity and chemical hardness,[110] which can be calculated with Flore's equation (Figure 6.18 b).[111]

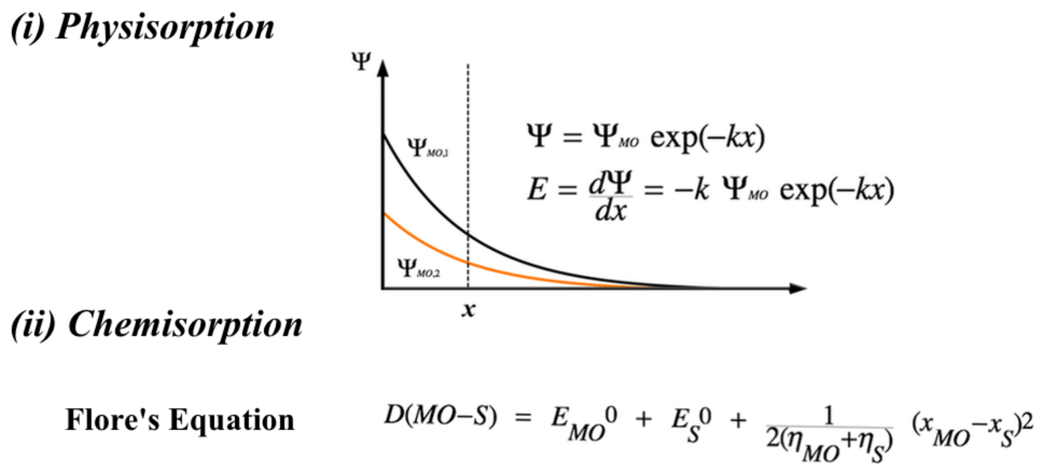
(i) Physisorption
Ψ
Ψ_{MO1}
Ψ_{MO2}
$\Psi = \Psi_{MO} \exp(-kx)$
$E = \frac{d\Psi}{dx} = -k\ \Psi_{MO} \exp(-kx)$
x
(ii) Chemisorption
Flore's Equation
$D(MO-S) = E_{MO}^0 + E_S^0 + \frac{1}{2(\eta_{MO}+\eta_S)} (x_{MO}-x_S)^2$

Figure 6.18 The interaction in physisorption and chemisorption.

In this regard, a series of metal oxides with distinct electronic structures were mixed with Li_2S_6 solutions and then centrifuged (Figure 6.19). The Li_2S_6 solution (control) exhibits a dark brown color, while the mixtures containing CNTs, CeO_2, ZnO, MgO, Al_2O_3, MoO_3, TiO_2, WO_3, or V_2O_5 show increasingly lighter color, indicating an increasing degree of adsorption or reaction of the sulfides with oxides. This observation suggests that various oxides could be used as the blocking moieties for RSL fabrication.

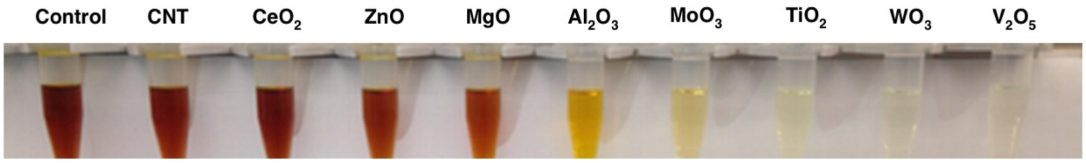
Control
CNT
CeO_2
ZnO
MgO
Al_2O_3
MoO_3
TiO_2
WO_3
V_2O_5

Figure 6.19 Photographs of Li_2S_6 solutions mixed with metal oxides after centrifugation.

To understand the adsorption and chemical reaction of polysulfides with the RSL, Figure 6.20 compares the redox potentials of polysulfides (E_{redox}) with the conduction bands (E_c) of commonly used metal oxides.[110,112-114] For Li-S batteries, the redox potentials of polysulfides exist in the range from 2.2 to 2.5 V (*vs.* Li^+/Li) depending on their compositions,[103] which is marked as purple. Based on the relative position of the conduction bands, such oxides can be categorized into two groups: one group that can physically adsorb polysulfides without electron transfer (physisorption) including MgO, Al_2O_3, SiO_2, Li_2O, CeO_2, PbO, NiO and ZnO; the other group that can react with polysulfides (chemisorption) including SnO_2, CoO, TiO_2, Fe_2O_3, CuO, MnO_2, MoO_3, V_2O_5, WO_3, and CrO_3.

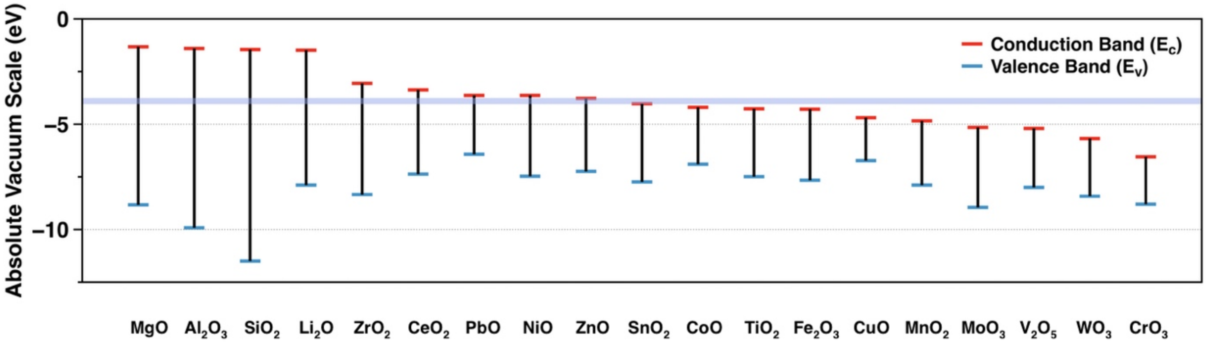

Figure 6.20 Absolute potentials of the conduction bands and valence bands of various metal oxides, as well as the oxidation potential of polysulfides (2.2 to 2.5 V *vs.* Li^+/Li, labeled in purple).

Figure 6.21 displays the work functions of a series of oxides,[110] which can be used as an indicator for their ability in physisorption or polysulfide-scavenging capability. Comparing with MgO, CeO_2 and ZnO, Al_2O_3 has the highest work function and the best polysulfide-scavenging performance as observed in the visual experiment, in which the Li_2S_6 solutions with MgO, CeO_2 or ZnO remain brownish while that with Al_2O_3 shows light yellow color.

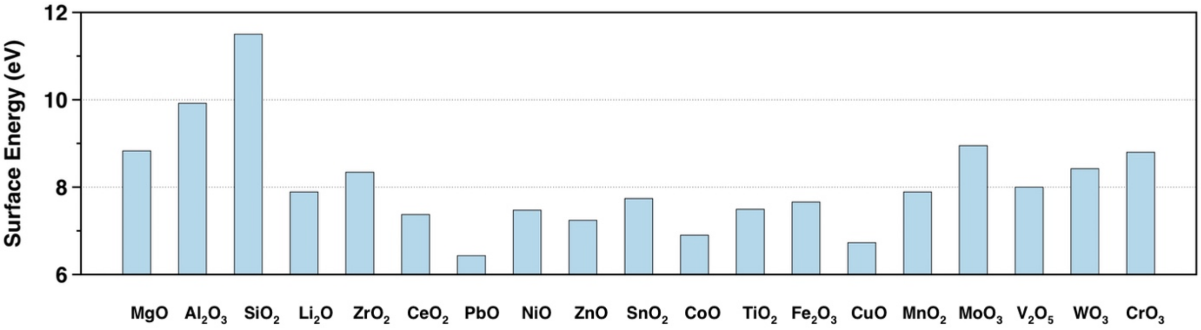

Figure 6.21 Work functions of a series of metal oxides.

In terms of the oxides with E_c lower than E_{redox}, chemisorption occurs, where the color of the Li_2S_6 solutions diminished immediately upon contact with the oxides (MoO_3, TiO_2, WO_3 and V_2O_5). It is reasonable to hypothesize that stronger bond energy between an oxide and the polysulfides should lead to better scavenging or blocking effect. To examine such a hypothesis, a series of CNTs/oxide RSL were fabricated using CNTs and different oxides and their polysulfide-scavenging capability was evaluated. Figure 6.22 presents their bond energies with polysulfides, as well as capacities of Li-S cells with such RSL after 100 cycles at 1C. As shown here, there is a significant correlation between bond energy and cycling stability: stronger bond energies between the oxides and polysulfides lead to higher capacity retention rates, as well as lowered self-discharge rates (Figure 6.23). For example, WO_3 and polysulfides exhibit high bond energy of 13.62 eV, leading to cells with a high capacity of 1075 mAh g^{-1} and a near-zero self-discharge rate. CuO and polysulfides show a lower bond energy of 9.83 eV, as expected, resulting in lower capacity retention of 572.9 mAh g^{-1} and ~ 9.0% of self-discharge rate. This observation suggests that it is possible to use the bond energy between the scavenging materials and polysulfides to evaluate or predict their polysulfide-scavenging capability, providing quantified guidance for Li-S batteries.

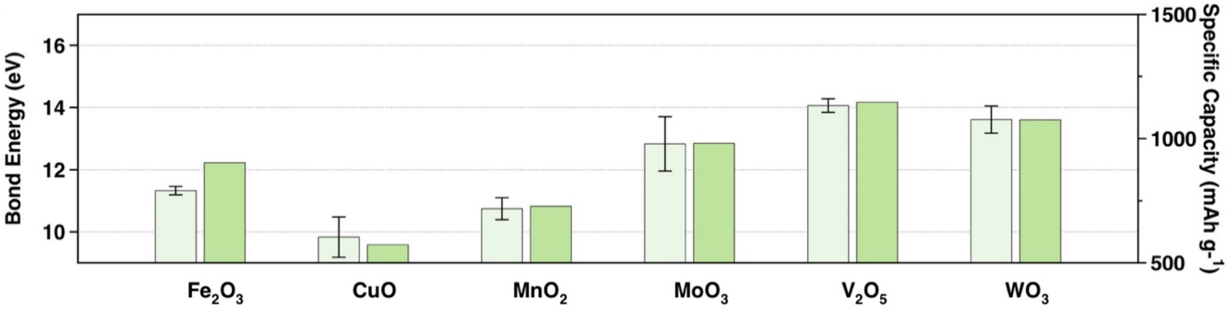

Figure 6.22 A comparison of the bond energies between the metal oxides and polysulfides (Light green) with the specific capacity of the corresponding Li-S cells after 100 cycles at 1 C (Green).

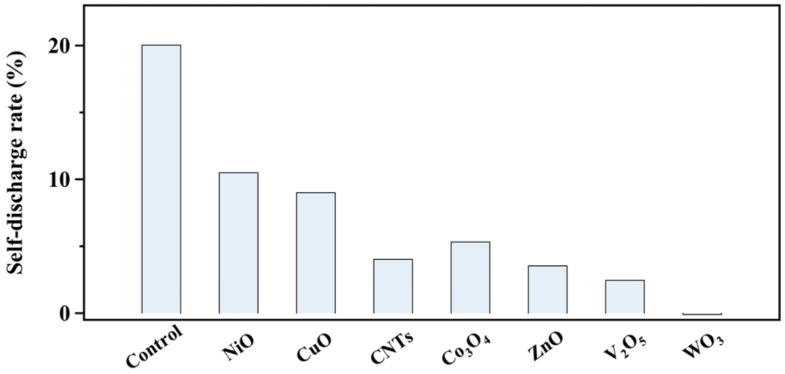

Figure 6.23 Self-discharge rate of Li-S cells with different CNTs/oxide RSL.

6.8 Conclusion

In this chapter, we have developed a class of RSL based on CNTs and oxides with low-dimension forms, which can dynamically block the diffusion of polysulfides and regenerate themselves during cycling. Li-S batteries with CNTs/V_2O_5 RSL exhibit high areal capacity of >6 mAh cm^{-2} for 60 cycles, dramatically extended cycling life (>100 cycles *vs.* 12 cycles), low self-discharge rate of 2.45% after resting for 3 days and ~73.3% less lithium corrosion. With further optimization, the energy density of the cell with RSL can possibly reach up to 560 Wh kg^{-1}, which could bring Li-S batteries to practical applications. Rooting from the electronic structure of the oxides and the redox potentials of polysulfides, the scavenging capability of the oxides is thoroughly investigated and correlated with the electrochemical performance of Li-S cells. This work not only offers a class of polysulfide-scavenging layers to address the shuttling effect effectively, but also provides quantified design framework towards Li-S batteries with high energy density and prolonged cycling life, which brings them one step closer to practical applications.

Chapter 7 Redox-mediators based on transitional metal oxides

7.1 Introduction

The electrochemical reaction in sulfur cathode involves several species, such as sulfur (S_8), lithium polysulfides (Li_2S_n, $4 \leq n \leq 8$) or sulfur radicals, lithium persulfide (Li_2S_2) and lithium sulfide (Li_2S). Their poor electronic conductivity results in their sluggish electrochemical responses. The slow electron transfers in these species lead to large over-potentials and limited utilization of active materials, especially under high current densities. Many efforts have been made to expedite their electrochemical responses, mainly focused on hosting the active materials within conductive scaffolds such as porous carbons composites.

Compared to artificial electronic devices, biological systems transport electrons in a more efficient manner, usually facilitated by redox mediators or electron shuttles. For instance, $NADP^+$/NADPH ($NADP^+$: nicotinamide adenine dinucleotide phosphate) is one of the redox pairs involved in photosynthesis. In thylakoid space, water is split into protons, electrons, and molecular oxygen. Protons and electrons are subsequently used to synthesize NADPH, which reduces CO_2 into hydrocarbon through the Calvin cycle, and converts back to $NADP^+$ (Figure 7.1 a). Similar mediators also exist in the cellular respiration process, in which NADH (reduced form of nicotinamide adenine dinucleotide) carries the electrons released by catabolic reactions to the inner mitochondrial membrane, dispatches them to Complex I in the respiratory chain, and forms NAD^+. Through several protein complexes, the electrons are passed onto O_2 to generate H_2O. The presence of these redox mediators enables the efficient electron harvesting and utilization, which are essential for biochemical processes. Utilizing a similar concept, redox couples (*e.g.*, iodide/triiodide) have also been explored in dye-sensitized solar cells. While iodide regenerates the photo-oxidized dye in the electrolyte, triiodide diffuses to the counter electrode and accepts the electrons from the external circuit, enabling the continuous charge separation and electron transportation within the cell (Figure 7.1 b).

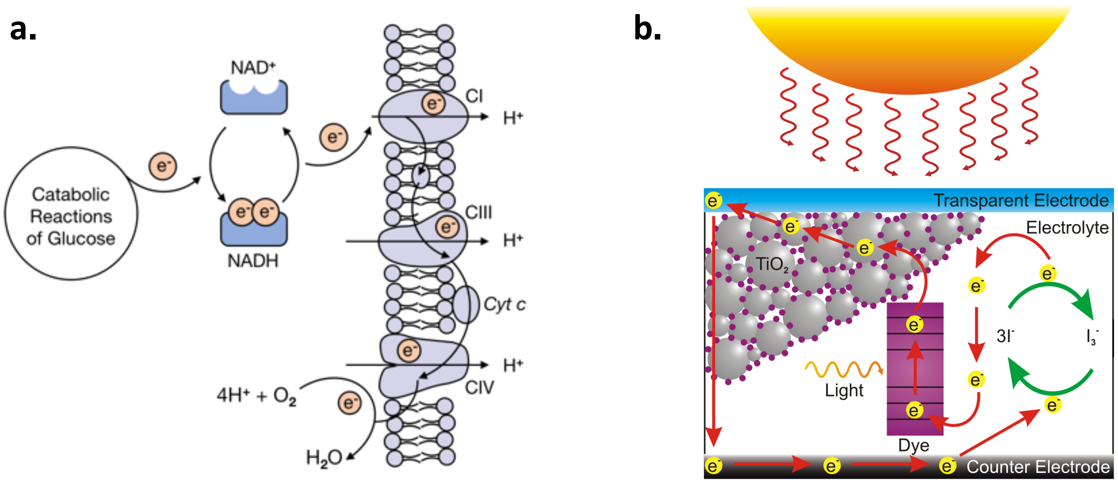

Figure 7.1 Illustration of electron transfer process in **a.** photosynthesis and **b.** dye-sensitized solar cells. Reproduced from Wikipedia.

7.2 Geometric and electronic structures of redox mediators

Orthorhombic Nb_2O_5 and birnessite MnO_2 are known as pseudocapacitive oxides with fast electrochemical kinetics and long cycling life. In terms of electrochemical behaviors, $Nb_2O_5/Li_xNb_2O_5$ ($0<x<1.25$) delivers the majority of its capacity between 1.2-2 V (*vs.* Li/Li^+),[115,116] while MnO_2/Li_yMnO_2 ($0<y<1$) is electrochemically active between 2.4-3.6 V (*vs.* Li/Li^+).[117,118] Given that the redox potentials of sulfur species lie in between these ranges, they are employed as the reductive mediator and oxidative mediator for sulfur species, respectively.

To unveil the fundamental differences between sulfur species and these oxides in electrochemical behaviors, we investigated the geometric structures of Nb_2O_5 and MnO_2 before and after lithiation. As shown in Figure 7.2 a, orthorhombic Nb_2O_5 presents a unit cell with NbO_6 octahedra and NbO_7 pentagonal bipyramids connecting each other by sharing edges or vertexes[119,120]. All the niobium cations are arranged in a plane perpendicular to the [001] direction.

After lithiation, lithium cations occupy the interstices of NbO_x polyhedrons (Figure 7.2 b), and the structure only experiences a slight expansion (Table 7.1).

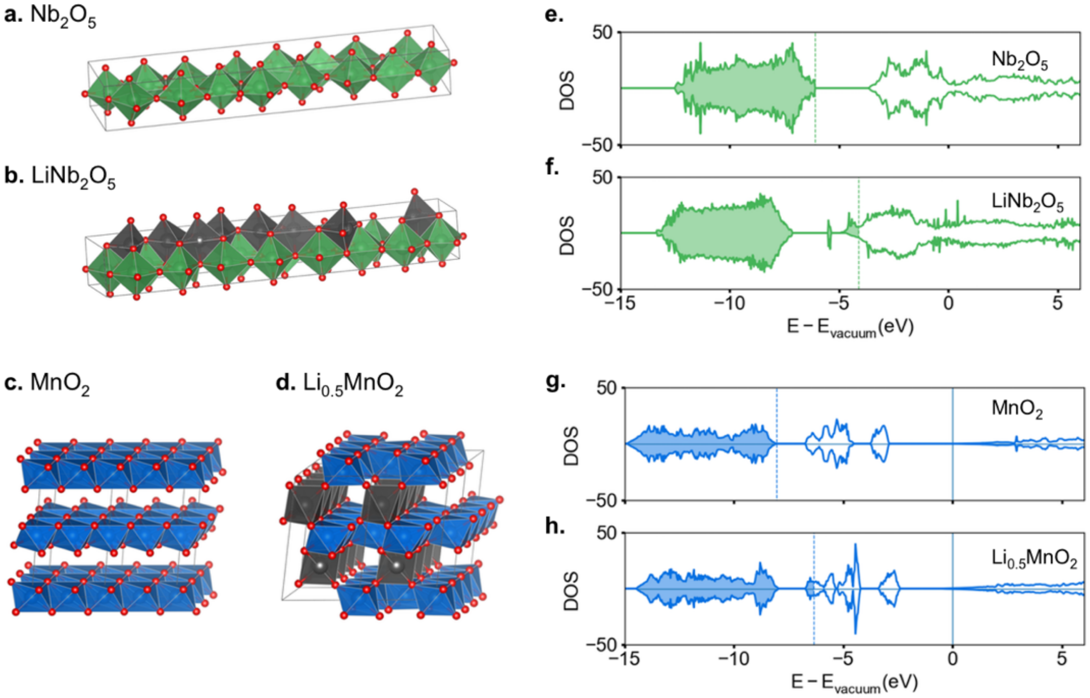

Figure 7.2 Geometric and electronic structures of redox mediators. The geometric structure of **a.** Nb_2O_5, **b.** $LiNb_2O_5$, **c.** MnO_2, and **d.** $Li_{0.5}MnO_2$. The corresponding electronic density of states of **e.** Nb_2O_5, **f.** $LiNb_2O_5$, **g.** MnO_2, and **h.** $Li_{0.5}MnO_2$. Lithium, niobium, manganese, and oxygen atoms are shown in gray, green, blue, and red, respectively. Shadowed area represents filled valence band, while unfilled area indicates an empty conduction band. The vertical dashed lines and solid lines show the positions of VBM and CBM, respectively.

Table 7.1 Lattice parameters of T-Nb_2O_5 and $LiNb_2O_5$.

x in $Li_xNb_2O_5$	a	b	c	α	β	γ
0.0	6.176	29.175	3.931	90	90	90
1.0	6.315	29.117	3.931	90.006	90.064	90.617

Table 7.2 Lattice Parameters of MnO_2 and $Li_{0.5}MnO_2$.

x in Li_xMnO_2	a	b	c	α	β	γ
0.0	5.654	5.654	9.506	90.0	90.0	120.04
0.5	5.661	5.691	9.651	89.8	101.4	118.08

The unit cell of birnessite MnO_2 is in a hexagonal structure with a symmetry of P_{63}/mmc (Figure 7.2 c)[121,122]. Mn^{4+} cations exist as MnO_6 octahedra that share edges within the same layer and the interlayer distance is 4.75 Å. After lithiation, lithium cations are placed in the interlayer region, at the center of the distorted octahedral site, formed by 3 oxygen anions in the upper layer of MnO_6 and 3 oxygen in the lower layer of MnO_6 (Figure 7.2 d). LiO_6 octahedra align in the [100] direction and no face-sharing structure are formed between LiO_6 octahedron and MnO_6 octahedron (Table 7.5).

Furthermore, Figure 2e-h illustrates the electronic band structure of these redox mediators. Both Nb_2O_5 (Figure 7.2 e) and MnO_2 (Figure 7.2 g) present moderate band gaps of 2.4 eV and 1.3 eV, respectively. More importantly, the lithiation process barely changes the shape of their valence bands, but significantly lowers their absolute band energies (Figure 7.2 f and Figure 7.2 h). This implies weak hybridization between lithium *2s* and oxygen *2p* orbitals. Given that their conduction bands are partially filled after lithium insertion, $LiNb_2O_5$ and $Li_{0.5}MnO_2$ are expected to exhibit high electronic conductivity due to their metallic characteristics. The minimum phase transitions during lithiation and delithiation, as well as the high electronic conductivities of Nb_2O_5 and MnO_2 result in their fast electrochemical responses. The asymmetric electronic state of $LiNb_2O_5$ indicates that it is EPR active, which is consistent with the EPR result (Figure 7.3 a-b).

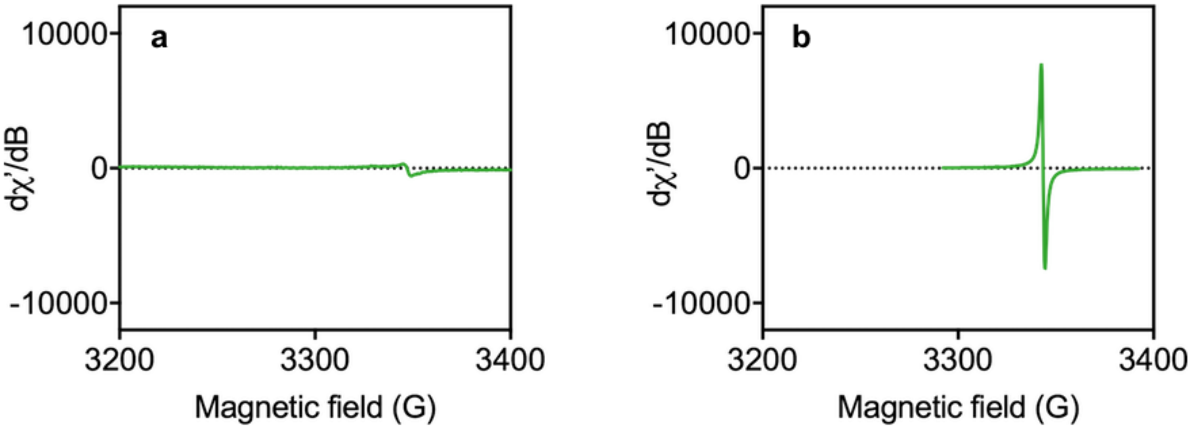

Figure 7.3 Electron paramagnetic resonance spectrum of **a.** Nb_2O_5 and **b.** $LiNb_2O_5$ at 5 K, illustrating the formation of EPR active species Nb^{4+}.

7.3 Methods

7.3.1 Synthesis of RGO and RGO-metal oxides composites.

Reduced graphene oxide (RGO) was prepared by oxidation of natural graphite flacks (Sigma-Aldrich) following Hummers method and then reduced by ascorbic acid (Sigma-Aldrich) at 90 ˚C for 2 h (pH = 10). The resulted solid product was washed with deionized water for several times until pH reaches 7. After freeze-drying, RGO was obtained.

RGO-Nb_2O_5 composites were synthesized according to the previously reported procedure. Briefly, 25 mg $NbCl_5$ (Sigma-Aldrich) was dissolved in 5 mL of ethanol (Fisher Scientific). In a separate vial, 110.7 mg RGO was dispersed in 50 mL ethanol by sonication. Both vials were chilled in an ice bath for 2 h. The two solutions were then mixed while 0.5 mL oleylamine (Sigma-Aldrich) and 8.3 μL deionized water were slowly injected. The solution was heated at 75 ˚C in an oil bath with magnetic stirring for 6 h. The resulted product was washed with ethanol and water to remove excess oleylamine and then freeze-dried. After annealing at 600 ˚C for 3 h in argon, RGO-Nb_2O_5 composites were obtained.

RGO-MnO_2 composites were synthesized at room temperature. First, 3.175 mg $MnSO_4 \cdot H_2O$ (Sigma-Aldrich) was dissolved in 2.5 mL deionized water. In a separate vial, 109.5 mg RGO was dispersed in 15 mL deionized water by sonication. The two solutions were then mixed and form a homogenous solution. Then, 10 mg $KMnO_4$ (Sigma-Aldrich) was dissolved in 2.5 mL deionized water and added to the previous solution. This solution was further stirred at room temperature for 12 h. The resulting solid product was washed with water for several times and then freeze-dried.

Synthesis of S-RGO and S-RGO-metal oxides composites. The sulfur and RGO composites (denoted as S-RGO composites) were prepared using a liquid infiltration method at 159 ˚C for 4 h. S-Nb_2O_5 composites, S-MnO_2 composites and S-Nb_2O_5-MnO_2 were synthesized *via* similar method by replacing RGO with RGO-Nb_2O_5, RGO-MnO_2, and mixed RGO-Nb_2O_5 and RGO-MnO_2 composites (weight ratio = 1:1). The weight ratio between sulfur and RGO (or RGO-metal oxides composites) was 4:1.

Preparation of sulfur cathodes. Sulfur cathodes were prepared using a slurry casting method. Carbon/sulfur composites, carbon fiber (Pyrograf Product Inc.) and sodium alginate (Sigma-Aldrich, 4 wt-% solution in deionized water) were mixed with a weight ratio of 8:1:1 to form a homogenous slurry, which was casted onto carbon-coated aluminum foil with a doctor blade. The resulting electrodes were dried at 70 ˚C in vacuum for 4 h and then cut into pieces with a diameter of 14 mm.

Preparation of Li_2S_6 solution. 20 mM Li_2S_6 solution was prepared by mixing stoichiometric amounts of elemental sulfur (Sigma-Aldrich) and Li_2S (Alfa Aesar) in DOL: DME (Sigma-Aldrich, volume ratio 1:1). A homogenous dark-yellow solution of Li_2S_6 was obtained after stirring for 24 h at 130 ˚C.

7.3.2 Material characterizations. XRD measurements were performed on Rigaku MiniFlex instrument using the copper Kα radiation (λ = 1.54 Å). TGA was performed on a TA Instrument SDT Q600 employing a heating rate of 5 ˚C min^{-1} from 40 ˚C to 700 ˚C under airflow. SEM and TEM studies were conducted on a ZEISS Supra 40VP and Titan S/TEM, respectively. For XPS studies, the samples were sealed in a transporter in the glove box before being quickly transferred to the high-vacuum chamber of XPS (AXIS Ultra DLD) for analysis. All the spectra were fitted to Gaussian-Lorentzian functions and a Shirley-type background using CasaXPS software. The binding energy values were all calibrated using C 1s peak at 285.0 eV. All the EPR spectra were recorded at 5 K with a Bruker ELEXSYS E580 spectrometer. The microwave power and modulation amplitude were set to 2 mW and 20 G, respectively. Lithium-sulfur batteries were assembled within commercial EPR quartz tubes with an outer diameter of 5 mm and a length of 250 mm. Two electrodes are separated by > 15 mm, and only cathode is within the active cavity. *In situ* EPR cells were cycled at 0.3 mV s^{-1} and stopped at potentials of interest during discharging. Immediately, they were placed in liquid nitrogen to prevent further reactions.

7.3.3 Electrochemical characterizations. To evaluate the electrochemical performance, 2032-type coin cells (MTI Corporation) were assembled with polypropylene separator (Celgard 2500) and lithium foil (Alfa Aesar) as the anodes. 0.5 M LiTFSI (Sigma-Aldrich) and 2 wt-% $LiNO_3$ (Sigma-Aldrich) in DOL/DME was used as the electrolyte. Cyclic voltammetry analysis was performed on a Bio-Logic VMP3 electrochemical workstation with a three-electrode configuration. Lithium foils were used as both the counter electrode and the reference electrode. Galvanostatic charge-discharge measurements were carried out using Land CT2000 battery tester in a voltage range of 1.7-2.8 V for all rates. Specific capacities were calculated with respect to the mass of sulfur. EIS tests were carried out on a Solartron 1860/1287 Electrochemical Interface.

7.3.4 DFT calculations. The periodic structures including MnO_2, $Li_{0.5}MnO_2$, Nb_2O_5 and $Li_{1.0}Nb_2O_5$ are calculated with VASP. SCAN functional is used for describing the exchange-correlation interactions. It has been shown that SCAN functional is very accurate for the electronic structure of MnO_2, alkali intercalated MnO_2, and a wide range of materials[123-125]. The energy cutoff for plane waves is 400 eV. The density of k-mesh is large enough to make sure the energy difference is smaller than 0.01 eV/unit cell. HOMO/LUMO positions of isolated molecules including S_8, LiS_4, and LiS_3 radicals are calculated by Gaussian09 package in the level of B3LYP functional with 6-311++(d,p) basis sets.

Alignment of absolute band positions. We used a scheme to align the band edge positions (including VBM and CBM) of different materials with the vacuum energy:

$$E_i = \left[E_i^{bulk} - E_{ref}^{bulk}\right] + \left[E_{ref}^{slab} - E_{vac}^{slab}\right]$$

The first term calculates the difference between band edge energy E_i (which is either VBM or CBM) and a reference state E_{ref}. Here we use the energy of a semi-core orbital as the reference state. The second term calculates the difference between the reference state and vacuum energy in the slab model. The reference state is chosen as the semi-core orbitals because they are rarely influenced by their chemical environment. In this work, we choose the *4s* orbital of niobium atom, *3s* orbital of manganese atom, *1s* of lithium atom (for Li_2S_2 only) as the reference state, respectively. It should be notated that the energy of semi-core orbitals can be also influenced by the Madelung potential. If the adopting slab model is too thin, the Madelung potential will be different between bulk and thin slab. Therefore, we ensured the slab model has a sufficiently large thickness (larger than 35 Å) in all the calculations to minimize the difference of the Madelung potential at the center of the slab.

7.4 Electron transfers

The band edges of sulfur species and redox mediators are further aligned with respective to vacuum energy to illustrate the electron transfer pathways (Figure 7.4). Given that Nb_2O_5 presents lower conduction band positions than that of S_8 (-3.68 eV *vs.* -2.95 eV), electrons and lithium cations can be inserted into Nb_2O_5 upon discharge, generating $LiNb_2O_5$. Subsequently, the electrons in $LiNb_2O_5$ can be transferred to the conduction bands of S_8, LiS_4, and LiS_3 radicals, reducing them to Li_2S_2/Li_2S. The resulted Nb_2O_5 will be repetitively reduced to $LiNb_2O_5$ until all sulfur species are converted. Similarly, during charge process, electrons can be easily extracted from $Li_{0.5}MnO_2$, forming MnO_2. Since the conduction band of MnO_2 is lower than the valence bands of sulfur intermediates, electrons will flow from these sulfur species (Li_2S_2, LiS_3, LiS_4, Li_2S_n) to MnO_2. The redox between MnO_2 and $Li_{0.5}MnO_2$ continues until sulfur species are completely oxidized to S_8.

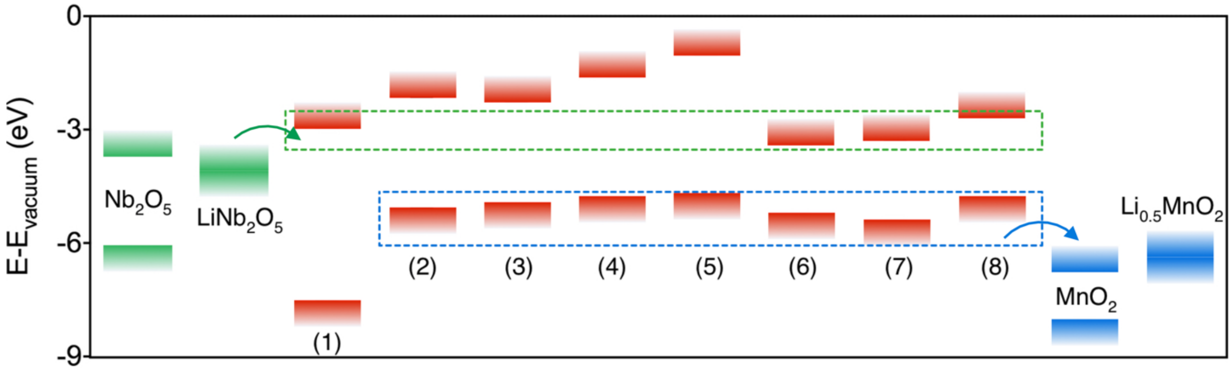

Figure 7.4 Electron transfer pathways in the sulfur cathode with the presence of mediators. (1) S_8, (2) Li_2S_7-4DOL, (3) Li_2S_6-4DOL, (4) Li_2S_5-4DOL, (5) Li_2S_4-4DOL, (6) LiS_4-DOL, (7) LiS_3-DOL and (8) Li_2S_2.

To probe into the process of electron transfer in sulfur cathodes, electron paramagnetic resonance (EPR) spectroscopy was employed for *in situ* analysis. Lithium-sulfur batteries were assembled within EPR tubes and cycled at 0.3 mV s^{-1} under room temperature. These cells were stopped at voltages of interest and placed in liquid nitrogen to prevent further reactions. Figure 7.5 a shows the EPR spectra of S-RGO electrode at different potentials (*vs.* Li^+/Li), illustrating the formation of sulfur radicals along cycling. RGO also exhibits a small broad peak at around 3350 Gauss (g = 2), which can be assigned to carbon radicals[126,127]. Given that Nb^{4+} (as in $LiNb_2O_5$) is EPR active while Nb^{5+} (as in Nb_2O_5) is EPR silent[128,129], S-Nb_2O_5 electrode was chosen as a representative electrode with redox mediators. As shown in Figure 7.5 b, the electrode not only exhibits the signals of sulfur radicals, but also shows a sharp peak at 3350 Gauss (g = 2), indicating the existence of $LiNb_2O_5$ during discharge.

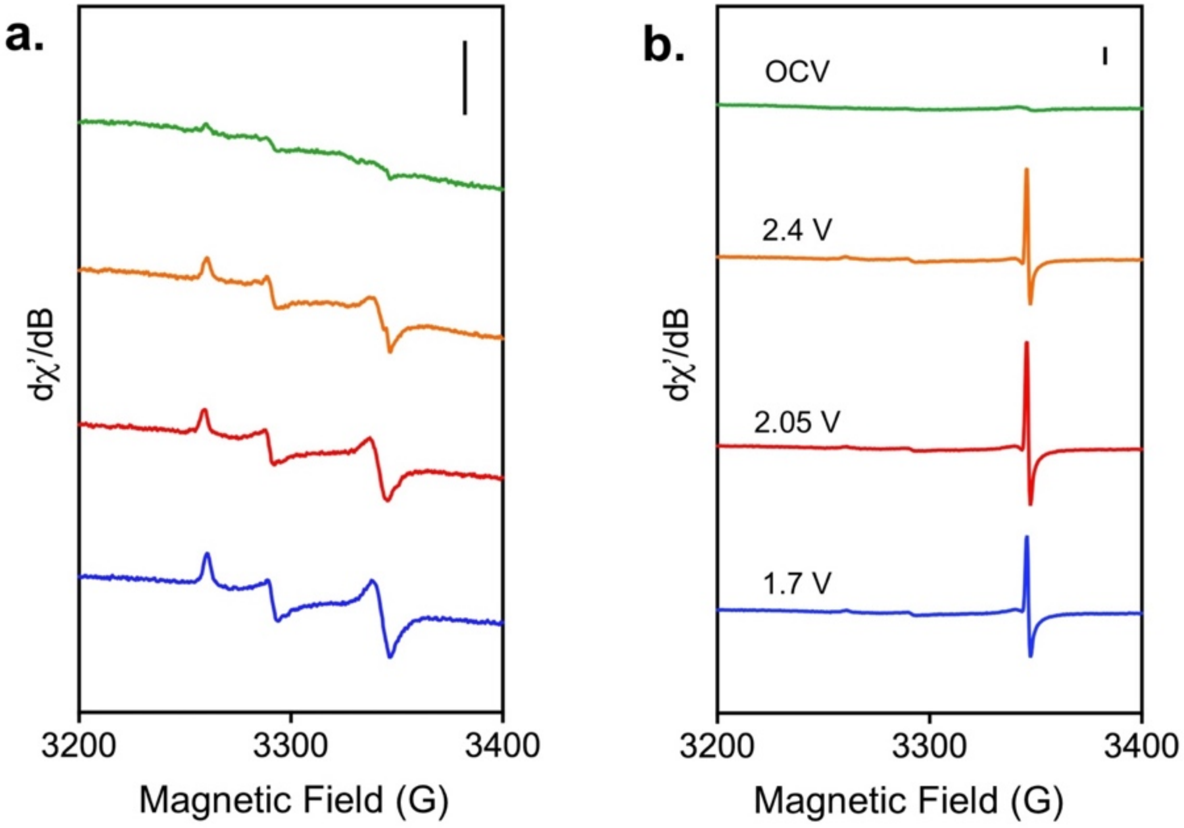

Figure 7.5 EPR spectrum of **b.** S-RGO electrode and **c.** S-Nb_2O_5 electrode at various potentials (*vs.* Li^+/Li). All the EPR spectra were recorded at 5 K. Scale bars are 1000 in **a.** and **b.**

Moreover, the direction of electron transfers between $LiNb_2O_5$ and sulfur species was investigated with X-ray photoelectron spectroscopy. Li_2S_6 solution was chosen as a representative composition of sulfur intermediates and mixed with $LiNb_2O_5$. The brown solution underwent apparent color change upon mixing (Figure 7.6). Meanwhile, the solid products were separated by centrifugation and dried in an argon-filled glove box.

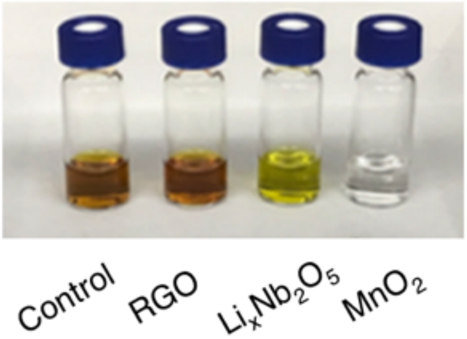

Figure 7.6 Digital photograph of Li_2S_6 solution before and after mixing with RGO, $LiNb_2O_5$, and MnO_2.

$LiNb_2O_5$, which is the discharged product of Nb_2O_5, is composed of 51.2% Nb^{5+} (206.7 eV, 209.5 eV) and 48.8% Nb^{4+} (203.4 eV, 206.1 eV)[130,131] (Figure 7.7 a). After mixing with the Li_2S_6 solution, the percentage of Nb^{4+} declines to 30% (Figure 7.7 b), suggesting the oxidation of Nb^{4+}. Correspondingly, the sulfur 2p spectrum illustrates the reduction of Li_2S_6 (Figure 7.7 c) and the generation of Li_2S_2 (161.7 eV) and Li_2S (160 eV)[106,132] (Figure 7.7 d). Besides, a small amount of thiosulfate groups (166.8 eV)[106,133] is also formed on the surface, which could serve as the active sites for electron transfers. Similar electron transfer process was also observed between Li_2S_6 and MnO_2 (Figure 7.8). The fast and reversible conversions of redox mediators between their oxidizing and reducing forms ($Nb_2O_5/LiNb_2O_5$ and $MnO_2/Li_{0.5}MnO_2$) ensure their mediation effects in sulfur cathode.

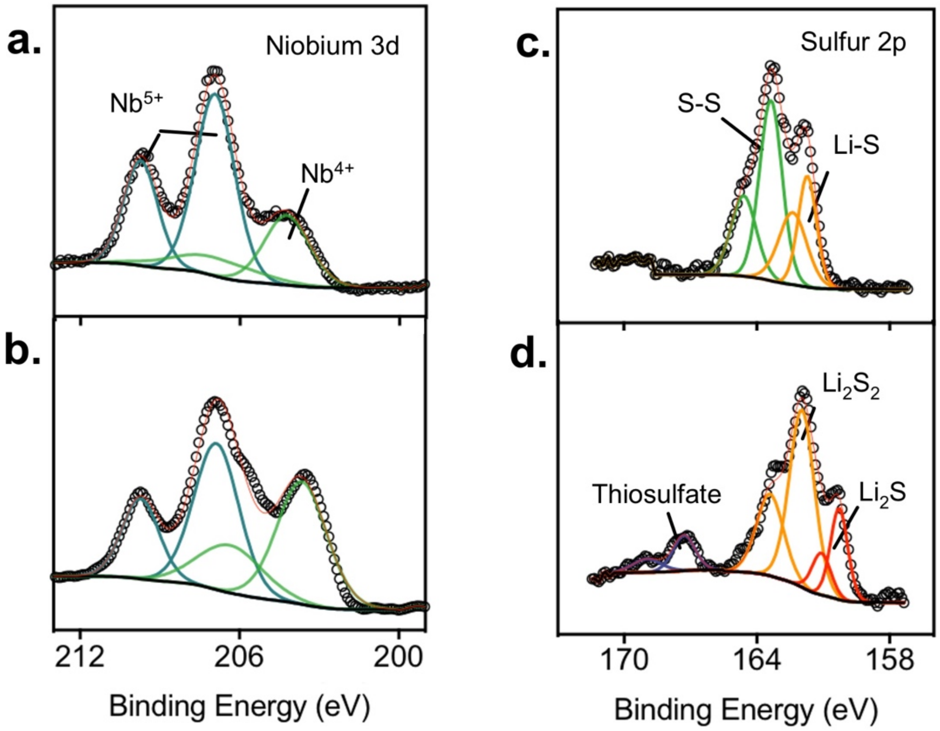

Figure 7.7 Niobium 3d spectrum of $LiNb_2O_5$ **d.** before and **e.** after mixing with Li_2S_6 solution. Sulfur 2p spectrum of **f.** Li_2S_6 and **g.** $LiNb_2O_5$-Li_2S_6 composites.

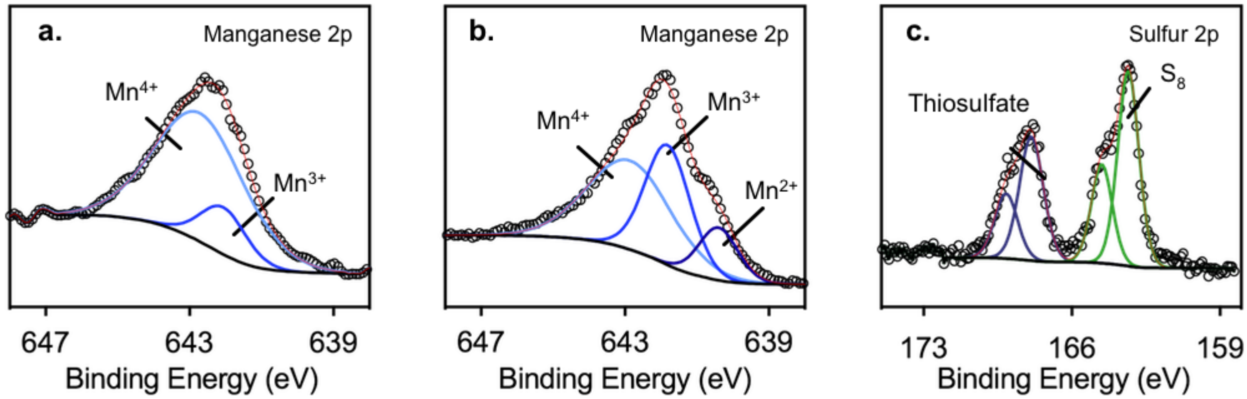

Figure 7.8 Manganese 2p spectrum of MnO_2 **a.** before and **b.** after mixing with Li_2S_6 solution. **c.** Sulfur 2p spectrum of MnO_2-Li_2S_6 composites.

7.5 Material characterizations

To evaluate the mediation effect of these oxides, we synthesized orthorhombic Nb_2O_5 and birnessite MnO_2 nanoparticles on reduced graphene oxides (RGO) using a hydrothermal method. As shown in Figure 7.9, the crystalline nanoparticles are homogeneously grown on RGO sheets. The d-spacings of Nb_2O_5 and MnO_2 nanoparticles are 0.395 nm and 0.24 nm, corresponding to (001) lattice plane of orthorhombic Nb_2O_5 and (100) lattice plane of birnessite MnO_2, respectively. Electrodes based on these composites were prepared using a slurry casting method. The weight percentages of oxides are around 10 % (Figure 7.10).

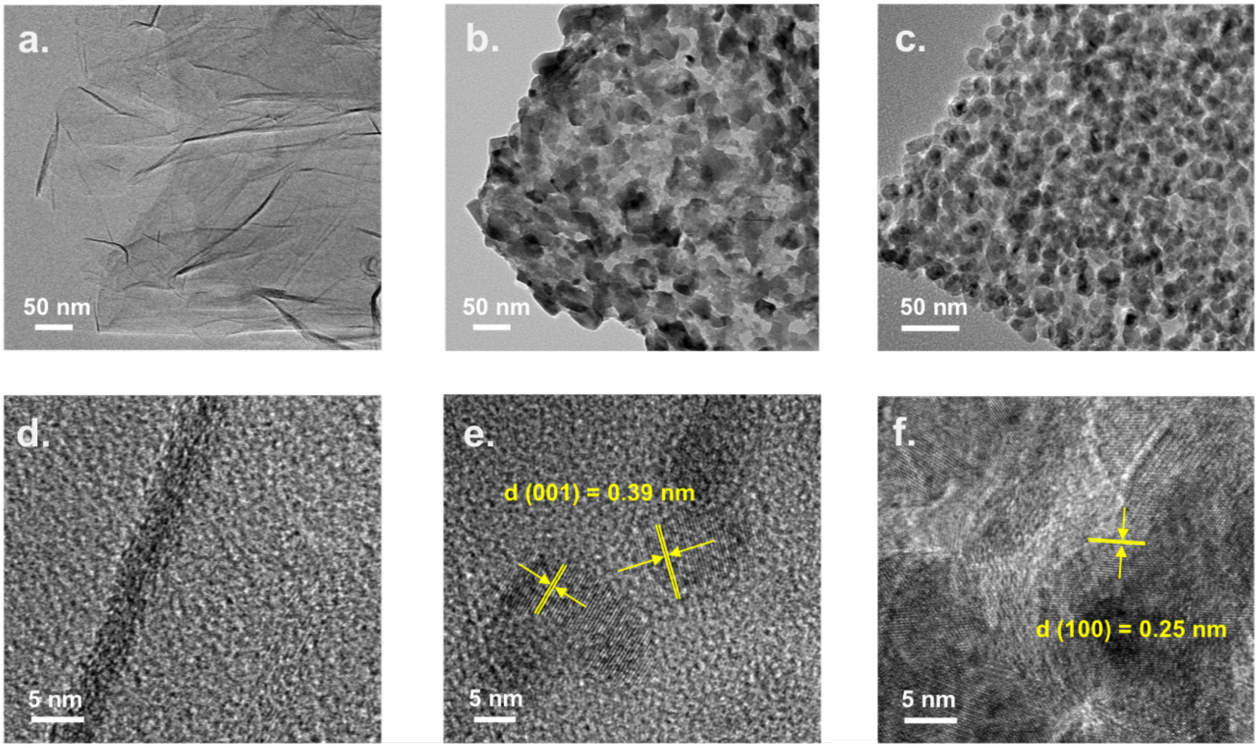

Figure 7.9 TEM images of **a.** RGO, **b.** RGO-Nb_2O_5, **c.** RGO-MnO_2 composites and the corresponding high-resolution TEM images of **d.** RGO, **e.** RGO-Nb_2O_5, **f.** RGO-MnO_2; Scale bars are 50 nm in TEM, and 5 nm in HRTEM.

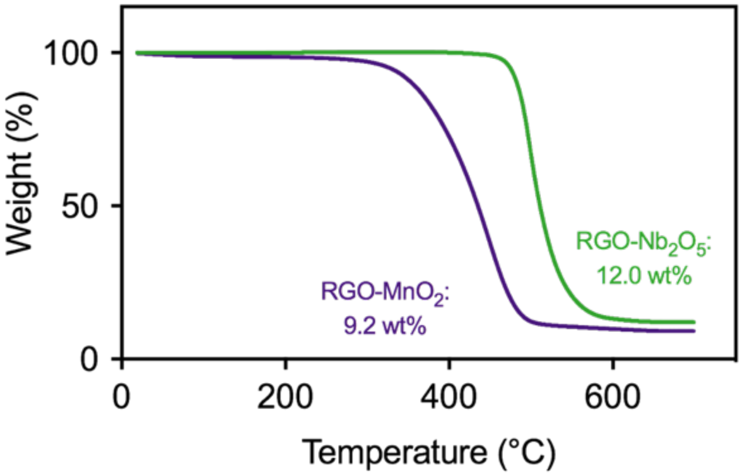

Figure 7.10 Thermogravimetric analysis of RGO-based composites.

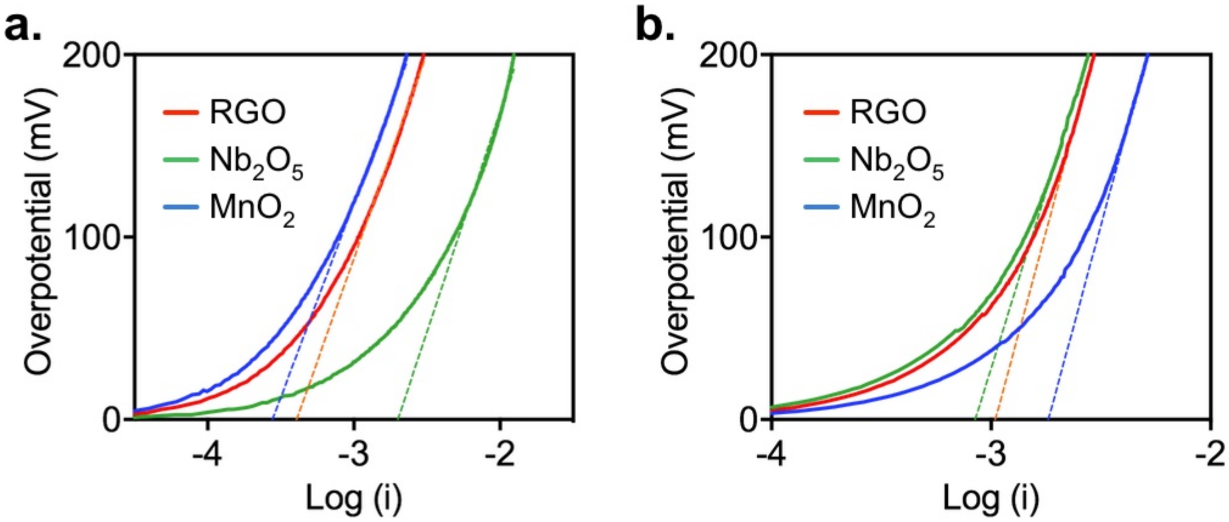

Figure 7.11 Tafel plot of RGO, Nb_2O_5, MnO_2 composites in 50 mM Li_2S_6 catholyte during **a.** cathodic scan and **b.** anodic scan.

The catalytic effects of these oxides are characterized using linear voltammetry with 50 mM Li_2S_6 solution as catholyte. According to the Butler-Volmer model, the standard rate constant (k^0) of an electrochemical reaction is proportional to its exchange current (i_0), which can be obtained from a Tafel plot. Figure 7.11 presents the Tafel plots of RGO, Nb_2O_5, MnO_2 during cathodic and anodic scans. These plots deviate sharply from linear behavior as the overpotential (η) approaches to zero, while the linear segments extrapolate to an interception of log i_0. As shown in Figure 7.11 a, Nb_2O_5 exhibits much higher exchange current comparing to that of RGO (2 mA *vs.* 0.41 mA), suggesting that the reduction of sulfur species on $Nb_2O_5/Li_xNb_2O_5$ nanoparticles is 3.9 times faster than that on RGO sheets. Although the incorporation of MnO_2 nanoparticles imposes a slight negative effect on sulfur reduction (0.28 mA), it significantly promotes the oxidation process of sulfur species. During anodic scans, the exchange currents of RGO, Nb_2O_5, MnO_2 are 1.0 mA, 0.85 mA and 1.82 mA, respectively (Figure 7.11 b). The oxidation of sulfur species is 82% faster on MnO_2/Li_yMnO_2 nanoparticles than that on RGO sheets. Therefore, $Nb_2O_5/Li_xNb_2O_5$ can promote the discharge process of sulfur species as a reductive mediator, while MnO_2/Li_yMnO_2 can assist the charge process as an oxidative mediator.

To form the sulfur/carbon composites, we infused elemental sulfur into these carbon-based materials, forming S-RGO, S-Nb_2O_5 and S-MnO_2 composites. Electrodes based on such composites were prepared using a slurry casting method. As shown in Figure 7.12, sulfur and niobium elements are homogeneously distributed in S-Nb_2O_5 electrode.

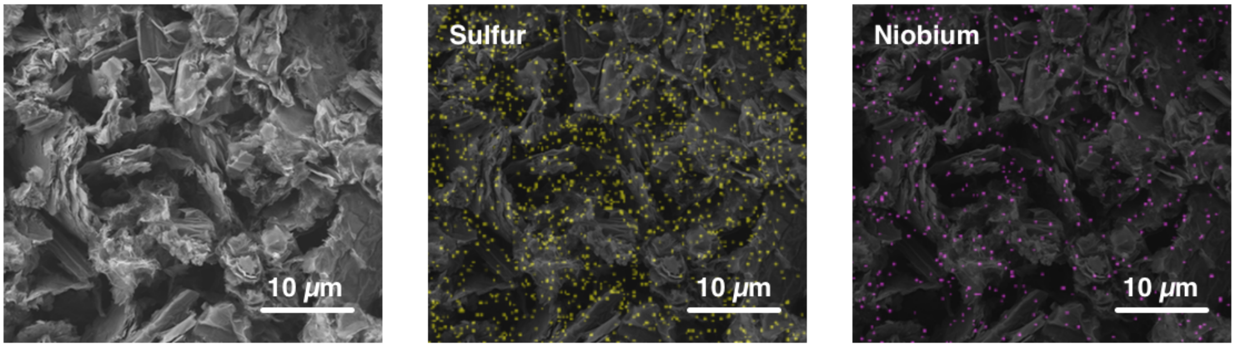

Figure 7.12 SEM and EDS images of electrode based on S-Nb_2O_5 composites, showing the homogenous distribution of sulfur and niobium elements.

7.6 Electrochemical characterizations

The electrochemical behaviors of these composites were examined with cyclic voltammetry (CV) at a scanning rate of 0.3 mV s^{-1} using three-electrode configuration (Figure 7.13 a). All three cathodes exhibit two cathodic peaks which can be attributed to the reduction of S_8 to sulfur intermediates ($i_p^{c,1}$) and their subsequent reduction to Li_2S_2/Li_2S ($i_p^{c,2}$). During the anodic sweep, there is one peak resulting from the conversion of Li_2S_2/Li_2S to sulfur intermediates and S_8 (i_p^a). The electrode without oxides shows much wider separation between cathodic and anodic peaks, whereas the ones with Nb_2O_5 or MnO_2 exhibit faster redox kinetics (Figure 7.13 b).

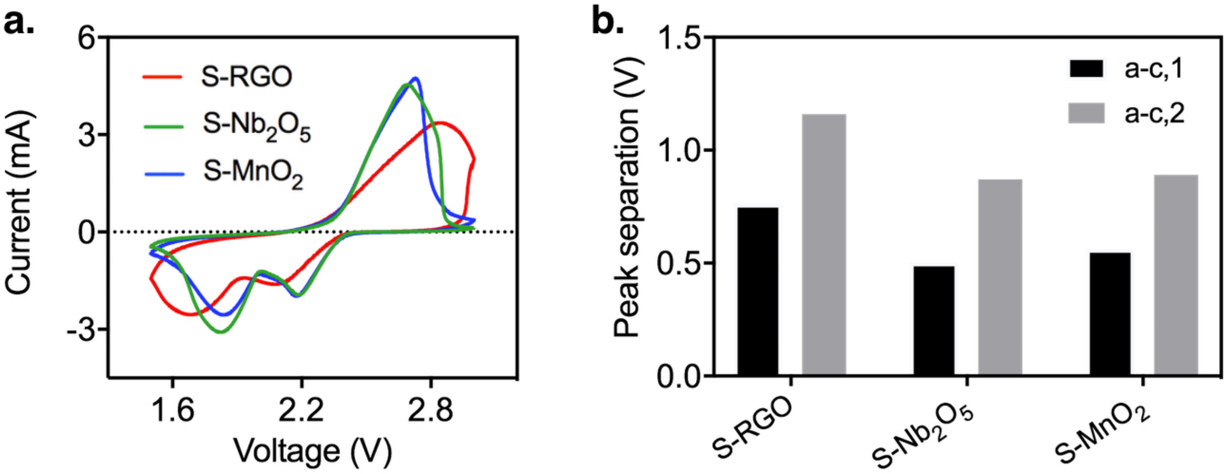

Figure 7.13 a. Cyclic voltammetry of sulfur cathodes at a scanning rate of 0.3 mV s^{-1}, showing accelerated electrochemical kinetics of sulfur electrodes after incorporating oxides as redox mediators. **b.** Redox peak separations of sulfur cathodes with/without oxides at 0.3 mV s^{-1}.

The electrochemical responses of these sulfur cathodes were further studied under different sweep rates, ranging from 0.1 mV s^{-1} to 0.5 mV s^{-1} (Figure 7.14 a). The redox peaks shift with increasing sweep rate, indicating a quasi-irreversible electrochemical process with slow electron transfer. As shown in Figure 7.14 b-d, all the cathodes exhibit a linear relationship between cathodic/anodic peak currents (i_p) and the square root of sweep rates (v). According to the classic

Randles-Šević equation, the slope of the curve ($i_p/v^{0.5}$) represents the square root of average diffusion coefficient of lithium polysulfides, which is correlated with their conversion rates under certain potentials. Figure 7.14 e summarizes the relative diffusion coefficient of sulfur species with/without oxides at different electrochemical steps. During the cathodic sweep, Nb_2O_5 and MnO_2 promote the conversion from S_8 to sulfur intermediates by 23% and 26.3%, respectively, whereas Nb_2O_5 also assists the formation of Li_2S_2/Li_2S. On the other hand, the addition of MnO_2 and Nb_2O_5 expedite the oxidation of sulfur species by 44.7% and 25%, respectively.

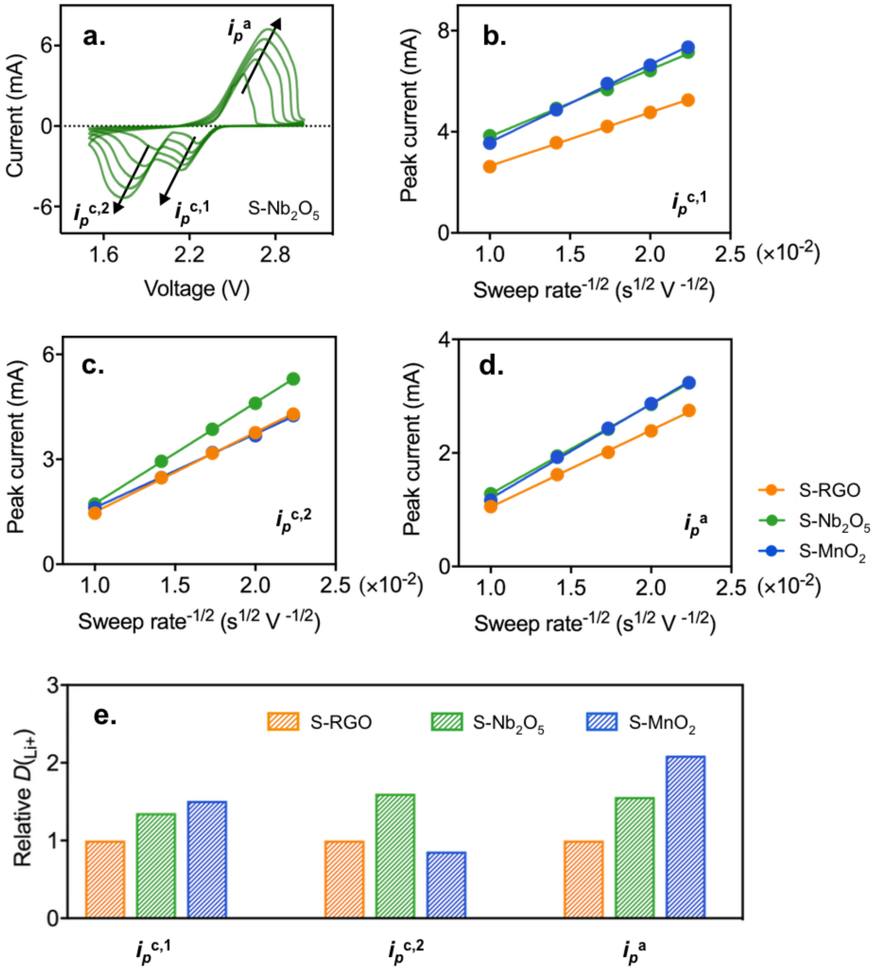

Figure 7.14 Electrochemical performance of sulfur cathodes with/without redox mediators. **a.** Cyclic voltammetry of a S-Nb_2O_5 electrode under different sweep rates, ranging from 0.1 mV

s^{-1} to 0.5 mV s^{-1}. **b-d.** Plots of cathodic and anodic peak currents *vs.* square root of sweep rates. **e.** Relative conversion rate of sulfur species during different electrochemical steps.

The volumetric energy density of lithium-sulfur battery is closely related to the mass loading of active materials in cathode, as well as their utilization rate[134]. Although a number of studies have shown enhanced redox kinetics by incorporating oxides/sulfides/nitrides/carbides with sulfur species, the majority of these studies focused on thin electrodes (mass loading (S) < 5 mg cm^{-2}). The improved electrochemical performances in such electrodes cannot be readily transformed into that in thick electrodes, which is required for practical applications. To achieve optimal redox kinetics and energy densities, we fabricated sulfur cathodes with both Nb_2O_5 and MnO_2 as dual redox mediators (denoted as S-Nb_2O_5-MnO_2). Here, the electrochemical behaviors of electrodes with high mass loadings (*i.e.*, 6 mg cm^{-2}) were systematically investigated.

S-Nb_2O_5-MnO_2 demonstrates excellent rate performance, delivering reversible capacities of 959, 848, 812, 753 and 692 mAh g^{-1}_{sulfur} under current densities of 0.5, 1.0, 2.0, 3.0 and 4.0 mA cm^{-2}_{areal}, respectively (Figure 7.15 a). In contrast, cathode without mediators exhibits capacities of 1030, 852, 765, 670 and 230 mAh g^{-1}_{sulfur} under same testing conditions. Figure 7.15 b further compares the representative voltage profiles of both electrodes at 0.2 C rate (1 C rate = 1675 mAh g^{-1}_{sulfur}), demonstrating reduced polarization (257 mV *vs*. 405 mV), as well as enhanced specific capacity (812 mAh g^{-1}_{sulfur} *vs.* 765 mAh g^{-1}_{sulfur}).

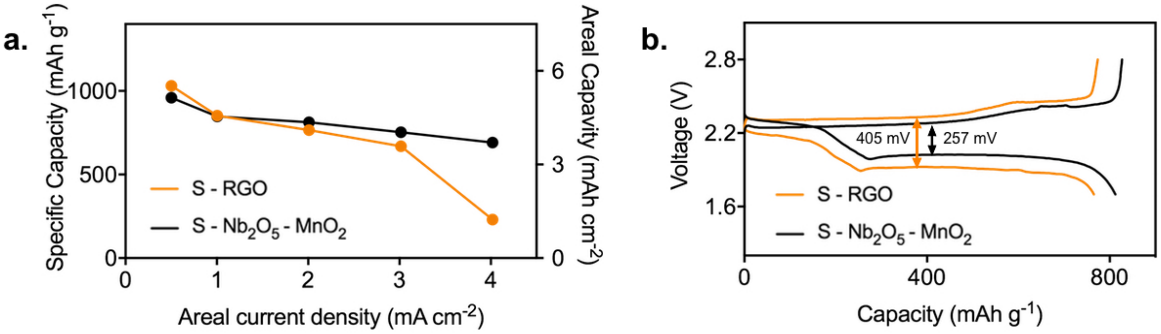

Figure 7.15 a. Comparison of the rate capability at various current densities. **b.** Representative voltage-capacity profiles of cells at high current densities (335 mA g^{-1}_{sulfur}, corresponding to 0.2 C rate).

Additionally, the interaction between sulfur species and oxides nanoparticles also constrains the outward diffusion of lithium polysulfides, resulting in suppressed self-discharge capacity loss by ~8% (Figure 7.16), as well as enhanced cycling stability. Comparing to S-RGO electrodes, the one with dual mediators exhibits better reversibility (0.47% *vs.* 0.67% per cycle) at 0.1 C rate (Figure 7.17 a). By lowering the depth of discharge, an areal capacity of 4.8 mAh cm^{-2}_{areal} is successfully maintained for 60 cycles with S-Nb_2O_5-MnO_2 electrode, whereas the S-RGO electrode experiences capacity deterioration after 32 cycles (Figure 1.17 b).

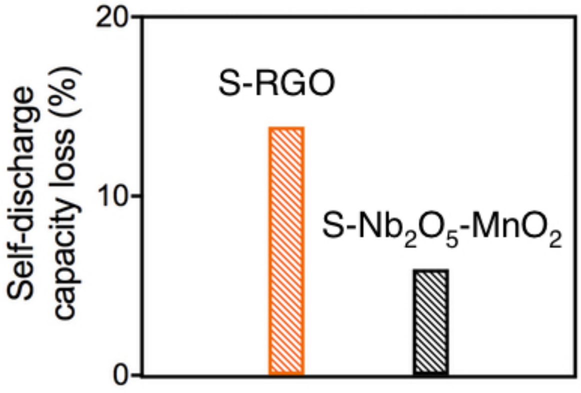

Figure 7.16 Self-discharge capacity loss of sulfur cathodes with/without dual mediators.

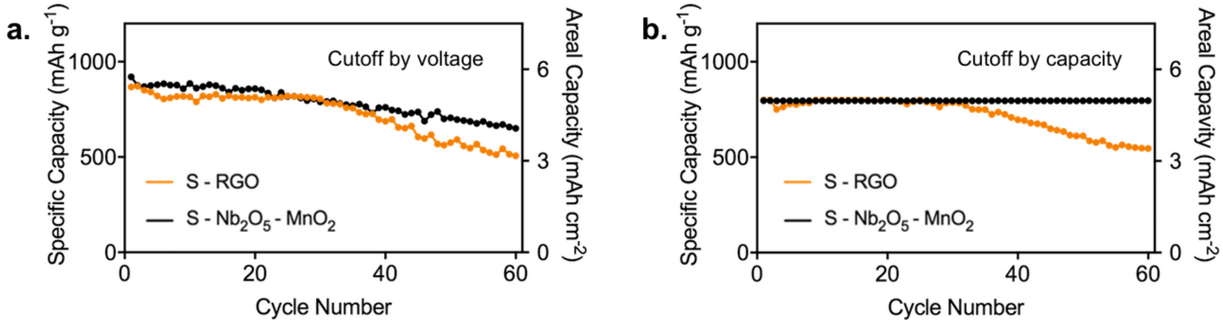

Figure 7.17 Galvanostatic cycling performance at 0.1 C rate under different discharge conditions **d.** Self-discharge capacity loss of sulfur cathode with/without dual mediators. **e.** discharge to 1.7 V and **f.** discharge to 800 mAh g^{-1}_{sulfur} or 1.7 V.

7.7 Conclusion

Pseudocapacitive materials Nb_2O_5 and MnO_2 have been systematically investigated as redox mediators for sulfur cathodes. By facilitating fast electron transfer through chemical reactions, these oxides dramatically improve the redox kinetics of electrodes with high sulfur loading. Theoretical calculations and experimental characterizations are combined to elucidate the redox mediation process. Future studies can be extended to tuning the electronic structures and working windows of various potential mediators, such as heteroatom-doped carbon materials, metal sulfides/nitride/carbides, metal organic frameworks and *etc.*, leading to the rational design of high energy battery systems.

Chapter 8 Hybrid Silicate Coatings for Lithium Metal Anodes

8.1 Introduction

To circumvent the spontaneous reactions between metallic lithium and electrolyte components, researchers have exploited a number of solid materials as solid electrolytes or coatings for lithium metal anode (LMA). These materials can be categorized into four groups: inorganic, polymeric, hybrid organic/inorganic and carbonaceous materials. Inorganic Li^+ conductors, represented by lithium superionic conductor (LISICON), tend to form point contacts with LMA due to their rigidity, resulting in large interfacial resistance.[39,54,55] Although ceramic materials with Li^+ conductivity exceeding 1×10^{-3} S cm^{-1} have been developed, such materials (*e.g.* $Li_{10}GeP_2S_{12}$ and $Li_{1.3}Al_{0.3}Ti_{1.7}(PO_4)_3$) are unstable in the presence of metallic lithium[56,57]. Electrochemically inert lithium phosphorous oxynitride (LiPON)[58] and Al_2O_3[59] have been deposited on LMA using a sputtering and an atomic layer deposition technique, respectively; however, the area of the coatings is limited (*e.g.*, < 5 cm^2). Polymeric materials, which offer the ease of processing, present insufficient modulus to inhibit dendritic formation.[60-62] Hybrid organic/inorganic layers, which combine the merits of organic and inorganic materials, have been subsequently deposited onto LMA and demonstrated successful suppression of dendrite formation at a high current density (*e.g.* 2 mA cm^{-2}).[63] Coatings of carbon nanospheres[64] and carbon film[65] have also been transferred onto LMA to facilitate the formation of stable SEI, whereas it is still difficult to implement such coatings during battery fabrication.

In this chapter, we designed and fabricated conformal coatings of organic-inorganic hybrid silicate for LMA by a vapor deposition process. As shown in Figure 8.1, lithium foil is generally covered by a skin layer of Li_2O and LiOH. When lithium foil is exposed to the vapor of 3-mercaptopropyl trimethoxysilane (MPS) and tetraethoxysilane (TEOS), Li_2O can react with the mercapto groups (-SH) from MPS, forming -S^--Li^+ bonds (Reactions I). Meanwhile, the moieties of methoxysilane (-Si-OCH_3, from MPS) and ethoxysilane (-Si-OCH_2CH_3, from TEOS) can undergo hydrolysis and condensation reactions, forming a thin layer of lithium silicate (Li_xSiO_y) (Reaction II).

Such thin and compact organic-inorganic coatings possess a “hard” inorganic moiety (Li_xSiO_y) to block the growth of lithium dendrites and a “soft” organic moiety (mercaptopropyl groups) to enhance the flexibility and robustness. More importantly, Li_xSiO_y can serve as a Li^+ conductor to facilitate Li^+ transportation through the electrode/electrolyte interphase, while the S^-/Li^+ bonds between the coatings and the metallic lithium improves the adhesion of the coatings to the metal substrate.

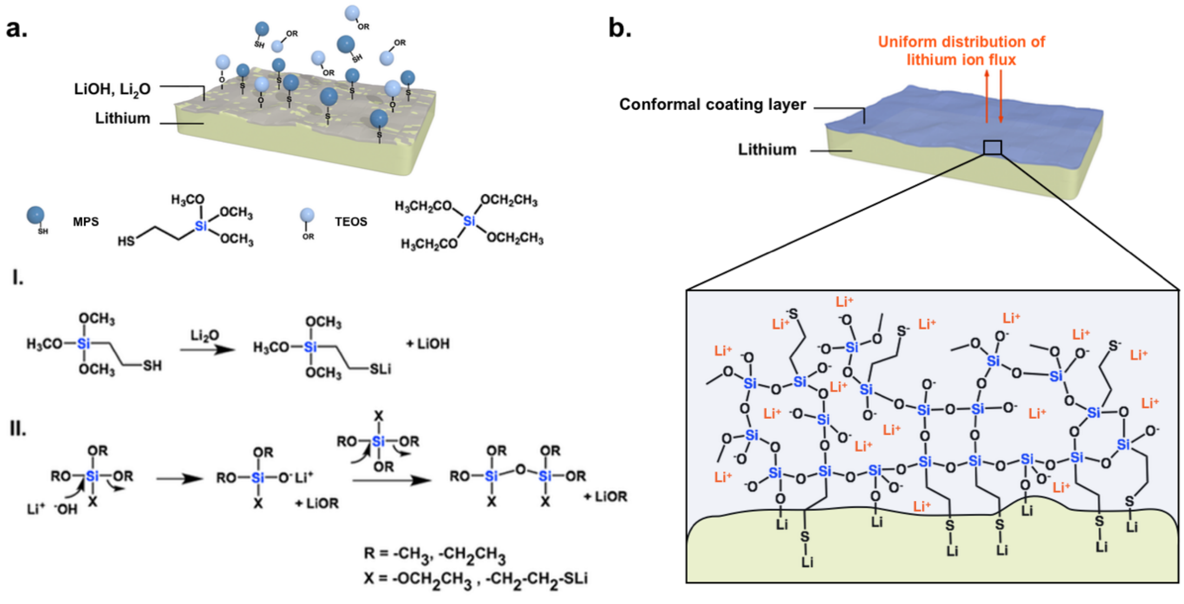
a.
LiOH, Li₂O
Lithium
MPS
TEOS
I.
Li₂O
+ LiOH
II.
+ LiOR
R = -CH₃, -CH₂CH₃
X = -OCH₂CH₃ , -CH₂-CH₂-SLi
b.
Uniform distribution of lithium ion flux
Conformal coating layer
Lithium

Figure 8.1 Illustration of the formation of an organic-inorganic coating on LMA. **a.** Reactions of methoxysilane and ethoxysilane catalyzed by LiOH; **b.** Formation of an organic-inorganic coating layer on LMA.

8.2 Methods

8.2.1 Fabrication of coated lithium metal anode. Lithium chips were exposed to the mixed vapor of 3-mercaptopropyl trimethoxysilane (MPS) and tetraethoxysilane (TEOS) at 100 ˚C and ambient pressure for 8 h, followed by heat treatment at 120 ˚C for 30 min. The volume ratio of MPS and TEOS in the precursor is 1:1. For thicker coating layer, the lithium chips can be pre-treated with O_2 for 1 h.

8.2.2 Preparation of cathodes. Both lithium iron phosphate and sulfur cathodes were prepared using a slurry casting method. Active materials ($LiFePO_4$ or sulfur), carbon black and polyvinylidene fluoride (PVDF) were mixed with a weight ratio of 8:1:1 to form a homogenous slurry with N-methyl-2-pyrrolidone, then cast onto aluminum foil (lithium iron phosphate cathodes) or carbon-coated aluminum foil (sulfur cathodes) with a doctor blade. All the electrodes were dried at 70 ˚C for 12 h. The mass loadings for $LiFePO_4$ and sulfur are 5 mg cm^{-2} and 2 mg cm^{-2}, respectively. For Li-$LiFePO_4$ cell, the current density and areal capacity are around 0.85 mA cm^{-2} and 0.65 mAh cm^{-2} for LMAs, respectively. For Li-S cell, the current density and areal capacities are around 1 mA cm^{-2} and 2.15 mAh cm^{-2} for LMAs, respectively.

8.2.3 Material characterization methods. SEM studies were conducted on a ZEISS Supra 40VP SEM. Samples were transferred from an argon atmosphere to vacuum chamber of SEM in less than 1 min. For XPS studies, the samples were sealed in a transporter in the glove box before being quickly transferred to the high-vacuum chamber of XPS (AXIS Ultra DLD) for analysis. All the spectra were fitted to Gaussian-Lorentzian functions and a linear-type background using CasaXPS software. The binding energy values were all calibrated using C 1s peak at 284.5 eV.

8.2.4 Electrochemical characterization methods. To evaluate the electrochemical performance, 2032-type coin cells (MTI Corporation) were assembled with Celgard PP separators for all cells.

1 M lithium hexafluorophosphate ($LiPF_6$) in ethylene carbonate/diethyl carbonate (EC/DEC, *v*:*v*= 1:1) was used as electrolyte for Li-$LiFePO_4$ cells, while 1 M LiTFSI with 1 wt% $LiNO_3$ in 1,3-dioxolane/1,2-dimethoxyethane (DOL/DME, *v*:*v* = 1:1) was used as electrolyte for Li-S cells. Galvanostatic charge-discharge measurements were carried out using Land CT2000 battery testers. The voltage windows for Li-$LiFePO_4$ and Li-S cells are 2.4 - 4 V and 1.7 - 2.8 V, respectively. Specific capacities were calculated with respect to the mass of lithium iron phosphate or sulfur.

8.3 Material characterizations

The morphology of the coated LMA was characterized by scanning electron microscopy (SEM), showing significantly reduced the roughness of the lithium surface after the coating process (Figure 8.2 a, b). No noticeable crack or defect can be observed on the coated LMA. Elemental mapping images achieved by energy-dispersive x-ray spectroscopy (EDX) reveal the homogenous distribution of silicon and sulfur, verifying the formation of uniform coatings (Figure 8.2 c, d).

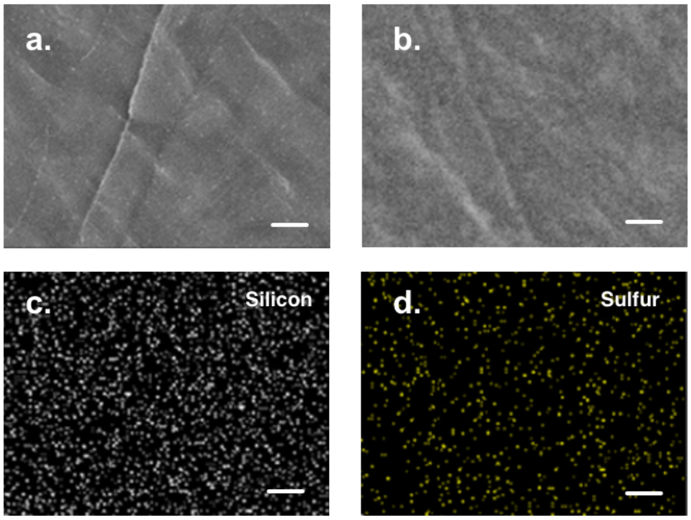

Figure 8.2 Characterizations of the inorganic-organic coatings. SEM images of a lithium foil **a.** before and **b.** after the vapor deposition. Elemental mapping of the coatings shows the uniform distribution of **c.** silicon and **d.** sulfur. Scale bars are 2 µm in a, b and 10 µm in c, d.

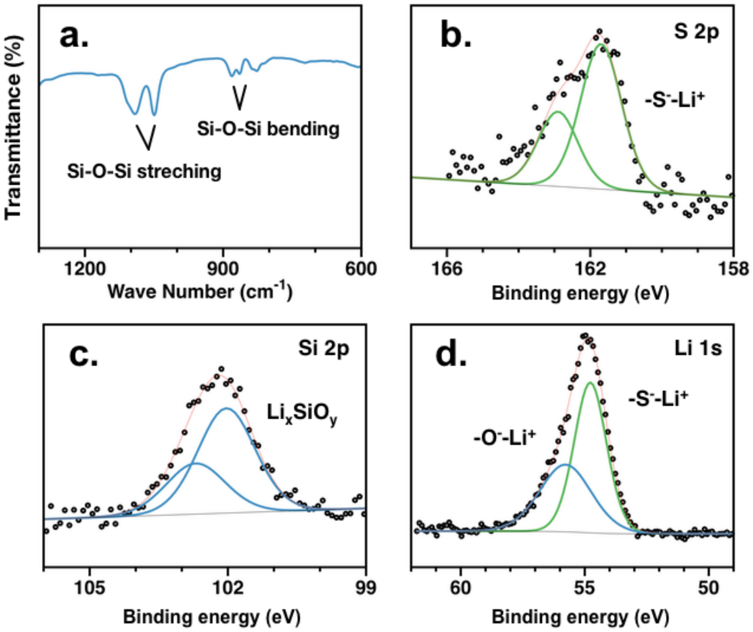

Figure 8.3 Characterizations of the inorganic-organic coatings. **a.** FTIR spectra of the coatings, indicating the formation of Si-O-Si bonds. XPS analysis of a coating layer for **b.** silicon 2p and **c.** sulfur 2p and **d.** lithium 1s, respectively.

Fourier transform infrared (FTIR) spectrum of the coating exhibits Si-O-Si stretching at 1092 cm^{-1} and 1049 cm^{-1}, as well as its bending at 880 cm^{-1} and 864 cm^{-1},[135] confirm the formation of silicate coatings (Figure 8.3 a). In addition, x-ray photoelectron spectroscopy (XPS) reveals a typical 2p$_{3/2}$ spectrum of silicon at 101.6 eV[136, 137], consistent with the formation of lithium silicate (Li$_x$SiO$_y$) (Figure 8.3 b). A typical spectrum of sulfur displays a binding state at 161.3 eV[106], in accordance with the formation of -S$^-$-Li$^+$ bonds (Figure 8.3 c). Consistently, lithium 1s spectrum shows two binding states at 54.6 eV and 55.6 eV[138], which are attributed to -S$^-$-Li$^+$ bonds and -O$^-$-Li$^+$ bonds, respectively (Figure 8.3 d). No metallic lithium (Li^0) peaks (~ 53.4 eV[137]) can be detected, indicating a complete coverage of the metal surface. Such coatings with Si-O-Si backbones and Si-C/Si-O-Li side groups are expected to possess high chemical stability and mechanical strength.

The thickness of the coatings was estimated with XPS depth profiling. The intensity of silicon 2p signal decreased gradually with ion gun etching. After 3 min, the coating layer was completely removed. Based on the etching rate of 8.1 nm/min, the thickness is estimated as 24 nm (Figure 8.4).

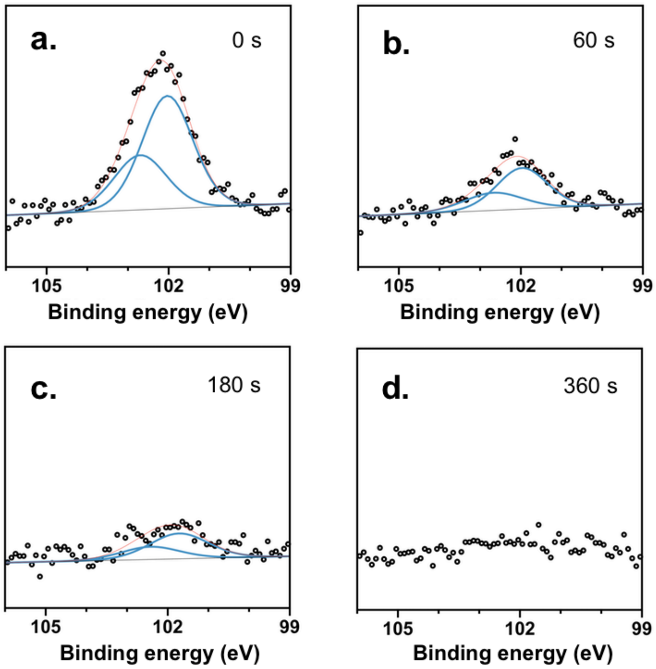

Figure 8.4 XPS depth profiling of coatings on LMA. Silicon 2p spectrum after etching for **a.** 0 s, **b.** 60 s, **c.** 180 s and **d.** 360 s, respectively.

The electronic resistivity of the coating layer was characterized using direct current-voltage measurement. LMAs were sandwiched between two stainless steel (SS) blocking electrodes and subjected to a direct current of 5 mA. The electrical resistivity (ρ) of the coating layer can be calculated with equation $\rho = \frac{R \cdot S}{L} = \frac{U \cdot S}{I \cdot L}$, where L is the thickness of the coating layer, I is the applied current, S is the area of the lithium chips and U is the average voltage response. The electronic resistivity of the coating layer is calculated as $2.29 * 10^{14}\ \Omega \cdot cm$, which is electronically insulated (Figure 8.5).

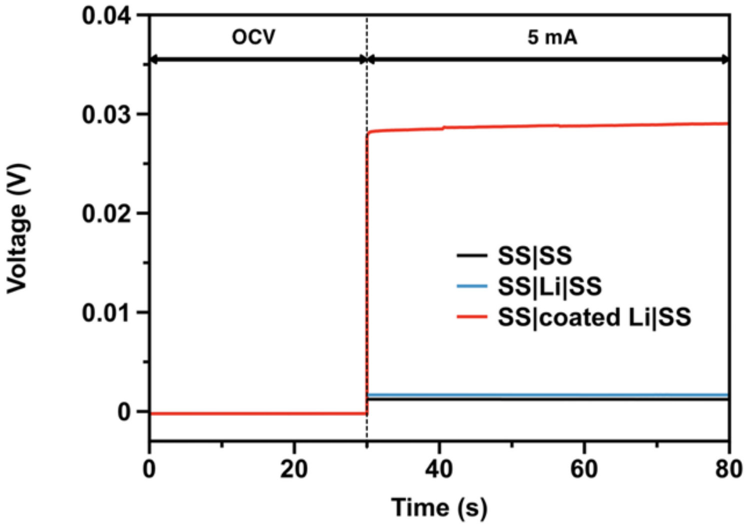

Figure 8.5 Comparison of the current response of the coated and uncoated LMAs.

To verify the sealing of lithium surface by the coating layers, we exposed an uncoated and a coated lithium foil to atmosphere of 25 ˚C and 50 % humidity. Figure 8.6 exhibits the photographs of the lithium foils after exposure for different time periods. The uncoated lithium foil tarnishes immediately after exposing to air (< 2 min), while the coated lithium foil can visually maintain unchanged in 4 h after exposure.

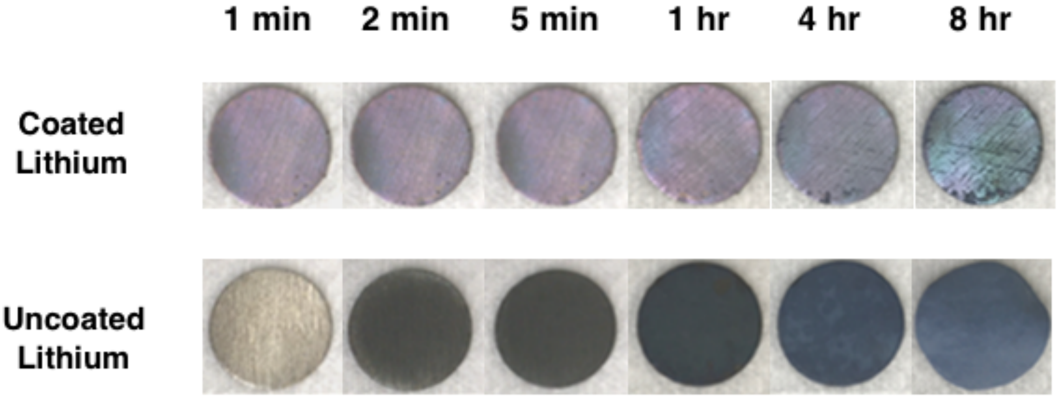

Figure 8.6 Digital images of an uncoated and a coated lithium foil exposed to air at 25 ˚C and 50 % humidity.

8.4 Electrochemical behaviors and morphological changes

Symmetric cell configuration is employed to evaluate the electrochemical stability of the LMAs. The electrochemical impedance spectroscopy of the resulted symmetric cells shows similar charge transfer resistance for the uncoated and coated LMAs (Figure 8.7).

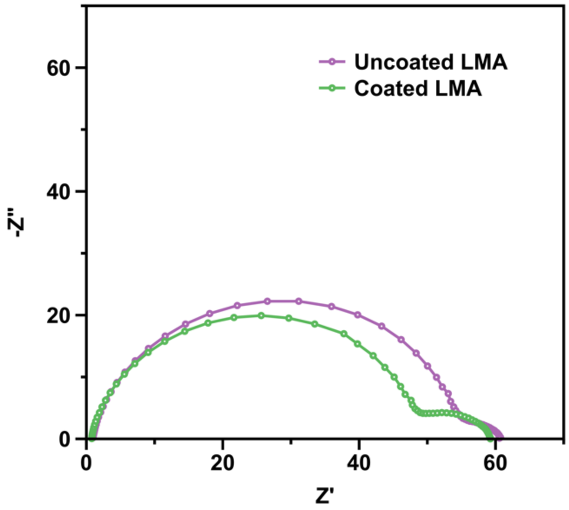

Figure 8.7 Nyquist plots showing similar charge transfer resistance for symmetric cells of uncoated and coated LMAs.

Furthermore, lithium plating/stripping tests was first conducted in carbonate-based electrolyte, i.e., 1M $LiPF_6$ in ethylene carbonate (EC)/diethyl carbonate (DEC) (v:v = 1:1), a representative electrolyte for commercial lithium-ion batteries (Figure 8.8). Under a current density of 0.5 mA cm^{-2} (2 h for each plating or stripping period with an areal capacity of 1.0 mAh cm^{-2}), the uncoated electrode shows rapidly increased and fluctuated overpotential due to the reactions between the lithium and the electrolyte. In contrast, the coated electrode presents an initial overpotential of 45 mV, which is maintained for 500 h (corresponding to 125 cycles of lithium plating/stripping). Such behavior indicates a stable interface between the coated LMA and the carbonate-based electrolyte.

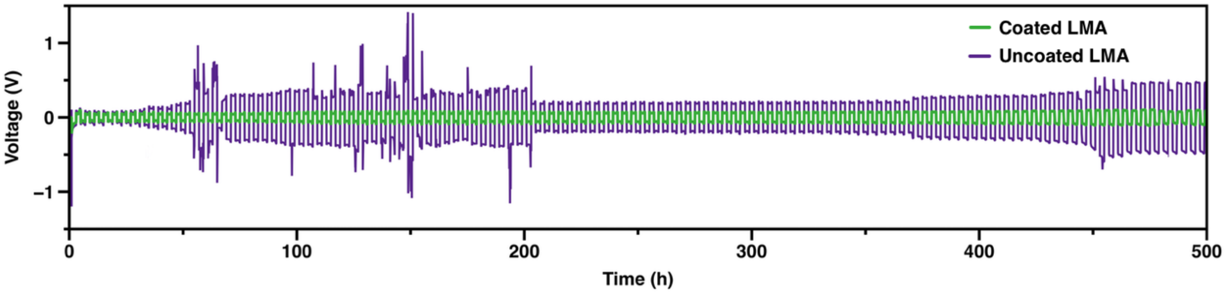

Figure 8.8 Voltage profiles of symmetric lithium cells at 0.5 mA cm^{-2} in a carbonate-based electrolyte.

The morphological changes of the uncoated and coated electrodes were probed with SEM. After 50 cycles (corresponding to 100 h), the surface of the uncoated LMA becomes porous with submicron-sized dendritic structure (Figure 8.9 a, b). Such high-surface-area electrode can lead to excessive formation of SEI, consuming both the lithium and electrolyte. In addition, detachment of such dendritic structures from the electrode may occur during lithium stripping, further deteriorating the electrode performance. In contrast, the coated LMA maintains a smooth surface after the cycling process without forming any pits or dendritic structures (Figure 8.9 c).

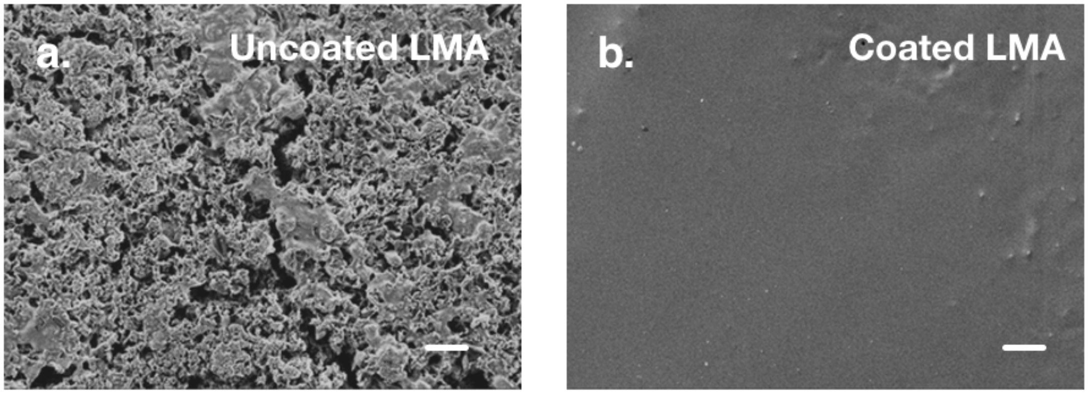

Figure 8.9 SEM images of **a.** uncoated and **b.** coated LMAs after cycling for 100 h. Scale bars are 10 µm.

It is important to point out that the coatings made by MPS/TEOS alone or other volumetric ratios of MPS and TEOS fail to prevent the dendritic formation (Figure 8.10). A MPS molecule contains three methoxysilane groups and one mercaptopropyl group, while a TEOS molecule contains four ethoxysilane groups. The use of MPS leads to the formation of silicate coating with a lower degree of condensation reaction and lower modulus. On the other hand, the use of TEOS leads to the formation of silicate coatings without the adhesive mercapto groups; as-formed coatings may be easily detached from the electrode. The balancing between MPS and TEOS leads to the formation of robust coatings with suitable mechanical strength and adhesion to the anodes, resulting in the stable electrochemical behaviors.

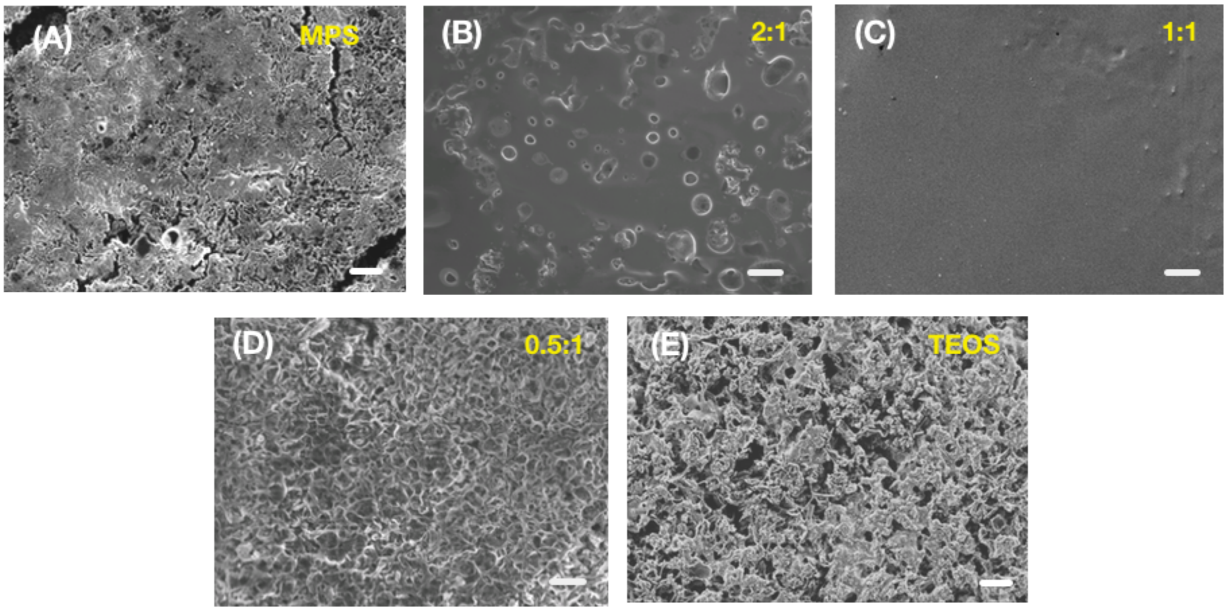

Figure 8.10 SEM images of coated LMA with the different volumetric ratio between MPS and TEOS **a**. 1:0, **b.** 2:1, **c.** 1:1, **d.** 0.5:1, **e.** 0:1. All the LMAs were cycled in symmetric cells for 100 h (50 cycles) under a current density of 0.5 mA cm^{-2} with an area capacity of 1 mAh cm^{-2}. Scale bars are 10 μm.

In lithium-sulfur battery, ether-based electrolytes are commonly used to replace the carbonate-based one due to the irreversible reactions between polysulfides and carbonates.[139] To evaluate the feasibility of using such coated LMA in lithium-sulfur cells, similar lithium plating/stripping experiments were performed with 1M lithium bis(trifluoromethanesulfonyl) (LiTFSI) in 1,3-dioxolane (DOL)/dimethoxyethane (DME) (*v*:*v*=1:1). Although exhibiting less severe degradation than that in the carbonate-based electrolyte, the uncoated LMA experiences a gradual evolution of overpotential from 26.5 mV to 757 mV during the first 900 h; afterward, the overpotential rapidly increases and fluctuates (Figure 8.11). In contrast, the coated LMA shows excellent electrochemical stability with a negligible increase in overpotential from 17 mV to 31 mV after 1000 h.

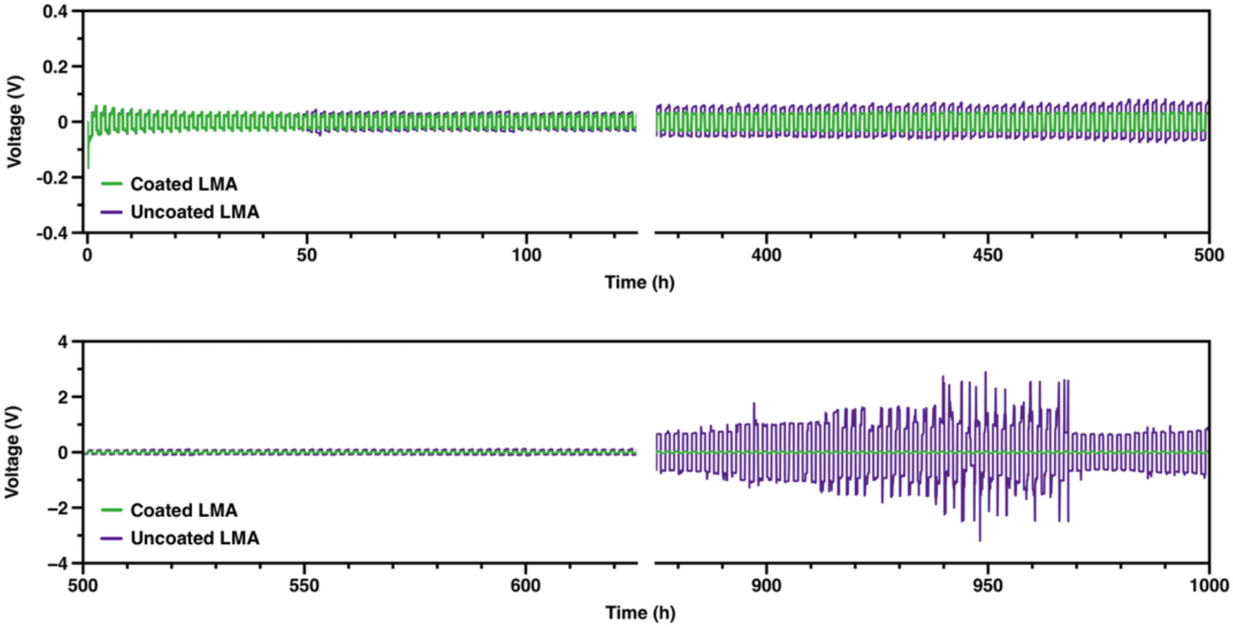

Figure 8.11 Voltage profiles of symmetric lithium cells at 0.5 mA cm^{-2} in LiTFSI (1 M) in DOL/DME (*v*:*v* = 1:1).

Similarly, the morphology of LMA was probed with SEM. As shown in Figure 8.12 a, the surface of the uncoated LMA becomes rough with rod-like structures, while that of the coated LMA is maintained smooth and intact with a grain size of around 2 µm (Figure 8.12 b, c).

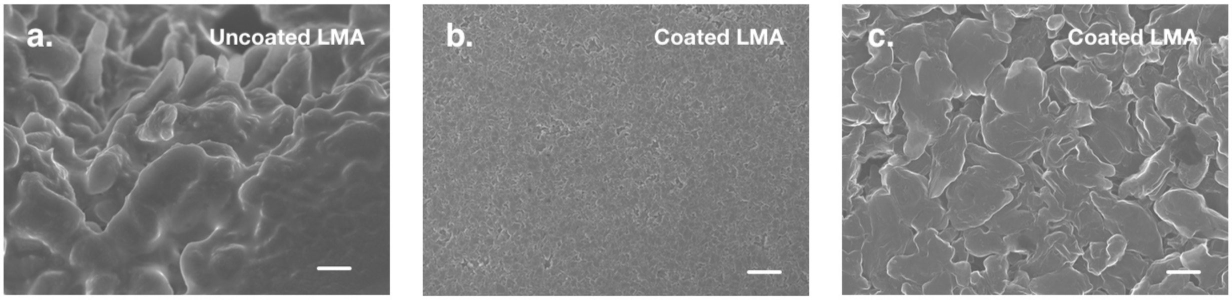

Figure 8.12 SEM images of **a.** uncoated and **b.** coated LMAs after cycling for 200 h. Scale bars are 10 µm in (**a**, **b**) and 1 µm in **c**.

The thickness of the coating layer could affect both mechanical stability and electrochemical performance of the cells. With a short deposition time (*e.g.* 4 h), the as-formed coating layer is not uniform (Figure 8.13) with an average thickness around 10 nm. The coating becomes homogeneous after 8 h deposition with a thickness of 24 nm. Under a current density of 2 mA cm^{-2}, the 10 nm-coated LMA experiences a gradual evolution of overpotential during the first 110 h; afterward, the overpotential rapidly increases and fluctuates (Figure 8.14). In contrast, the 24 nm-coated LMA shows excellent electrochemical stability for more than 200 cycles, successfully suppressing the formation of lithium dendrites and the side-reactions between lithium and electrolyte. Therefore, to achieve a satisfactory electrochemical performance, especially under high current densities, the thickness of the homogenous coating layer should be at least 20 nm.

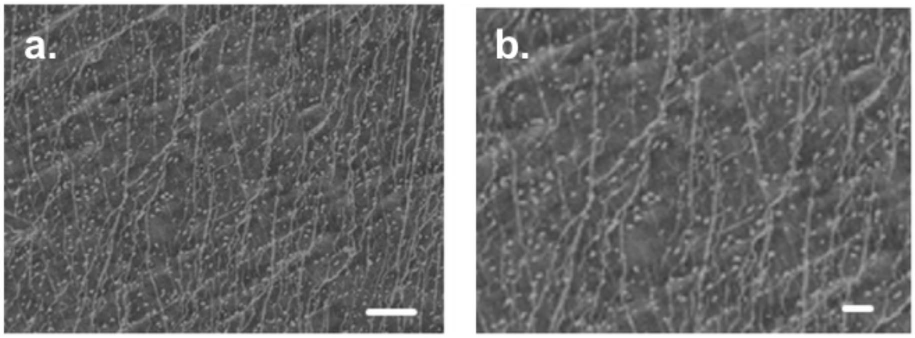

Figure 8.13 SEM images of coated LMAs with a deposition time of 4 h under different magnifications. Scale bars are 10 μm in (A) and 2 μm in (B).

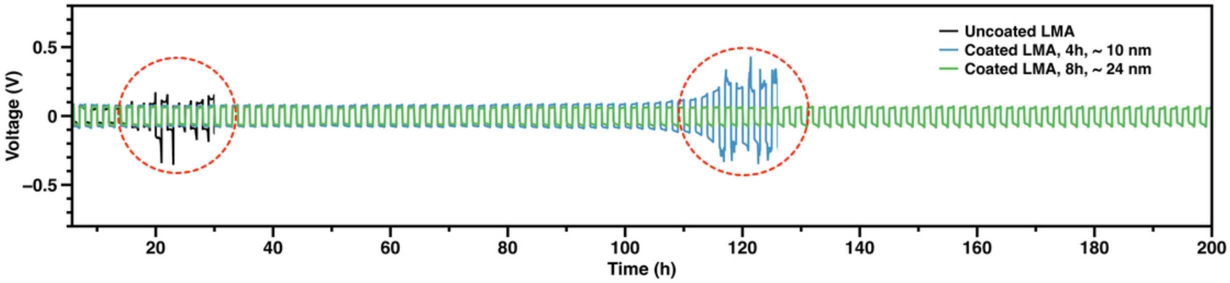

Figure 8.14 Voltage profiles of symmetric lithium cells at 2 mA cm^{-2} with an areal capacity of 2.0 mAh cm^{-2} in LiTFSI (1 M) in DOL/DME (v:v = 1:1).

Although thicker coatings may provide better mechanical stability, it may also lead to increased resistance. Table 4.1 compares the thickness of the coating layers with resistance and the resulted IR drops. For example, under a current density of 2 mA cm^{-2}, the IR drop from the anode can be as high as 0.45 V for 1 μm-coated LMAs, which will significantly impede the fast charging/discharging behavior of the cells.

Table 8.1 Comparison of the thickness of the coating layer, the resistance and the IR drop at a current density of 2 mA cm^{-2}. Assuming the diameter of the electrodes is 1.56 cm.

Thickness	**Resistance (ohms)**	**IR drop at 2 mA cm^2 (V)**
10 nm	0.1	0.0004
24 nm (this work)	2.8	0.01
100 nm	11.7	0.04
250 nm	29.2	0.11
0.5 μm	58.3	0.22
1 μm	116.7	0.45
2 μm	233.3	0.89

Replacing the graphite anodes in conventional lithium-ion batteries with LMA would dramatically increase their energy density. As a proof-of-concept, Li-$LiFePO_4$ cells were constructed and cycled at 0.5 C rate (1 C = 170 mAh g^{-1}). With a protective coating on the LMA, Li-$LiFePO_4$ cell exhibits improved electrochemical kinetics and decreased polarization, evidenced by the voltage difference between charge and discharge plateaus (374 mV *vs.* 268 mV) and an increased initial capacity (137.9 mAh g^{-1} *vs.* 124.9 mAh g^{-1}) (Figure 8.15a). After 500 cycles, the cell with a coated LMA exhibits a reversible capacity of 103.6 mAh g^{-1} and an average coulombic efficiency of 99.87%, while the cell with an uncoated LMA suffers from rapid deterioration after 200 cycles (Figure 8.15b). Considering the identical cathodes used in both cells, the decay of cell performance is mainly caused by degradation of the LMA, more specifically, dendrite formation and the side reactions between metallic lithium and electrolyte species.[140]

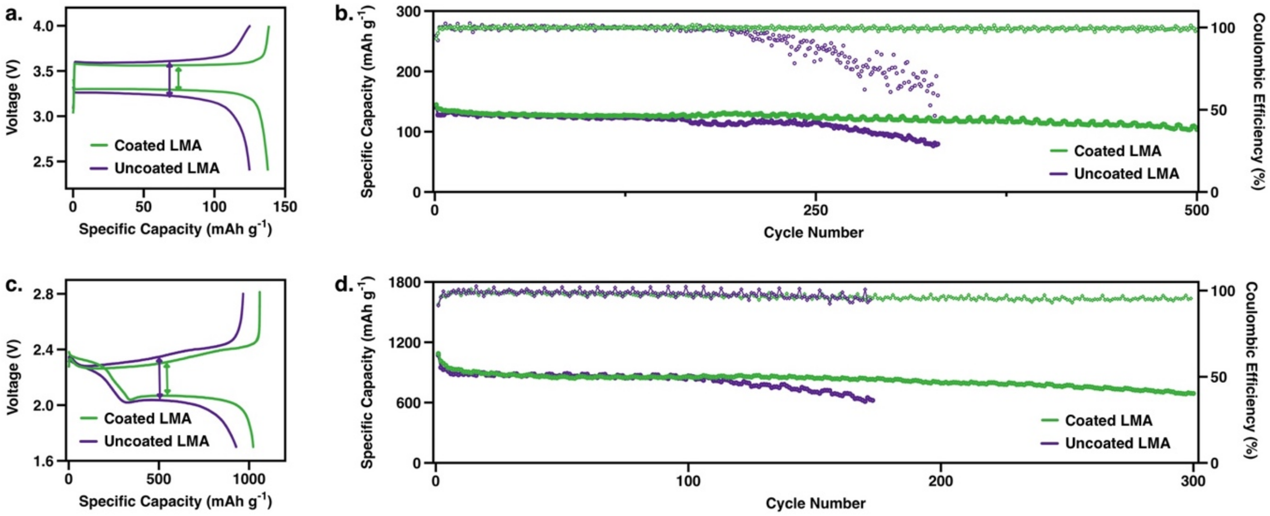

Figure 8.15 a. Voltage-capacity profile of Li-$LiFePO_4$ cells during the 3rd cycle at 0.5 C rate; **b.** Galvanostatic cycling performance of Li-$LiFePO_4$ cells at 0.5 C rate. **c.** Voltage-capacity profile of Li-S cells during the 3rd cycle at 0.3 C rate; **d.** Galvanostatic cycling performance of Li-S cells at 0.3 C rate.

In Li-S cells, the undesirable side-reactions between LMA and soluble lithium polysulfides (Li_2S_n, n= 4-8) complicate the situation. The formation of insulating Li_2S/Li_2S_2 layer on LMA and shuttling of polysulfides could builds up internal resistance and reduces coulombic efficiency, respectively. These issues could be mitigated by forming a hermetic coating on LMA. To adapt such coated LMA in lithium-sulfur system, Li-S cells were constructed with 1M LiTFSI and 1 wt % $LiNO_3$ in DOL/DME (*v*:*v* = 1:1) and tested at 0.3 C rate (1 C = 1675 mAh g^{-1}). Similar to the Li-$LiFePO_4$ cells, Li-S cell with coated LMA shows reduced cell polarization (233 mV *vs.* 300 mV) and increased initial capacity (Figure 8.15c). Regarding to electrochemical stability, the sulfur cathode with a coated LMA maintains a reversible capacity of 693 mAh g^{-1} after 300 cycles with an average coulombic efficiency of 96.6%. Whereas the sulfur cathode with an uncoated LMA experiences rapid capacity deterioration after 100 cycles, and encounters cell failure after 173 cycles due to dendrite-induced short-circuit (Figure 8.15d). The average cycling lifetime and capacity degradation rate of Li-S cells show small deviations, indicating excellent reproducibility and consistency of this deposition method (Figure 8.16).

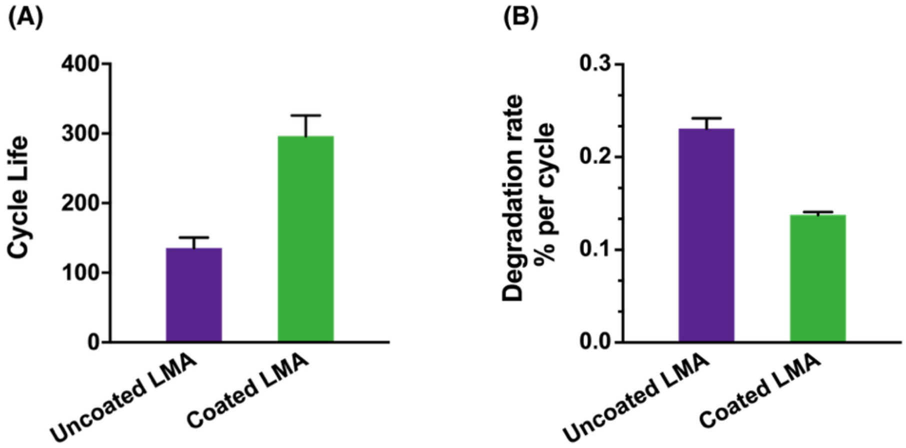

Figure 8.16 Comparison of (A) average cycling life and (B) degradation rate of capacity of Li-S batteries with uncoated and coated LMAs at 0.3 C rate. The number of cells in each group is 4.

8.5 Side-reactions with electrolyte components

To further understand the mechanism, the surface layers of the post-cycle LMA in Li-S cells were investigated using XPS. As shown in Figure 8.17 a and e, the carbon spectra of the coated and uncoated LMA present five binding states at 292.6, 289.7, 288.3, 286.3 and 284.5 eV, corresponding to $-CF_3$, -O-C=O, -C=O, -C-O and -C-C- groups, respectively.[141] Among these species, $-CF_3$ group can be assigned to LiTFSI, while the rests are mainly originated from the decomposition products of the organic solvents. Significantly less decomposition species is formed for the uncoated LMA. Meanwhile, both fluorine spectra exhibit two valence states at 688.4 and 684.4 eV, which can be attributed to $-CF_3$ in LiTFSI and LiF from decomposed LiTFSI, respectively (Figure 8.17 b and f).[141] Consistently, the relative amount of LiF is much higher for the uncoated LMA (50.2% *vs.* 12.8%). On the other hand, the nitrogen species on these two LMAs are not identical. For the uncoated LMA, five binding states at 403.7, 400.6, 399.2, 398.2 and

396.8 eV can be assigned to N-O, -N=C, -N-SO_2- (as in LiTFSI), LiN_3, and -NH_x groups, respectively[142-144] (Figure 8.17 c). For the coated LMA, no signal of -N=C presents but an additional peak at 407.4 eV can be assigned to -NO_x as in $LiNO_3$ (Figure 8.17d). All of the above results reveal fewer decomposition products from the electrolyte on the coated LMA, thanks to the hermetic coatings. More importantly, due to the high stability of the hybrid silicate coatings, the Li_xSiO_y component (at 101.6 eV, Figure 8.17 h) is well maintained after the repetitive lithium plating/stripping and long-term exposure to organic solvents and polysulfide anions.

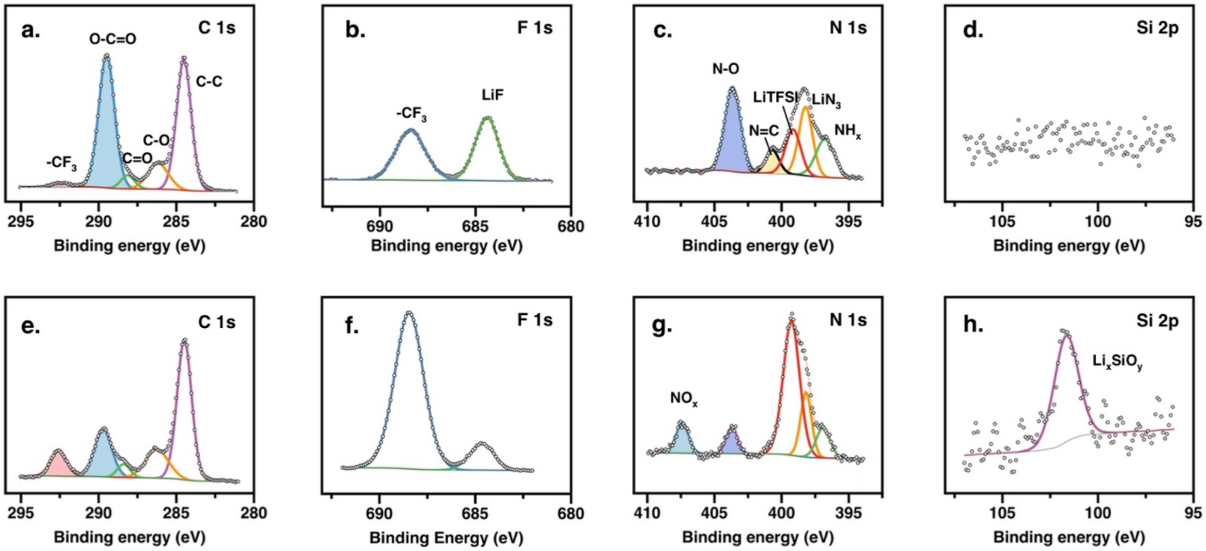

Figure 8.17. XPS analysis of LMAs after cycling regarding (**a**, **e**) carbon 1s, (**b**, **f**) fluorine 1s and (**c**, **g**) nitrogen 1s and (**d**, **h**) silicon 2p spectra of uncoated and coated LMAs, respectively. Both cells were cycled at 0.3 C rate for 150 cycles and interrupted at a fully charged state (2.8 V *vs.* Li^+/Li).

8.6 Conclusion

In this work, we have successfully demonstrated the fabrication of robust hybrid silicate coatings on lithium surface by a facile vapor deposition method. Catalyzed by Li_2O and LiOH on the surface of lithium foils, protective coatings can be *in situ* formed with vapors of 3-

mercaptopropyl trimethoxysilane (MPS) and tetraethoxysilane (TEOS). The resulting anodes demonstrated significantly enhanced electrochemical stability in symmetric lithium cells and rechargeable lithium batteries. Such enhancement is originated from the hybrid silicate structure with both organic and inorganic moieties. This simple yet effective approach opens a new route for the stabilization of metallic anodes and brings rechargeable lithium-metal batteries one step closer to practical application.

Reference

1. Bresser, D. *et al.* Perspectives of automotive battery R&D in China, Germany, Japan, and the USA. *J. Power Sources* **382,** 176-178 (2018).
2. Bard, A. J. & Faulkner, L. R. *Electrochemical methods: Fundamentals and applications*. (Wiley, 2000).
3. Winter, M. & Brodd, R. J. What are batteries, fuel cells, and supercapacitors? *Chem. Rev.* **104,** 4245-4269 (2004).
4. Manthiram, A. An outlook on lithium ion battery technology. *ACS Cent. Sci.* **3,** 1063-1069 (2017).
5. Schweidler, S. *et al.* Volume changes of graphite anodes revisited: A combined *operando* X-ray diffraction and *In Situ* pressure analysis study. *J. Phys. Chem. C* **122,** 8829-8835 (2018).
6. Kim, H., Seo, M., Park, M.-H. & Cho, J. A critical size of silicon nano-anodes for lithium rechargeable batteries. *Angew. Chem. Int. Ed. Engl.* **49,** 2146-2149 (2010).
7. Li, Y. *et al.* Growth of conformal graphene cages on micrometre-sized silicon particles as stable battery anodes. *Nat. Energy* **1,** 15029 (2016).
8. Magasinski, A. *et al.* High-performance lithium-ion anodes using a hierarchical bottom-up approach. *Nat. Mater.* **9,** 353-358 (2010).
9. Wu, H. *et al.* Stable Li-ion battery anodes by in-situ polymerization of conducting hydrogel to conformally coat silicon nanoparticles. *Nat Commun* **4,** 1943 (2013).
10. Wang, C. *et al.* Self-healing chemistry enables the stable operation of silicon microparticle anodes for high-energy lithium-ion batteries. *Nat. Chem.* **5,** 1042-1048 (2013).
11. Liu, Q. *et al.* Insight on lithium polysulfide intermediates in a Li/S battery by density functional theory. *RSC Adv.* **7,** 33373-33377 (2017).
12. Vijayakumar, M. *et al.* Molecular structure and stability of dissolved lithium polysulfide species. *Phys. Chem. Chem. Phys.* **16,** 10923-10932 (2014).
13. Xiao, J. *et al.* Following the transient reactions in lithium-sulfur batteries using an in situ nuclear magnetic resonance technique. *Nano Lett* **15,** 3309-3316 (2015).
14. Wang, Q. *et al.* Direct observation of sulfur radicals as reaction media in lithium sulfur batteries. *J. Electrochem. Soc.* **162,** A474-A478 (2015).
15. Wujcik, K. H. *et al.* Characterization of polysulfide radicals present in an ether-based electrolyte of a lithium-sulfur battery during initial discharge using in situ X-ray absorption spectroscopy experiments and first-principles calculations. *Adv. Energy Mater.* **5,** 1500285 (2015).
16. Ji, X., Lee, K. T. & Nazar, L. F. A highly ordered nanostructured carbon-sulphur cathode for lithium-sulphur batteries. *Nat. Mater.* **8,** 500-506 (2009).
17. Han, S.-C. *et al.* Effect of multiwalled carbon nanotubes on electrochemical properties of lithium/sulfur rechargeable batteries. *J. Electrochem. Soc.* **150,** A889 (2003).
18. Ji, L. *et al.* Porous carbon nanofiber-sulfur composite electrodes for lithium/sulfur cells. *Energy Environ. Sci.* **4,** 5053 (2011).
19. Wang, H. *et al.* Graphene-wrapped sulfur particles as a rechargeable lithium-sulfur battery cathode material with high capacity and cycling stability. *Nano Lett* **11,** 2644-2647 (2011).
20. Evers, S. & Nazar, L. F. Graphene-enveloped sulfur in a one pot reaction: a cathode with good coulombic efficiency and high practical sulfur content. *Chem. Commun.* **48,** 1233-1235 (2012).
21. Li, X. *et al.* Optimization of mesoporous carbon structures for lithium-sulfur battery

applications. *J. Mater. Chem.* **21,** 16603 (2011).

22. Jayaprakash, N., Shen, J., Moganty, S. S., Corona, A. & Archer, L. A. Porous hollow carbon@sulfur composites for high-power lithium-sulfur batteries. *Angew. Chem. Int. Ed. Engl.* **50,** 5904-5908 (2011).
23. Zhao, M.-Q. *et al.* Graphene/single-walled carbon nanotube hybrids: one-step catalytic growth and applications for high-rate Li-S batteries. *ACS Nano* **6,** 10759-10769 (2012).
24. Zhang, C., Wu, H. B., Yuan, C., Guo, Z. & Lou, X. W. Confining sulfur in double-shelled hollow carbon spheres for lithium-sulfur batteries. *Angew. Chem. Int. Ed. Engl.* **51,** 9592-9595 (2012).
25. Xu, T. *et al.* Mesoporous carbon-carbon nanotube-sulfur composite microspheres for high-areal-capacity lithium-sulfur battery cathodes. *ACS Appl. Mater. Interfaces* **5,** 11355-11362 (2013).
26. Hagen, M. *et al.* Lithium-sulfur cells: The gap between the state-of-the-art and the requirements for high energy battery cells. *Adv. Energy Mater.* **5,** 1401986 (2015).
27. Song, J. *et al.* Nitrogen-doped mesoporous carbon promoted chemical adsorption of sulfur and fabrication of high-areal-capacity sulfur cathode with exceptional cycling stability for lithium-sulfur batteries. *Adv. Funct. Mater.* **24,** 1243-1250 (2014).
28. Song, J. *et al.* Strong lithium polysulfide chemisorption on electroactive sites of nitrogen-doped carbon composites for high-performance lithium-sulfur battery cathodes. *Angew. Chem. Int. Ed. Engl.* **54,** 4325-4329 (2015).
29. Zhou, G., Zhao, Y. & Manthiram, A. Dual-confined flexible sulfur cathodes encapsulated in nitrogen-doped double-shelled hollow carbon spheres and wrapped with graphene for Li-S batteries. *Adv. Energy Mater.* **5,** 1402263 (2015).
30. Wu, H. *et al.* A high-efficiency N/P co-doped graphene/CNT@porous carbon hybrid matrix as a cathode host for high performance lithium-sulfur batteries. *J. Mater. Chem. A* **5,** 20458-20472 (2017).
31. Pang, Q. *et al.* A nitrogen and sulfur dual-doped carbon derived from polyrhodanine@cellulose for advanced lithium-sulfur batteries. *Adv. Mater. Weinheim* **27,** 6021-6028 (2015).
32. Peng, H.-J. *et al.* Strongly coupled interfaces between a heterogeneous carbon host and a sulfur-containing guest for highly stable lithium-sulfur batteries: Mechanistic insight into capacity degradation. *Adv. Mater. Interfaces* **1,** 1400227 (2014).
33. Peng, H.-J. *et al.* Enhanced electrochemical kinetics on conductive polar mediators for lithium-sulfur batteries. *Angew. Chem. Int. Ed. Engl.* **55,** 12990-12995 (2016).
34. Pang, Q., Kundu, D., Cuisinier, M. & Nazar, L. F. Surface-enhanced redox chemistry of polysulphides on a metallic and polar host for lithium-sulphur batteries. *Nat. Commun.* **5,** 4759 (2014).
35. Chang, C.-H., Chung, S.-H. & Manthiram, A. Effective stabilization of a high-loading sulfur cathode and a lithium-metal anode in Li-S batteries utilizing SWCNT-modulated separators. *Small* **12,** 174-179 (2016).
36. Zhuang, T.-Z. *et al.* Rational integration of polypropylene/graphene oxide/nafion as ternary-layered separator to retard the shuttle of polysulfides for lithium-sulfur batteries. *Small* **12,** 381-389 (2016).
37. Sun, Y., Liu, N. & Cui, Y. Promises and challenges of nanomaterials for lithium-based rechargeable batteries. *Nat. Energy* 16071 (2016).
38. Lin, D., Liu, Y. & Cui, Y. Reviving the lithium metal anode for high-energy batteries. *Nat.*

Nanotechnol. **12,** 194-206 (2017).

39. Xu, W. *et al.* Lithium metal anodes for rechargeable batteries. *Energy Environ. Sci.* **7,** 513-537 (2014).
40. Cheng, X.-B., Zhang, R., Zhao, C.-Z. & Zhang, Q. Toward safe lithium metal anode in rechargeable batteries: A review. *Chem. Rev.* **117,** 10403-10473 (2017).
41. Brissot, C., Rosso, M., Chazalviel, J. N. & Lascaud, S. Dendritic growth mechanisms in lithium/polymer cells. *J. Power Sources* **81-82,** 925-929 (1999).
42. Brissot, C., Rosso, M., Chazalviel, J. N., Baudry, P. & Lascaud, S. In situ study of dendritic growth inlithium/PEO-salt/lithium cells. *Electrochim. Acta* **43,** 1569-1574 (1998).
43. Rosso, M. *et al.* Dendrite short-circuit and fuse effect on Li/polymer/Li cells. *Electrochim. Acta* **51,** 5334-5340 (2006).
44. Bouchet, R., Lascaud, S. & Rosso, M. An EIS Study of the Anode Li/PEO-LiTFSI of a Li Polymer Battery. *J. Electrochem. Soc.* **150,** A1385 (2003).
45. Chazalviel, J. Electrochemical aspects of the generation of ramified metallic electrodeposits. *Phys Rev, A* **42,** 7355-7367 (1990).
46. Monroe, C. & Newman, J. The impact of elastic deformation on deposition kinetics at lithium/polymer interfaces. *J. Electrochem. Soc.* **152,** A396 (2005).
47. Aurbach, D. *et al.* On the Surface Chemical Aspects of Very High Energy Density, Rechargeable Li-Sulfur Batteries. *J. Electrochem. Soc.* **156,** A694 (2009).
48. Xiong, S., Xie, K., Diao, Y. & Hong, X. Characterization of the solid electrolyte interphase on lithium anode for preventing the shuttle mechanism in lithium-sulfur batteries. *J. Power Sources* **246,** 840-845 (2014).
49. Song, J. H. *et al.* Effect of fluoroethylene carbonate on electrochemical performances of lithium electrodes and lithium-sulfur batteries. *J. Electrochem. Soc.* **160,** A873-A881 (2013).
50. Heine, J. *et al.* Fluoroethylene carbonate as electrolyte additive in tetraethylene glycol dimethyl ether based electrolytes for application in lithium ion and lithium metal batteries. *J. Electrochem. Soc.* **162,** A1094-A1101 (2015).
51. Aurbach, D. A short review of failure mechanisms of lithium metal and lithiated graphite anodes in liquid electrolyte solutions. *Solid State Ionics* **148,** 405-416 (2002).
52. Peled, E. The electrochemical behavior of alkali and alkaline earth metals in nonaqueous battery systems—the solid electrolyte interphase model. *J. Electrochem. Soc.* **126,** 2047 (1979).
53. Ding, F. *et al.* Dendrite-free lithium deposition via self-healing electrostatic shield mechanism. *J. Am. Chem. Soc.* **135,** 4450-4456 (2013).
54. Dudney, N. J., West, W. C. & Nanda, J. *Handbook of solid state batteries*. (WORLD SCIENTIFIC, 2015).
55. Stone, G. M. *et al.* Resolution of the modulus versus adhesion dilemma in solid polymer electrolytes for rechargeable lithium metal batteries. *J. Electrochem. Soc.* **159,** A222-A227 (2012).
56. Zhang, L. *et al.* Effect of lithium borate addition on the physical and electrochemical properties of the lithium ion conductor $Li_{3.4}Si_{0.4}P_{0.6}O_4$. *Solid State Ionics* **231,** 109-115 (2013).
57. Zhang, T. *et al.* Stability of a water-stable lithium metal anode for a lithium-air battery with acetic acid-water solutions. *J. Electrochem. Soc.* **157,** A214 (2010).
58. Chung, K., Kim, W.-S. & Choi, Y.-K. Lithium phosphorous oxynitride as a passive layer for anodes in lithium secondary batteries. *Journal of Electroanalytical Chemistry* **566,** 263-267

(2004).
59. Kozen, A. C. *et al.* Next-generation lithium metal anode engineering via atomic layer deposition. *ACS Nano* **9,** 5884-5892 (2015).
60. Khurana, R., Schaefer, J. L., Archer, L. A. & Coates, G. W. Suppression of lithium dendrite growth using cross-linked polyethylene/poly(ethylene oxide) electrolytes: a new approach for practical lithium-metal polymer batteries. *J. Am. Chem. Soc.* **136,** 7395-7402 (2014).
61. Bouchet, R. *et al.* Single-ion BAB triblock copolymers as highly efficient electrolytes for lithium-metal batteries. *Nat. Mater.* **12,** 452-457 (2013).
62. Choi, S. M. *et al.* Cycling characteristics of lithium metal batteries assembled with a surface modified lithium electrode. *J. Power Sources* **244,** 363-368 (2013).
63. Kozen, A. C. *et al.* Stabilization of lithium metal anodes by hybrid artificial solid electrolyte interphase. *Chem. Mater.* **29,** 6298-6307 (2017).
64. Zheng, G. *et al.* Interconnected hollow carbon nanospheres for stable lithium metal anodes. *Nat. Nanotechnol.* **9,** 618-623 (2014).
65. Huang, S., Tang, L., Najafabadi, H. S., Chen, S. & Ren, Z. A highly flexible semi-tubular carbon film for stable lithium metal anodes in high-performance batteries. *Nano Energy* **38,** 504-509 (2017).
66. Liu, G., Niu, P., Yin, L. & Cheng, H.-M. α-Sulfur crystals as a visible-light-active photocatalyst. *J. Am. Chem. Soc.* **134,** 9070-9073 (2012).
67. Fan, F. Y. *et al.* Solvent effects on polysulfide redox kinetics and ionic conductivity in lithium-sulfur batteries. *J. Electrochem. Soc.* **163,** A3111-A3116 (2016).
68. Paolella, A. *et al.* Transient existence of crystalline lithium disulfide Li_2S_2 in a lithium-sulfur battery. *J. Power Sources* **325,** 641-645 (2016).
69. Yang, G., Shi, S., Yang, J. & Ma, Y. Insight into the role of Li_2 S_2 in Li-S batteries: a first-principles study. *J. Mater. Chem. A* **3,** 8865-8869 (2015).
70. Sun, J., Ruzsinszky, A. & Perdew, J. P. Strongly constrained and appropriately normed semilocal density functional. *Phys. Rev. Lett.* **115,** 036402 (2015).
71. Elazari, R., Salitra, G., Garsuch, A., Panchenko, A. & Aurbach, D. Sulfur-impregnated activated carbon fiber cloth as a binder-free cathode for rechargeable Li-S batteries. *Adv. Mater.* **23,** 5641-5644 (2011).
72. Zhou, G., Paek, E., Hwang, G. S. & Manthiram, A. Long-life Li/polysulphide batteries with high sulphur loading enabled by lightweight three-dimensional nitrogen/sulphur-codoped graphene sponge. *Nat. Commun.* **6,** 7760 (2015).
73. Ji, X., Evers, S., Black, R. & Nazar, L. F. Stabilizing lithium-sulphur cathodes using polysulphide reservoirs. *Nat. Commun.* **2,** 325 (2011).
74. Wei Seh, Z. *et al.* Sulphur-TiO_2 yolk-shell nanoarchitecture with internal void space for long-cycle lithium-sulphur batteries. *Nat. Commun.* **4,** 1331 (2013).
75. Chung, W. J. *et al.* The use of elemental sulfur as an alternative feedstock for polymeric materials. *Nat. Chem.* **5,** 518-524 (2013).
76. Yan, N. *et al.* Fabrication of a nano-Li-channel interlayer for high performance Li-S battery application. *RSC Adv.* **5,** 26273-26280 (2015).
77. Huang, J.-Q. *et al.* Ionic shield for polysulfides towards highly-stable lithium-sulfur batteries. *Energy Environ. Sci.* **7,** 347-353 (2014).
78. Jin, Z., Xie, K. & Hong, X. Electrochemical performance of lithium/sulfur batteries using perfluorinated ionomer electrolyte with lithium sulfonyl dicyanomethide functional groups as functional separator. *RSC Adv.* **3,** 8889 (2013).

79. Li, W. *et al.* V_2O_5 polysulfide anion barrier for long-lived Li-S batteries. *Chem. Mater.* **26,** 3403-3410 (2014).
80. Su, Y.-S. & Manthiram, A. A new approach to improve cycle performance of rechargeable lithium-sulfur batteries by inserting a free-standing MWCNT interlayer. *Chem. Commun. (Camb)* **48,** 8817-8819 (2012).
81. Chung, S.-H. & Manthiram, A. High-performance Li-S batteries with an ultra-lightweight MWCNT-coated separator. *J. Phys. Chem. Lett.* **5,** 1978-1983 (2014).
82. Wang, G., Lai, Y., Zhang, Z., Li, J. & Zhang, Z. Enhanced rate capability and cycle stability of lithium-sulfur batteries with a bifunctional MCNT@PEG-modified separator. *J. Mater. Chem. A* **3,** 7139-7144 (2015).
83. Kim, H. M., Hwang, J.-Y., Manthiram, A. & Sun, Y.-K. High-performance lithium-sulfur batteries with a self-assembled multiwall carbon nanotube interlayer and a robust electrode-electrolyte interface. *ACS Appl. Mater. Interfaces* **8,** 983-987 (2016).
84. Vizintin, A. *et al.* Fluorinated reduced graphene oxide as an interlayer in Li-S batteries. *Chem. Mater.* **27,** 7070-7081 (2015).
85. Huang, J.-Q. *et al.* Permselective graphene oxide membrane for highly stable and anti-self-discharge lithium-sulfur batteries. *ACS Nano* **9,** 3002-3011 (2015).
86. Zu, C., Su, Y.-S., Fu, Y. & Manthiram, A. Improved lithium-sulfur cells with a treated carbon paper interlayer. *Phys. Chem. Chem. Phys.* **15,** 2291-2297 (2013).
87. Yao, H. *et al.* Improved lithium-sulfur batteries with a conductive coating on the separator to prevent the accumulation of inactive S-related species at the cathode-separator interface. *Energy Environ. Sci.* **7,** 3381-3390 (2014).
88. Chung, S.-H. & Manthiram, A. Bifunctional separator with a light-weight carbon-coating for dynamically and statically stable lithium-sulfur batteries. *Adv. Funct. Mater.* **24,** 5299-5306 (2014).
89. Singhal, R., Chung, S.-H., Manthiram, A. & Kalra, V. A free-standing carbon nanofiber interlayer for high-performance lithium-sulfur batteries. *J. Mater. Chem. A* **3,** 4530-4538 (2015).
90. Balach, J. *et al.* Functional mesoporous carbon-coated separator for long-life, high-energy lithium-sulfur batteries. *Adv. Funct. Mater.* **25,** 5285-5291 (2015).
91. Chung, S.-H., Han, P., Singhal, R., Kalra, V. & Manthiram, A. Electrochemically stable rechargeable lithium-sulfur batteries with a microporous carbon nanofiber filter for polysulfide. *Adv. Energy Mater.* **5,** 1500738 (2015).
92. Chung, S.-H. & Manthiram, A. A polyethylene glycol-supported microporous carbon coating as a polysulfide trap for utilizing pure sulfur cathodes in lithium-sulfur batteries. *Adv. Mater.* **26,** 7352-7357 (2014).
93. Su, Y.-S. & Manthiram, A. Lithium-sulphur batteries with a microporous carbon paper as a bifunctional interlayer. *Nat. Commun.* **3,** 1166 (2012).
94. Song, R. *et al.* A trilayer separator with dual function for high performance lithium-sulfur batteries. *J. Power Sources* **301,** 179-186 (2016).
95. Xiao, Z. *et al.* A Lightweight TiO_2/graphene interlayer, applied as a highly effective polysulfide absorbent for fast, long-life lithium-sulfur batteries. *Adv. Mater.* **27,** 2891-2898 (2015).
96. Kim, M. S. *et al.* Fabricating multifunctional nanoparticle membranes by a fast layer-by-layer Langmuir-Blodgett process: application in lithium-sulfur batteries. *J. Mater. Chem. A* **4,** 14709-14719 (2016).

97. Chen, Z. *et al.* Design and synthesis of hierarchical nanowire composites for electrochemical energy storage. *Adv. Funct. Mater.* **19,** 3420-3426 (2009).
98. Ma, Y. *et al.* Lithium sulfur primary battery with super high energy density: Based on the cauliflower-like structured C/S cathode. *Sci. Rep.* **5,** 14949 (2015).
99. Li, G. *et al.* Synthesis of V_2O_5 hierarchical structures for long cycle-life lithium-ion storage. *J. Mater. Chem. A* **3,** 1103-1109 (2015).
100. Lee, J. W. *et al.* Extremely stable cycling of ultra-thin V_2O_5 nanowire-graphene electrodes for lithium rechargeable battery cathodes. *Energy Environ. Sci.* **5,** 9889 (2012).
101. Petkov, V. *et al.* Structure of $V_2O_5 \cdot n\ H_2O$ Xerogel solved by the atomic pair distribution function technique. *J. Am. Chem. Soc.* **124,** 10157-10162 (2002).
102. Xiong, C., Aliev, A. E., Gnade, B. & Balkus, K. J. Fabrication of silver vanadium oxide and V2O5 nanowires for electrochromics. *ACS Nano* **2,** 293-301 (2008).
103. Zhang, S. S. Liquid electrolyte lithium/sulfur battery: Fundamental chemistry, problems, and solutions. *J. Power Sources* **231,** 153-162 (2013).
104. Hart, C. J. *et al.* Rational design of sulphur host materials for Li-S batteries: correlating lithium polysulphide adsorptivity and self-discharge capacity loss. *Chem. Commun.* **51,** 2308-2311 (2015).
105. Mendialdua, J., Casanova, R. & Barbaux, Y. XPS studies of V_2O_5, V_6O_{13}, VO_2 and V_2O_3. *J. Electron Spectros. Relat. Phenomena* **71,** 249-261 (1995).
106. Liang, X. *et al.* A highly efficient polysulfide mediator for lithium-sulfur batteries. *Nat. Commun.* **6,** 5682 (2015).
107. Tao, X. *et al.* Strong sulfur binding with conducting Magnéli-phase $Ti_nO_{2(n-1)}$ nanomaterials for improving lithium-sulfur batteries. *Nano Lett.* **14,** 5288-5294 (2014).
108. Hiemenz, P. C. & Rajagopalan, R. *Principles of Colloid and Surface Chemistry*. (1997).
109. Dean, J. A. *Lange's handbook of chemistry*. (1985).
110. Matar, S. F., Campet, G. & Subramanian, M. A. Electronic properties of oxides: Chemical and theoretical approaches. *Progress in Solid State Chemistry* **39,** 70-95 (2011).
111. Masel, R. I. *Principles of Adsorption and Reaction on Solid Surfaces*. (John Wiley & Sons, 1996).
112. Greiner, M. T. *et al.* Universal energy-level alignment of molecules on metal oxides. *Nat. Mater.* **11,** 76-81 (2012).
113. Xu, Y. & Schoonen, M. A. A. The absolute energy positions of conduction and valence bands of selected semiconducting minerals. *Am. Mineral.* **85,** 543-556 (2000).
114. Greiner, M. T., Chai, L., Helander, M. G., Tang, W.-M. & Lu, Z.-H. Transition metal oxide work functions: The influence of cation oxidation state and oxygen vacancies. *Adv. Funct. Mater.* **22,** 4557-4568 (2012).
115. Augustyn, V. *et al.* High-rate electrochemical energy storage through Li^+ intercalation pseudocapacitance. *Nat. Mater.* **12,** 518-522 (2013).
116. Sun, H. *et al.* Three-dimensional holey-graphene/niobia composite architectures for ultrahigh-rate energy storage. *Science (80).* **356,** 599-604 (2017).
117. Tan, H., Wang, S. & Lei, X. New insights for the cyclic performance of Li/MnO_2 batteries using a simple electrochemical process. *J. Electrochem. Soc.* **162,** A448-A452 (2015).
118. Wang, D. *et al.* β-MnO_2 as a cathode material for lithium ion batteries from first principles calculations. *Phys. Chem. Chem. Phys.* **15,** 9075-9083 (2013).
119. Chen, D. *et al.* Unraveling the naure of anomalously fast energy storage in T-Nb_2O_5. *J. Am. Chem. Soc.* **139,** 7071-7081 (2017).

120. Pinto, M. B., Soares, A. L., Mella Orellana, A., Duarte, H. A. & De Abreu, H. A. Structural, electronic, and thermodynamic properties of the T and B Phases of niobia: First-principle calculations. *J. Phys. Chem. A* **121,** 2399-2409 (2017).

121. Kitchaev, D. A., Dacek, S. T., Sun, W. & Ceder, G. Thermodynamics of phase selection in MnO_2 framework structures through alkali intercalation and hydration. *J. Am. Chem. Soc.* **139,** 2672-2681 (2017).

122. Gaillot, A.-C. *et al.* Structure of synthetic K-rich birnessite obtained by high-temperature decomposition of $KMnO_4$. I. Two-layer polytype from 800 °C experiment. *Chem. Mater.* **15,** 4666-4678 (2003).

123. Zhang, Y. *et al.* Efficient first-principles prediction of solid stability: Towards chemical accuracy. *Comput. Mater.* **4,** 9 (2018).

124. Kitchaev, D. A. *et al.* Energetics ofpolymorphs in density functional theory. *Phys. Rev. B* **93,** 045132 (2016).

125. Park, H., Koh, H. S. & Siegel, D. J. First-principles study of redox end members in lithium-sulfur batteries. *J. Phys. Chem. C* **119,** 4675-4683 (2015).

126. Pham, C. V., Krueger, M., Eck, M., Weber, S. & Erdem, E. Comparative electron paramagnetic resonance investigation of reduced graphene oxide and carbon nanotubes with different chemical functionalities for quantum dot attachment. *Appl. Phys. Lett.* **104,** 132102 (2014).

127. Stathi, P., Gournis, D., Deligiannakis, Y. & Rudolf, P. Stabilization of phenolic radicals on graphene oxide: an XPS and EPR study. *Langmuir* **31,** 10508-10516 (2015).

128. Jida, S. & Miki, T. Electron paramagnetic resonance of Nb-doped $BaTiO_3$ ceramics with positive temperature coefficient of resistivity. *J. Appl. Phys.* **80,** 5234-5239 (1996).

129. Zimmermann, P. H. Temperature dependence of the EPR spectra of niobium-doped TiO_2. *Phys. Rev. B* **8,** 3917-3927 (1973).

130. Zhou, P. *et al.* Effect of concurrent joule heat and charge trapping on RESET for NbAlO fabricated by atomic layer deposition. *Nanoscale Res. Lett.* **8,** 91 (2013).

131. Rahman, M. M. *et al.* A vein-like nanoporous network of Nb_2O_5 with a higher lithium intercalation discharge cut-off voltage. *J. Mater. Chem. A* **1,** 11019 (2013).

132. Diao, Y., Xie, K., Xiong, S. & Hong, X. Insights into Li-S battery cathode capacity fading mechanisms: Irreversible oxidation of active mass during cycling. *J. Electrochem. Soc.* **159,** A1816-A1821 (2012).

133. Liu, F. *et al.* Regenerative polysulfide-scavenging layers enabling lithium-sulfur batteries with high energy density and prolonged cycling life. *ACS Nano* **11,** 2697-2705 (2017).

134. Xue, W. *et al.* Gravimetric and volumetric energy densities of lithium-sulfur batteries. *Curr. Opin. Electrochem.* **6,** 92-99 (2017).

135. Karakassides, M. A. An infrared reflectance study of Si-O vibrations in thermally treated alkali-saturated montmorillonites. *Clay Miner* **34,** 429-438 (1999).

136. Philippe, B. *et al.* Role of the $LiPF_6$ Salt for the long-term stability of silicon electrodes in Li-ion batteries - A photoelectron spectroscopy study. *Chem. Mater.* **25,** 394-404 (2013).

137. Radvanyi, E., De Vito, E., Porcher, W. & Jouanneau Si Larbi, S. An XPS/AES comparative study of the surface behaviour of nano-silicon anodes for Li-ion batteries. *J. Anal. At. Spectrom.* **29,** 1120 (2014).

138. Seh, Z. W. *et al.* Facile synthesis of Li_2S-polypyrrole composite structures for high-performance Li_2S cathodes. *Energy Environ. Sci.* **7,** 672 (2014).

139. Barchasz, C., Leprêtre, J.-C., Patoux, S. & Alloin, F. Electrochemical properties of ether-

based electrolytes for lithium/sulfur rechargeable batteries. *Electrochim. Acta* **89,** 737-743 (2013).

140. Lu, D. *et al.* Failure mechanism for fast-charged lithium metal batteries with liquid electrolytes. *Adv. Energy Mater.* **5,** 1400993 (2015).
141. Xu, C. *et al.* Interface layer formation in solid polymer electrolyte lithium batteries: an XPS study. *J. Mater. Chem. A* **2,** 7256 (2014).
142. Lee, H. *et al.* Chemical aspect of oxygen dissolved in a dimethyl sulfoxide-based electrolyte on lithium metal. *Electrochim. Acta* **123,** 419-425 (2014).
143. Wang, L., Liu, J., Yuan, S., Wang, Y. & Xia, Y. To mitigate self-discharge of lithium-sulfur batteries by optimizing ionic liquid electrolytes. *Energy Environ. Sci.* **9,** 224-231 (2016).
144. Xiong, S., Xie, K., Diao, Y. & Hong, X. Properties of surface film on lithium anode with $LiNO_3$ as lithium salt in electrolyte solution for lithium-sulfur batteries. *Electrochim. Acta* **83,** 78-86 (2012).